



Theses and Dissertations

2024-07-30

3D Printed Mounts for Liquid Microdroplet Resonators

Parker A. Awerkamp
Brigham Young University

Follow this and additional works at: <https://scholarsarchive.byu.edu/etd>



Part of the [Engineering Commons](#)

BYU ScholarsArchive Citation

Awerkamp, Parker A., "3D Printed Mounts for Liquid Microdroplet Resonators" (2024). *Theses and Dissertations*. 10465.

<https://scholarsarchive.byu.edu/etd/10465>

This Dissertation is brought to you for free and open access by BYU ScholarsArchive. It has been accepted for inclusion in Theses and Dissertations by an authorized administrator of BYU ScholarsArchive. For more information, please contact ellen_amatangelo@byu.edu.

3D Printed Mounts for Liquid Microdroplet Resonators

Parker A. Averkamp

A dissertation submitted to the faculty of
Brigham Young University
in partial fulfillment of the requirements for the degree of
Doctor of Philosophy

Ryan M. Camacho, Chair
Aaron R. Hawkins
Stephen Marshall Schultz
Daniel Elijah Smalley
Gregory P. Nordin

Department of Electrical and Computer Engineering
Brigham Young University

Copyright © 2024 Parker A. Averkamp

All Rights Reserved

3D Printed Mounts for Liquid Microdroplet Resonators

Parker A. Averkamp
Department of Electrical and Computer Engineering
Doctor of Philosophy

BYU Engineering

Abstract

Liquid microdroplet resonators provide an excellent tool for optical studies due to their innate smoothness and high quality factors, but they can be difficult to control. By using 3D printed mounts to support the droplets, we can obtain precise control over the droplet geometries and positions. We here present our work with oil, water, and ice microdroplets, as well as tools required to enable their study.

We first present methods for creating 3D printed mounts for oil microdroplet resonators. The mounts enable precise positioning of the droplets relative to a tapered optical fiber. The oil microdroplet resonators exhibited quality factors of over 4×10^5 .

Water microdroplet resonators are more difficult to create due to the evaporation of water. By supporting the droplet on a 3D printed structure that supplies water to the droplet, we can maintain a water microdroplet resonator in an ambient environment while also controlling its shape and size. The resulting resonators have high quality factors, with values measured as high as 6×10^8 .

Ice microdroplets may be useful as optical resonators; however, typically ice appears cloudy due to trapped air bubbles. We present a method for freezing clear ice microdroplets in both humid and dry environments, enabling the formation of a clear ice droplet without the risk of additional crystal growth. To facilitate the freezing of droplets in a low-humidity environment, we have developed an environmental control chamber capable of maintaining an arbitrary humidity level and controlling the temperature of a small sample. We here present instructions for its manufacture as well as validation of its function.

Finally, we present an automated fabrication system for the creation of tapered and dimpled optical fibers. Tapered fibers have been essential in our work as tools for optical coupling to microdroplet resonators, and dimpled fibers allow for coupling to on-chip structures. The system we present allows for their fabrication with no user input and is able to produce fibers with efficiencies over 90% at a high yield.

Keywords: optics, microdroplet, 3d printing, optical resonator, tapered fiber, dimpled fiber

Acknowledgments

I acknowledge partial funding by the National Institutes of Health under grant R15GM123405 and partial funding by the National Science Foundation under grant 1941583.

I would like to thank the many research colleagues without whose contributions this work would not have been possible. Davin Fish, who worked with me when nothing worked yet. We broke hundreds of fibers together and failed 33 times to make our first 3D printed mount. We dreamed up the water droplet mount together that he later refined the 3D printing parameters for. Daniel Yirenya-Tawiah and Rebecca Anderson, who made plenty of fibers and tested many designs from me and Davin. David Hill, who kept my projects alive when I was not in the lab and who found the method for controlling the water flow rate that made water resonators possible. He is an equal contributor to the humidity control box. Dean Van Woerkom, who tirelessly did whatever David and I asked of him when building the humidity box. Madi King, who kept up with our main projects even while she explored chemical smoothing of our devices. Brandt Bashaw, who developed PCBs, wrote code, and just made things work. Kimi Wright, the ice queen, who froze droplet after droplet and kept the ice project alive with her constant improvements. Ben Goodey and Ian Timothy, who helped me in my final push. They are finishing the projects I started and are starting the projects I couldn't.

I thank my fellow graduate students, Sequioa Ploeg, Christian Carver, Ben Szamosfalvi, and Ben Fisher, who helped me in many ways by discussing research, studying with me in class, and introducing me to several new restaurants.

I would also like to thank my advisor, Ryan Camacho, for his excellent guidance and motivation throughout my PhD. He taught me how to turn ideas into viable research projects and make those projects a success.

I would like to acknowledge and thank my wife, Ashlin, who kept me supplied with a large number of snacks, reminded me of many important events, and was always willing to listen when I needed to talk. She and our daughters have provided loving support, which has sustained me through my research. Their contribution is hard to see and hard to describe but was the most important of all.

Table of Contents

List of Figures vii

List of Tables ix

1	Introduction	1
1.1	Motivation	1
1.2	Background	4
2	3D Printed Mounts for Microdroplet Resonators	12
2.1	Introduction	12
2.2	Methods	13
2.3	Results	17
2.4	Conclusion	19
3	Self-Sustaining Water Microdroplet Resonators Using 3D Printed Microfluidics	21
3.1	Introduction	21
3.2	Materials and Methods	23
3.3	Results	29
3.4	Discussion	29
3.5	Conclusions	32
4	Freezing of Clear Ice Microdroplets	33
4.1	Introduction	33
4.2	Methods	33
4.3	Conclusion	39
4.4	Additional Work	40
5	Environmental Control Box	43
5.1	Hardware in Context	43
5.2	Hardware Description	44
5.3	Design Files Summary	46
5.4	Bill of Materials Summary	47
5.5	Build Instructions	49
5.6	Operation Instructions	65
5.7	Validation and Characterization	71
6	Automated Fabrication of Tapered and Dimpled Optical Fibers	76

6.1	Introduction	76
6.2	System Overview	77
6.3	Fiber Fabrication Procedure	79
6.4	Results	88
6.5	Conclusion	89
7	Conclusion	90
7.1	List of Publications	91
	References	92

List of Figures

- 1.1 Wetting principles of droplets. 6
- 1.2 Whispering gallery mode. 8
- 1.3 Optical mode of a tapered optical fiber. 10

- 2.1 Image of thin-film water recirculation device, including simulated optical modes. 14
- 2.2 Wetting principles of the oil microdroplet resonator device. 15
- 2.3 3D printed oil microdroplet device with its optical mode and optical path. 16
- 2.4 Image of a water/glycerol microdroplet and plot of its optical resonance. 17
- 2.5 Optical resonance of a paraffin oil microdroplet. 17
- 2.6 Coupling distance and efficiency of a paraffin oil microdroplet resonator. 18

- 3.1 Corner pinning on a 3D printed mount. 24
- 3.2 Microfluidic system of the devices. 25
- 3.3 A water droplet and its optical mode. 27
- 3.4 Resonant features of water microdroplets. 30

- 4.1 Setup for freezing the microdroplets. 34
- 4.2 Steps of the freezing process. 36
- 4.3 Optically clear ice droplet. 36
- 4.4 Calculation of the sublimation rate. 38
- 4.5 Effect of humidity on droplet stability. 39
- 4.6 Seeding from an ice crystal. 40
- 4.7 Steps of the channel seeding method. 41

- 5.1 Constructed box clamped onto optical breadboard. 45
- 5.2 Exploded view of OSCBox. 50
- 5.3 Untapped and tapped 1/4-20 holes in the acrylic. 51
- 5.4 Untapped and tapped 6/32 holes in the acrylic. 51
- 5.5 Main acrylic pieces after being laser cut and tapped. 51
- 5.6 Colored image of the acrylic pieces. 52
- 5.7 Colored image of the aluminum stock pieces. 53
- 5.8 Three different box corners. 53
- 5.9 Preliminary construction of the box. 54
- 5.10 Close-up picture of an assembled corner. 54

- 5.11 Acrylic pieces after epoxying the screws. 55
- 5.12 Instructions for applying caulk and epoxy to edges. 56
- 5.13 The window seal used for wire doors. 57
- 5.14 The valve assembly for the box. 58
- 5.15 Female-to-female wire doors examples. 58
- 5.16 Foam-sealed wire doors. 59
- 5.17 Acrylic pieces used to construct the glove door assembly. 60
- 5.18 Process for assembling the glove door. 61
- 5.19 Silica gel used inside the desiccator. 62
- 5.20 CAD rendering and actual assembly of fan-assisted chemical desiccator. 63
- 5.21 CAD rendering and actual assembly of the TEC. 64
- 5.22 Pyrolab overview. 65
- 5.23 Graphical User Interface for OSCBox. 66
- 5.24 Temperature box of the GUI. 66
- 5.25 Humidity box of the GUI. 67
- 5.26 Advanced settings button on the GUI. 67
- 5.27 PID control advanced options for the TEC. 68
- 5.28 Humidity control advanced options. 69
- 5.29 LED and LCD control boxes of the GUI. 69
- 5.30 Plot control buttons of the GUI. 70
- 5.31 Plot taskbar for manipulating plot views while the collection is paused. 70
- 5.32 Magnifying glass feature of the plot. 71
- 5.33 30-Minute humidity trials. 72
- 5.34 Long term humidity test. 72
- 5.35 Precise humidity control over 80 minutes. 73
- 5.36 5-Minute temperature control test. 73
- 5.37 30-Minute temperature control test. 74
- 5.38 Humidity effects on ice droplets. 74

- 6.1 Fiber tapering and dimpling system. 77
- 6.2 Graphical representation of Pyrolab. 78
- 6.3 The GUI used to control the dimpling system. 79
- 6.4 Steps for the fabrication of a tapered and dimpled optical fiber. 80
- 6.5 Optical throughput of a fiber being tapered. 81
- 6.6 Taper profile mapping using computer vision. 84
- 6.7 Motor movements during dimpling. 85
- 6.8 Custom fiber holder. 88

List of Tables

- 3.1 Experimental and calculated reservoir heights and the differences between them for given resonator sizes. 29
- 5.1 Specifications table. 43
- 5.2 Design files summary. 46
- 5.2 Design files summary. 47
- 5.3 Bill of materials. 48
- 5.3 Bill of materials. 49
- 5.4 Aluminum stock list. 52
- 6.1 Efficiency results of four dimpled fibers. 89

Introduction

1.1 Motivation

Microdroplets have long been used as optical resonators, first observed by Ashkin and Dziedzic in 1977 [1], who found that optically levitated microdroplets exhibited resonant behaviors. Microdroplets make ideal optical resonators because the surface tension of microdroplets creates a perfectly spherical shape with no surface roughness. The spherical shape of microdroplets supports optical whispering gallery modes, named after the studies by Lord Rayleigh of the acoustics of the whispering gallery in St. Paul's Cathedral. In liquids, these modes can produce strong resonances, since the smoothness of the liquid drastically reduces the surface scattering loss of the resonators. Many liquids have been used for microdroplet resonators, including oils, water, glycerol, organic liquids, and combinations of these [2]. The variety of liquids and other materials introduced into them makes their applications diverse.

The impressive resonant nature of microdroplets makes them useful as laser cavities, and in 1986 Qian et al. demonstrated the first droplet lasers [3]. Since then, many demonstrations of microdroplet lasers have been reported. Several different types of lasers have been shown, such as dye lasers [4–7], Raman lasers [8, 9], and biolasers [10, 11]. Microdroplet resonators have further been utilized to explore nonlinear optical interactions [12, 13], as well as optomechanical effects [12, 14] and material analysis and sensing [15–17]. Microdroplet resonators also present unique opportunities as a subject of study for tuning resonances [6, 18, 19] and producing resonators with high quality factors (Q) [20, 21].

However, liquid resonators are more difficult to work with than solid resonators, requiring careful consideration of how to create the droplet and position and support the droplet for optical interrogation. The droplets can be formed on support systems a number of ways, but the most common is to atomize the liquid over a surface or drop an individual droplet onto a support using a pipette or similar tool. Though these methods effectively create droplets of a sufficiently small size (<1 mm), precise control over the size of the droplet is not reported. In this work, we will describe novel methods for creating microdroplets that allow for control over the droplet size. Once formed, the droplets must be supported. Though water naturally forms smooth spherical droplets in a free environment, typically a droplet must be attached to

a surface to create a usable optical device. However, surface adhesion can degrade the shape of the droplet for use as a microresonator. This difficulty can be overcome by manipulating the droplets using optical tweezers [22–24], but this method adds significant complexity to the system. Simpler methods involve supporting microdroplets by placing them on a hydrophobic surface [6–8, 11, 18, 19, 21, 25, 26], suspending droplets from a glass stem [14, 20, 27–29], or suspending a droplet in another liquid [4, 12, 22, 23, 30]. These methods all maintain the droplet in a sufficiently spherical shape to establish optical resonance.

We present a different method for forming and supporting microdroplet resonators that relies on specially designed 3D printed mounts. 3D printing has been used in many fields as a method for rapidly developing custom, inexpensive devices. In recent years, the precision of 3D printing has increased dramatically [31, 32], making it an attractive alternative to other fabrication methods. The flexibility of the design and rapid fabricate-test-redesign cycle allows us to engineer mounts that provide both increased coupling stability and tailored features such as resonator shape, size, and type of liquid.

Special considerations must be taken when creating microdroplet resonators from water. Water microdroplet resonators can be challenging to study because of the rapid evaporation of water, which causes the droplet to change size. This effect is especially pronounced at the small scales used for optical resonators. Typical methods to overcome evaporation involve either adding a stabilizer to the water, controlling the droplet environment, or both [26]. Stabilizing agents can be added to water so that the evaporation rate is decreased. This results in the droplet reaching equilibrium at humidities less than 100%. The most common stabilizers are glycerol [7, 11, 18, 21] and salt [19, 24]. Glycerol is hygroscopic, allowing it to absorb water from the air to establish equilibrium. Salt lowers the vapor pressure of water, with similar results. Alternatively (or additionally), the droplet environment can be controlled by either keeping the droplet in a humidity-controlled chamber [6, 8, 26] or submerging the droplet in another liquid [30].

We present a solution for droplet formation, support, size control, and stabilization against evaporation using a custom 3D printed platform. Our design incorporates a microfluidic system that allows us to precisely control the size of the droplet upon formation, which has been used for non-evaporating oil droplets [5] but to our knowledge has not otherwise been demonstrated for water microdroplets. Our microfluidic system further serves to provide a constant flow of water to the microdroplet from an external reservoir, completely mitigating the effects of evaporation on the droplet without requiring the addition of a stabilizer to the droplet or a specialized environment. Other methods have been shown to replenish the droplet against evaporation [20], though these did not seek to control droplet size. The microfluidic system we present feeds into a specially designed 3D printed mount (see figure 3.2) that supports the droplet in a spherical shape and allows for precise droplet positioning. Using this device, we demonstrate water microdroplet resonators that can be

tailored to an arbitrary size and are stable against evaporation without requiring additives to the water or a controlled environment.

The promising results obtained in our study of water droplets led us to pursue the creation of ice microdroplets. Ice microresonators could exploit the ease of adding analytes to liquids while providing the stability of coupling of a solid resonator. However, ice often appears cloudy due to trapped gas bubbles and impurities. Ideally, an ice microdroplet would be transparent to minimize optical loss. This is possible by freezing the droplet under carefully controlled conditions. Researchers have investigated the properties of freezing microdroplets, such as the process of freezing microdroplets [33] and the effect of humidity on the freezing of droplets [34]. Further research not restricted to microdroplets investigated the optical properties of ice [35] and nonlinear optical properties, in particular at the surface of ice [36, 37]. Nonlinear optics have also been used to investigate the freezing process [38].

However, the majority of previous research is focused on using optical techniques to analyze ice, rather than using ice as an optical tool. A recent study was able to create a microdroplet resonator from ice [39] using a rapid freezing approach. We believe that a slow freezing process will create an ice microdroplet that is perfectly optically clear and therefore more suited as an optical resonator.

We present methods for freezing optically clear microdroplets by slowly freezing droplets in a single direction. This method results in frozen droplets free of trapped air bubbles.

Droplets frozen at standard humidity levels will begin to grow ice crystals on their surface, which is undesirable for an optical resonator. To overcome this, the droplet can be placed in a low-humidity environment. However, this in turn makes the droplet more difficult to freeze. We present a method for overcoming this difficulty, allowing for the freezing of clear ice droplets even at a low humidity.

To enable the formation of ice droplets at low humidities, as well as other experiments where environmental control is needed, we developed an environmental control box. This allows us to control the ambient humidity of the setup and the temperature at the device. The box demonstrates powerful control at a low cost, while allowing the operator to access components inside the box. In this work we present instructions for manufacturing this environmental control box, including both hardware and software descriptions. We provide instructions for its operation and validation of its performance.

Optical interrogation of microdroplets is typically achieved by using a tapered optical fiber, though some experiments use free-space lasers. In our work, we use tapered optical fibers that are fabricated in-house. We fabricate our tapered fibers using a heat-and-pull method similar to those used in [27, 40–42]. When tapering a fiber, the core of the fiber becomes too small to support the optical mode. When this happens, the light begins to travel in the cladding of the fiber, which continues to guide the light as a glass/air waveguide. When this occurs, the fiber diameter is sufficiently large to support multiple optical modes, and

these modes interfere with each other. The interference of these modes in combination with the changing length of the fiber as it continues to be tapered results in a beating pattern in the throughput of the fiber, which is seen as oscillations in the power output. As the fiber is tapered to smaller diameters, the higher order optical modes will no longer be supported, and those modes will no longer produce beating in the fiber throughput. To determine the pull length, the optical throughput of the taper is monitored, and the pull is stopped when the fiber becomes single mode, which is seen when the power output no longer exhibits oscillations [27, 42]. This process results in fibers whose optical mode has an evanescent tail in the air and therefore can be coupled to a microdroplet resonator by bringing the fiber in close proximity to the microdroplet.

An additional step in the fiber tapering process adds a dimple to the fiber. This dimple allows for coupling to a wider range of devices, such as photonic integrated circuits [42, 43]. On-chip devices are difficult to couple to using tapered fibers, as the thick ends of the fiber may touch the device surface before the thin center is close enough for optical coupling. Additionally, the tapered fiber is long and straight, and as such it is hard to confine coupling to a single region when addressing a planar surface. Dimpling the fiber solves both these problems. The dimple is formed by bending the taper around a mold and annealing it, leaving a small dimple at its center. Since this dimple extends further downward than the rest of the fiber, and therefore is closer to the surface than the rest of the fiber, light will couple from the fiber only at the dimple when positioned correctly. In this way, undercut optical structures such as microdisk resonators [42, 44–51] and nanobeams [52–54] can be coupled to. The undercut nature of these devices makes them very difficult to address with on-chip waveguides, as the waveguide will have no supporting material.

We present a fully functional system for the automated fabrication of tapered and dimpled optical fibers. This automation reduces the load of training and fabrication time and ensures consistent fabrication. By integrating motorized stages, a laser source, an oscilloscope, a camera, and a torch into a single unified system, the user is able to fabricate a tapered or dimpled fiber at the touch of a button. The system analyzes output from the oscilloscope and uses computer vision techniques to analyze the camera feed in order to fully automate the tapering and dimpling process. The system is capable of producing tapered and dimpled optical fibers with efficiencies of over 90% with high repeatability. The system requires minimal training for new users and can create a tapered and dimpled fiber in under ten minutes.

1.2 Background

The study of microdroplet resonators and the sophisticated setups that support them hinges on an understanding of several optics and fluidics principles. This section will seek to provide necessary background to understand the principles discussed in this work.

1.2.1 Sessile Droplets

A sessile droplet is a droplet that rests upon a solid surface. Like all droplets, the shape of sessile droplets is strongly determined by the surface tension of the droplet. Surface tension arises from a mismatch between the cohesive and adhesive forces acting on a droplet. Cohesive forces are forces of attraction between molecules of the same type (the liquid) while adhesive forces are the attractive forces between molecules of different materials (water to air or water to the solid surface). When the cohesive forces in a liquid are much stronger than the adhesive forces acting on it (such as a water droplet suspended in air), the cohesive forces pull the droplet into a spherical shape, which is ideal for optical microdroplet resonators, especially because these forces act on each molecule in the liquid, smoothing the surface down to the atomic level. However, when other forces act on the droplet, it will no longer form a spherical shape. In the case of sessile droplets, the most significant forces (other than cohesion) are adhesion to the solid surface and gravity. Gravity is a factor only in large droplets; in small droplets the force of gravity is small compared to other forces. The relative importance of gravity can be determined from the Bond number, B_o , which is calculated as

$$B_o = \frac{\Delta\rho g L^2}{\gamma}, \quad (1.1)$$

where $\Delta\rho$ is the difference in the densities of the liquid and the gas, g is the gravitational constant, L is the characteristic length (for a droplet, the radius), and γ is the surface tension. For a water droplet in air with a radius of 250 μm , the Bond number is 0.0085. A Bond number less than 1 suggests that surface tension dominates over gravity and gravity can be safely neglected.

With the surface tension force dominating gravity, the significant forces in our sessile droplets are the cohesive force of the droplet and adhesion to the surface. These forces play together to create a contact angle between the surface and the droplet. The innate contact angle θ^* is the angle formed by the edge of the liquid droplet and the surface it rests on, as shown in figure 1.1.

As shown in figure 1.1(a), if the contact angle is smaller than 90° , the surface is considered to be hydrophilic (for water-based liquids) or oleophilic (for oil-based liquids). Similarly, if the contact angle is larger than 90° , the surface is considered to be hydrophobic or oleophobic. To create microdroplet resonators, it is desirable that the droplet be as spherical as possible, which makes highly hydrophobic (oleophobic) surfaces ideal. However, the material used in our devices has an innate contact angle of 43° (see figure 1.1(c)). This can be overcome by taking advantage of corner pinning. As a droplet grows, it will maintain the innate contact angle θ^* on a flat surface (see figure 1.1(b i)). However, when the droplet reaches a corner (see figure 1.1(b ii)), the contact angle will grow and the droplet will not advance past the corner until the critical angle θ_c is reached, where ϕ is the angle of the corner. This angle

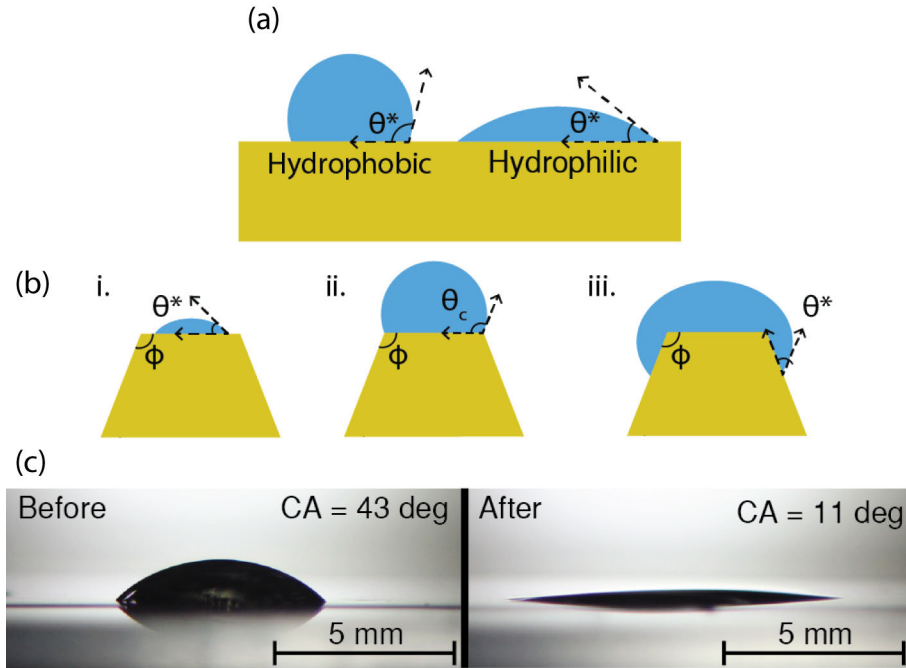


Figure 1.1: Wetting principles of water (oil) droplets. (a) Surfaces with a contact angle $\theta^* < 90^\circ$ are considered hydrophilic (oleophilic), while those with a contact angle $\theta^* > 90^\circ$ are considered hydrophobic (oleophobic) (b) Corner pinning occurs when a growing droplet (i) encounters a sharp corner (ii). In this case, the contact angle will grow until θ_c is reached, at which point the droplet will advance beyond the corner (iii), forming the innate contact angle with the new surface. (c) The innate contact angle of our devices is 43° , but by treating the devices with an oxygen plasma, the contact angle can be reduced to 11° .

is calculated as $\theta_c = 180^\circ - \phi + \theta^*$. Once the critical angle is reached, the liquid advances beyond the corner, with a contact angle of θ^* relative to the new surface (see figure 1.1(b iii)). The contact angle can be reduced by treating the devices with an oxygen plasma. This is useful in situations where it is desirable that the liquid hug the surface.

Because of the low Bond number of our droplets, the contact angle effectively determines the shape of the droplets. By utilizing corner pinning, nearly spherical droplets can be formed even though the material used is hydrophilic.

1.2.2 Evaporation from a Droplet

Though corner pinning allows us to create spherical droplets, water microdroplet resonators have the additional difficulty of evaporation. At the scales used in our experiments, the effects of evaporation become quite significant. We can model the rate of evaporation to better understand what will be required to overcome its effects. The analysis here mirrors that of [55].

The evaporation rate of a spherical droplet can be calculated using Fick's law, given as

$$\frac{dm}{dt} = \rho \frac{dV}{dt} = -D \int \nabla c \cdot dS = -D \int \frac{dc}{dn} dS, \quad (1.2)$$

where m , ρ , and V are the mass, density, and volume of the liquid, n is the normal vector, D is the diffusion coefficient of the liquid vapor, c is the liquid vapor concentration. We can approximate the concentration gradient $\frac{dc}{dn}$ at the droplet surface as

$$\frac{dc}{dn} \approx \frac{c_0 - c_\infty}{r}, \quad (1.3)$$

where r is the radius of the droplet and c_0 and c_∞ are the vapor concentrations at the surface of the droplet and at infinity (the environment). Using this relation, we can express the evaporation rate as

$$\frac{dm}{dt} = 4\pi r D (c_0 - c_\infty). \quad (1.4)$$

Note that the evaporation rate is proportional to the radius of the droplet. For a water droplet in air at lab conditions of 50% humidity at 21° C, $D = 2.43 \times 10^7 \mu\text{m}^2/\text{s}$, $c_0 = 1.85 \times 10^{-17} \text{ g}/\mu\text{m}^3$, and $c_\infty = 9.27 \times 10^8 \text{ g}/\mu\text{m}^3$. For a droplet with $r = 250 \mu\text{m}$, the resulting evaporation rate is $dm/dt = 7.05 \times 10^{-7} \text{ g/s}$. To make this number more meaningful, we can relate it to the rate of change of the radius of the droplet. Using the equation for the volume of a sphere $V = \frac{4}{3}\pi r^3$, we can find the derivative as

$$\frac{dm}{dt} = \rho \frac{dV}{dt} = \rho 4\pi r^2 \frac{dr}{dt}. \quad (1.5)$$

Using the evaporation rate determined above and $\rho = 9.97 \times 10^{-13} \text{ g}/\mu\text{m}^3$, we find that $\frac{dr}{dt} = 0.90 \mu\text{m/s}$. This rate is inversely proportional to the radius of the droplet, so as the droplet begins to shrink from evaporation, it will shrink faster as the droplet radius decreases. The size change of water droplets due to evaporation is a key challenge to overcome when working with water microdroplet resonators, as the resonant wavelength of a microdroplet resonator directly depends on its size.

1.2.3 Whispering Gallery Modes

Microdroplets act as optical resonators because their spherical shape can support whispering gallery modes (WGMs). These modes occur as light within the sphere reflects from its surface at near-grazing incidence angles. The resulting path brings the light back around the edge of the sphere. If the light is at a resonant wavelength, the light that has traversed the sphere will be in phase with new light entering the sphere, resulting in constructive interference. Because the surface is spherical, modes will exist with varying numbers of nodes in the radial, polar, and azimuthal directions, denoted by the mode numbers n , l , and m , respectively. An example of a WGM is given in figure 1.2, where the

figure represents a cross section of a water droplet with radius $r = 250 \mu\text{m}$. This WGM has a radial mode number of $n = 3$ (seen horizontally), a polar mode number $l = 2$ (seen vertically), and an azimuthal mode number $m = 2180$ (“into the page”).

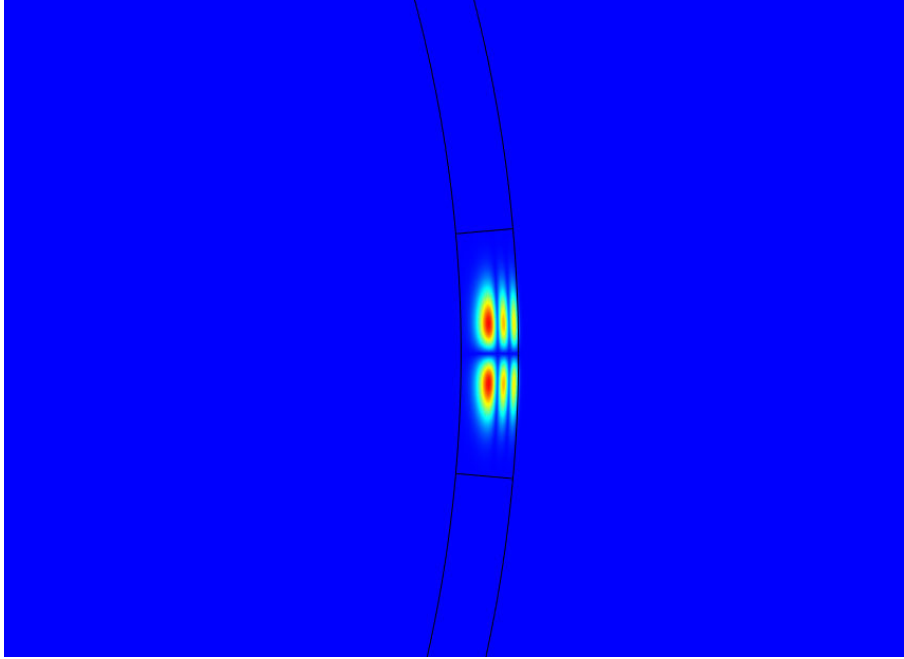


Figure 1.2: An example of a whispering gallery mode. This WGM is modeled on a water droplet with $r = 250 \mu\text{m}$. It has mode numbers $n = 3, l = 2, m = 2180$.

The resonant frequencies of the modes can be approximated as

$$\lambda_{0,m} \approx \frac{2\pi r n_{drop}}{m}, \quad (1.6)$$

where $\lambda_{0,m}$ is the free-space wavelength of the mode, m is the azimuthal mode number, r is the radius of the droplet, and n_{drop} is the refractive index of the liquid. Because modes of similar wavelength can be excited by changing n and l , we see many modes in our experimental results. We can find the free spectral range (*FSR*) of a single mode by finding the difference between the resonant wavelength of two adjacent azimuthal modes, that is, $FSR = \lambda_{0,m} - \lambda_{0,m+1}$. For a water droplet ($n_{drop} = 1.3$) with $r = 250 \mu\text{m}$ using $m = 2190$ (to give resonant wavelengths near 930 nm), we find that $FSR = 0.425 \text{ nm}$.

1.2.4 Quality Factor of Resonators

Optical resonators can be characterized by their quality factor (Q), which is a measure of how long it takes for the light in a resonator to decay. Similarly, the Q of a resonator can be thought of as a metric for how many times the light will circle the resonator before escaping. The quality factor of a resonator can be expressed as [56]

$$Q = 2\pi\nu_0\tau_p, \quad (1.7)$$

where ν_0 is the free-space frequency of the light and τ_p is the photon lifetime in the resonator. This relation can also be expressed as

$$Q = \frac{\nu_0}{\delta\nu}, \quad (1.8)$$

where $\delta\nu$ is the full width half max (FWHM) spectral linewidth of the resonance. The Q of a resonator can be directly measured using either of these relations. The photon lifetime can be observed by exciting a resonator, then turning off the excitation source and observing the power decay. This is known as a ring-down measurement. However, it is often more straightforward to measure the linewidth of the resonant peaks. By sweeping a laser's wavelength in time and measuring the power, a spectral response of the resonator can be obtained, then the linewidth can be measured. Since our laser output is set via wavelength, we can convert equation 1.8 to wavelength as

$$Q = \frac{\lambda_0}{\delta\lambda}, \quad (1.9)$$

where λ_0 is the free-space wavelength and $\delta\lambda$ is the FWHM linewidth of the resonant peak. The shape of the resonant peak is a Lorentzian. The derivation of this line shape is given in chapter 2.

The overall Q of a microdroplet resonator can be expressed as a combination of contributing Q factors associated with various loss mechanisms. As such we can express the overall Q as [57]

$$Q^{-1} = Q_{ab}^{-1} + Q_s^{-1} + Q_{rad}^{-1} \quad (1.10)$$

where Q_{ab} is the Q related to material absorption, Q_s is the Q related to surface scattering, and Q_{rad} is the Q related to radiative losses. Based on this relationship, the maximum value of Q is limited to the lowest of the contributions from loss mechanisms.

In our devices, the curvature is relatively large. Because radiative losses decay exponentially with increasing resonator size, at large droplet sizes relative to the wavelength, Q_{rad} becomes very large. A benchmark is that if $D/\lambda_0 \geq 15$, then $Q_{rad} > 10^{11}$ (where D is the droplet diameter and λ_0 is the free-space wavelength) [57]. In our devices, $D/\lambda_0 \approx 500$, so Q_{rad} will be large enough to be negligible.

The material absorption Q can be calculated by

$$Q_{ab} = \frac{2\pi n}{\alpha\lambda_0}, \quad (1.11)$$

where n is the refractive index of the resonator material and α is the absorption coefficient of the material.

We expect Q_s to be large enough to not limit the Q of the resonator, since surface scattering losses depend upon surface roughness, and the surface tension of liquid droplets will eliminate any roughness.

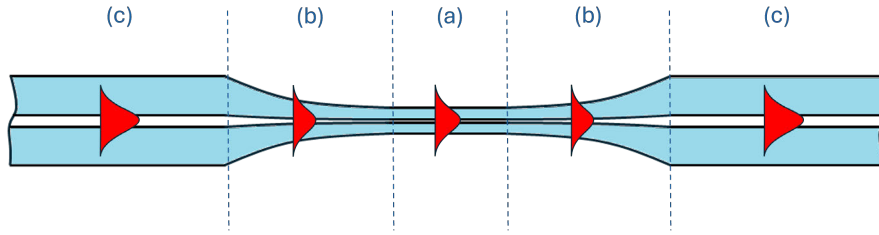


Figure 1.3: Schematic of the optical mode of a tapered optical fiber. The regions labeled (c) represent the fiber at its standard width. Region (b) shows the transition region, where multiple modes can exist. Region (a) shows the single mode taper. Note that in this region, the evanescent field of the mode extends into the air around the fiber.

1.2.5 Tapered Fiber Coupling

Tapered optical fibers provide a convenient method for coupling light from a fiber into a microdroplet resonator. We fabricate these fibers in-house from Corning SMF-28 fiber. Tapered fibers rely on decreasing the diameter of the fiber such that the evanescent field of the guided mode extends into the air. Figure 1.3 shows a schematic representation of the optical mode as it propagates through a tapered fiber [58]. In the regions labeled (c), the fiber is at its standard width, with the light being guided by the core/cladding interface. In this region, the evanescent field of the mode extends into the cladding of the fiber, but not into the air. In region (b), the fiber has been narrowed sufficiently that the light is no longer guided exclusively by the core/cladding interface. Multiple modes exist in this region, guided at the fiber/air interface. The presence of multiple modes is often undesirable, so the fiber is tapered further to ensure single mode performance. In region (a), the fiber has been tapered sufficiently to support only a single optical mode. This mode is guided by the fiber/air interface, and the evanescent field extends into the air. As the fiber widens back to its full width, the light is coupled back into the core/cladding mode. The taper diameter d is typically less than $1\ \mu\text{m}$.

Because the light in the tapered region has an evanescent field extending into the air, light can be coupled from the fiber into a microdroplet resonator if the resonator is brought sufficiently close to the fiber.

Single mode operation in a fiber is determined by the fiber parameter V_f [56]. The fiber parameter can be used to determine the number of modes a fiber can support. For the case of a single mode fiber, the fiber parameter must meet the requirement $V_f = 2.405$. We can calculate V_f as

$$V_f = 2\pi \frac{a}{\lambda_0} NA, \quad (1.12)$$

where a is the radius of the core of the fiber, λ_0 is the free-space wavelength of the light, and NA is the numerical aperture of the fiber. NA is found through the relation

$$NA = \sqrt{n_1^2 - n_2^2}, \quad (1.13)$$

where n_1 is the refractive index of the core of the fiber and n_2 is the refractive index of the cladding. Using these equations, we can determine how small the fibers must be tapered to have single mode performance. For the tapered fibers, the core is the glass fiber and the cladding is air. As such, $n_1 = 1.468$ (from Corning) and $n_2 = 1$. The resulting numerical aperture is $NA = 1.077$. Using this, we can calculate the single mode cutoff radius at both 1550 nm and 930 nm (the wavelengths used in our experiments). For light at 1550 nm, the taper will become single mode when $a < 551$ nm, and for 930 nm light, the taper will become single mode when $a < 330$ nm.

To create single mode fibers, our fabrication process typically relies on observing the optical transmission of the fiber during the pulling process, since it is difficult to accurately measure the fiber in real time at the scales needed to achieve single mode operation. This process involves observing the interference patterns between multiple modes as the fiber is tapered and is discussed more fully in chapter 6.

3D Printed Mounts for Microdroplet Resonators

This chapter is composed from a paper entitled “3D Printed Mounts for Microdroplet Resonators” published in the journal *Optics Express* [59]. I hereby confirm that the use of this article is compliant with all publishing agreements.

2.1 Introduction

Microdroplet resonators provide a powerful tool in the fields of biology, optics, and physics. In biology, they are useful for sensing applications due to their biocompatibility and versatility [10, 11]. They are used in optics to study lasing [3–5, 9] and nonlinear effects [12, 13]. In physics, they can be used to excite optomechanical effects [12, 14] and for material analysis and sensing [15–17]. Among the benefits of microdroplet resonators is their innate smoothness and versatility.

Currently, common methods for creating and positioning liquid microdroplet resonators include suspending a droplet on a glass stem [14, 20, 27], placing a droplet on a hydrophobic surface [25], suspending a droplet in another liquid [4, 12, 22, 23], and manipulating the droplet using optical tweezers [22, 23]. These methods cover a wide range of complexity, control, and ease of use, with trade-offs among the three.

At the same time, three-dimensional (3D) printing has been used in many fields as a method for rapidly developing custom, inexpensive devices. In recent years, the precision of 3D printing has increased dramatically [31, 32], making it an attractive alternative to other fabrication methods. In the field of optics, 3D printing has been used to create whispering gallery mode (WGM) resonators [60, 61]; however, to date, no research combining the benefits of 3D printing with those of liquid microdroplet resonators has been demonstrated. In this paper, we demonstrate for the first time 3D printed mounts for microdroplet resonators. The flexibility of the design and rapid fabricate-test-redesign cycle allows us to engineer mounts that allow for both increased coupling stability and tailored features such as resonator shape, size, and type of liquid.

2.2 Methods

2.2.1 Device Fabrication

To fabricate the devices, a custom digital light processor stereolithographic (DLP-SLA) printer with a 365 nm LED light source and a pixel pitch of 7.6 μm in the plane of the projected image was used [32]. A custom photopolymerizable resin was used that consists of poly(ethylene glycol)diacrylate (PEGDA, MW258) with a 1% (w/w) phenylbis(2,4,6-trimethylbenzoyl)phosphine oxide (Irgacure819) photoinitiator and a 2% (w/w) 2-nitrophenyl phenyl sulfide (NPS) UV absorber [31]. The 3D printed devices were fabricated on diced and silanized glass slides. Each slide was prepared by cleaning with acetone and isopropyl alcohol (IPA), followed by immersion in 10% 3-(trimethoxysilyl)propyl methacrylate in toluene for 2 h. After silane deposition, the slides were kept in toluene until use. In a typical device, each build layer of the print is exposed to a measured optical irradiance of 21.2 mW/cm^2 in the image plane for 400 ms, with a layer thickness of 10 μm . Adjustments to the irradiance and exposure time were made as necessitated by device geometry. After printing, unpolymerized resin in interior regions is gently flushed with IPA, followed by device optical curing for 30 min in a custom curing station using a 430 nm LED having a measured irradiance of 11.3 mW/cm^2 in the curing plane.

In some cases, the devices were exposed to an oxygen plasma in a Technics PEII plasma etcher for 2 min at 200 W in order to make the device polymer more hydrophilic. The increased hydrophilicity is maintained while the device is coated in water; however, airborne contaminants cause the polymer to return to its nominal hydrophilicity after 8–10 hours of exposure to air.

2.2.2 Design Considerations

This work builds upon our previous work, in which we combined the capabilities of advanced 3D printing techniques [31] and nano-water bridges [20], to create a device that was coated in a self-sustaining thin film of water [55] (referred to as thin-film devices hereafter), as shown in figure 2.1. To make these devices suitable for sustaining high quality optical resonance, several modifications were introduced. The thin-film devices consist of a frustrum base and a rounded head, with a central capillary allowing water recirculation. Figure 2.1(a) shows a scanning electron microscope (SEM) image of the thin-film device, which clearly exhibits the roughness and pixelation inherent in 3D printed devices. This roughness is eliminated, however when coated in a thin liquid film, as seen in figure 2.1(b). The device is exposed to an oxygen plasma to make it highly hydrophilic. This allows a thin film to be formed and maintained passively through surface wetting and capillary action. The smoothing film of water can be maintained with high stability over an extended period of time, even in the presence of evaporation, provided there is a reservoir of water at the base of the device [55].

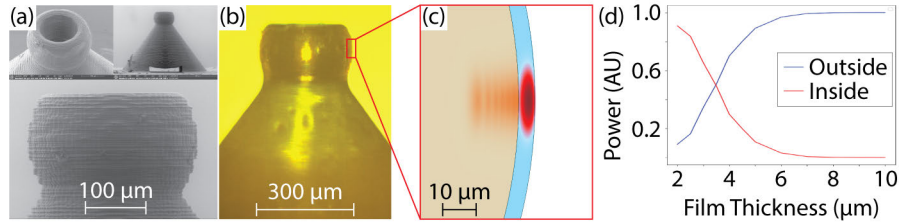


Figure 2.1: (a) SEM image of the water recirculation device, which highlights the surface roughness of 3D printed devices. (b) The water recirculation device coated with a thin film of water. (c) The fundamental R polarized mode of the thin film device with a film thickness of 5 μm . The 3D printed device is shown in tan, the water in light blue, and air in white. (d) Comparison of optical power inside and outside the 3D printed material as a function of water film depth.

Nonetheless, the optical quality Q of the device is reduced owing to penetration of the optical mode into the lossy 3D printed resin. In order to create a 3D printed liquid microdroplet resonator with a high quality factor Q , the liquid film must be thick enough that the optical mode does not penetrate the 3D printed material. Figure 2.1(c) shows the fundamental mode for light with the electric field primarily oriented in the radial direction (R polarized) for the thin-film device with a film thickness of 5 μm . The 3D printed material is shown in tan, with the water film being shown in light blue and air in white. To estimate the minimum required thickness, we simulated the mode profile for several film thicknesses and calculated the fraction of the optical power propagating inside the 3D printed material, as shown in figure 2.1(d). We compared this to the power propagating outside the 3D printed material (i.e., in the water and the air). As expected, devices with thicker films have less interaction with the lossy 3D printed material, and the simulation suggests that a minimum film thickness of 8–10 μm is required for a high Q resonator.

In order to create films of adequate thickness, careful balancing of liquid-liquid cohesive forces and liquid-solid adhesive forces was required, with many design-test cycles. As the liquid spreads across a solid, adhesive and cohesive forces interact, resulting in the liquid edge meeting the solid at a given angle, known as the contact angle θ^* , as seen in figure 2.2(a). The more hydrophilic a material is, the smaller its contact angle will be. A result of the contact angle is corner pinning, a phenomenon in which an advancing liquid cannot proceed around a corner boundary at the native contact angle. Rather, the localized volume of the liquid will increase, with the solid-liquid interface increasing in angle until the critical angle θ_c is reached, where $\theta_c = (180 - \phi) + \theta^*$ and ϕ is the angle of the corner boundary relative to a flat surface.

The surface roughness of the resin resulting from the 3D-printing process creates many corner boundaries. The native contact angle of the 3D printed material was measured to be 43° , which is too high to overcome the corner boundaries and prevents the devices from wetting completely. By treating the devices with an oxygen plasma, the contact

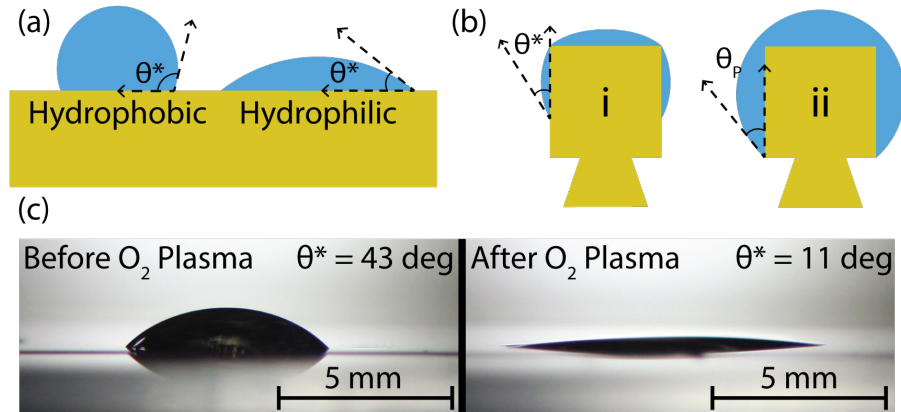


Figure 2.2: (a) Example of hydrophobic and hydrophilic innate contact angles θ^* . (b) Devices showing the effects of corner pinning. The liquid in (i) does not exhibit corner pinning, and thus the contact angle is θ^* . In (ii) the liquid is pinned at the bottom corner, and the angle formed is θ_p such that $\theta^* < \theta_p < \theta_c$. (c) Our devices are sometimes treated by exposing them to oxygen plasma, which reduces the contact angle.

angle was reduced to 11° , as seen in figure 2.2(c), allowing the creation of a stable film that overcomes the corner boundaries. However, owing to the hydrophilicity of the resulting plasma-treated material, the adhesive forces result in a film of water that is $< 2 \mu\text{m}$ [55].

To increase the film thickness, we sought a design that would create a larger contact angle while maintaining a droplet shape. Through over 30 design-test cycles we explored the design space of our 3D printed devices. We created designs that implemented microfluidic systems, hydrophobic microstructuring, and unique geometries, all of which were made practical by the rapid fabrication times and design flexibility of the 3D printing process, which are not available using standard fabrication techniques. The best results were achieved by leveraging corner pinning at the lower boundary of the device head. To accomplish this, we adjusted our design to include a sharp undercut at the bottom of the device head, another geometry that can be difficult to fabricate using traditional stereolithography techniques. Pinning allows for a larger contact angle at the corner boundary. Figure 2.2(b) shows this effect. As liquid is added to the device head, the solid-liquid boundary advances down the side of the head at the innate contact angle θ^* , as seen in figure 2.2(b i). Then, when sufficient liquid has been added, the liquid will pin at the bottom edge of the head as shown in figure 2.2(b ii). The resulting contact angle θ_p will obey $\theta^* < \theta_p < \theta_c$, allowing a thicker film to be formed.

Figure 2.3 shows an example device utilizing our final design. Figure 2.3(a) shows a profile view of the 3D printed mount. The device consists of a frustrum base with a chamfered cylindrical head. In an unsupported system, the surface tension of droplets forces them into a spherical shape. To mirror this, the heads of our devices are designed such that the diameter and the height are equal. Figure 2.3(b) shows a microdroplet

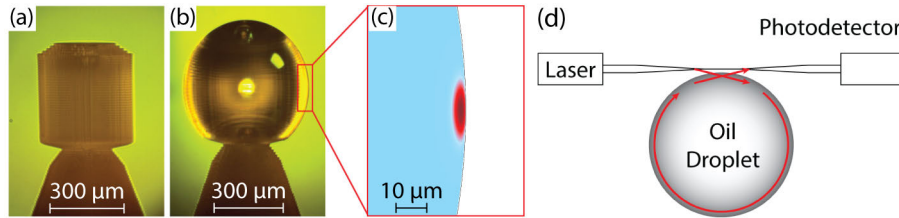


Figure 2.3: (a) 3D printed device for supporting microdroplet resonators. (b) Paraffin oil droplet supported by the 3D printed device. (c) Fundamental Z polarized mode of the droplet. Oil is shown in light blue, and air is shown in white. (d) Visualization of the experimental setup. After an optical fiber is tapered, a 3D printed device supporting a microdroplet is brought close enough to the fiber to enable evanescent coupling. The throughput is monitored to determine resonance qualities.

supported by our 3D printed mount. In figure 2.3 paraffin oil (Sigma Aldrich 76235) was used for the microdroplets, though our devices support the use of other fluids. Two constraints are observed in the creation of droplets that allow for control of droplet size. First, the corner boundary at the bottom of the head must not be overcome. When an excess of liquid is added to the droplet, the critical angle is overcome and the liquid flows down the entire device, resulting in a loss of curvature and thickness of the film. The second feature is the smoothness over the top corner boundary of the head. When an insufficient amount of liquid is placed on the head, there is not a smooth interface between liquid on the top of the head and liquid on the sides. This results in a corner at the top of the head. While the film formed in this manner can be thick enough to support the optical mode, the film is less stable than when a smooth interface is formed. These two features result in upper and lower bounds on the droplet size, and these bounds are determined by the size of the 3D printed head. In this way, we can constrain the droplet size to a specific range by scaling the 3D printed mount.

2.2.3 Experimental Procedure

We create droplets on the device by dipping a bare optical fiber in liquid and then touching the fiber to the head of the device. Figure 2.3(c) shows the calculated fundamental mode for light polarized in the vertical direction (Z polarized) for a spherical paraffin oil droplet with a radius of 243.5 μm, the measured radius of the droplet shown in figure 2.3(b). Note that the mode size is consistent with that of the thin-water film devices, and the droplets form a film approximately 50 μm thick.

Figure 2.3(d) shows the optical coupling setup of our experiments, which use a tapered optical fiber and a tunable laser. The fiber is tapered using a heat-and-pull rig similar to those used in [27, 40–42]. To determine the pull length, the optical throughput of the taper is monitored, and the pull is stopped when the fiber becomes single mode [27, 42]. The droplets are then carefully brought into close proximity to the fiber to allow coupling into the resonant modes. The coupling efficiency is carefully monitored to ensure the microdroplet did not come into contact

with the fiber. On occasions when there is a strong attraction between the fiber and the droplet, or when the two come into contact, the fiber requires cleaning. The tapered fiber is rinsed with isopropyl alcohol, then deionized water, and, in some cases, the pulling stages are used to add tension to the fiber. Through this careful cleaning and tensioning of the fiber, we are able to maintain a stable coupling distance between the fiber and resonator, allowing us to control coupling efficiency, adjust polarization, and collect spectral data.

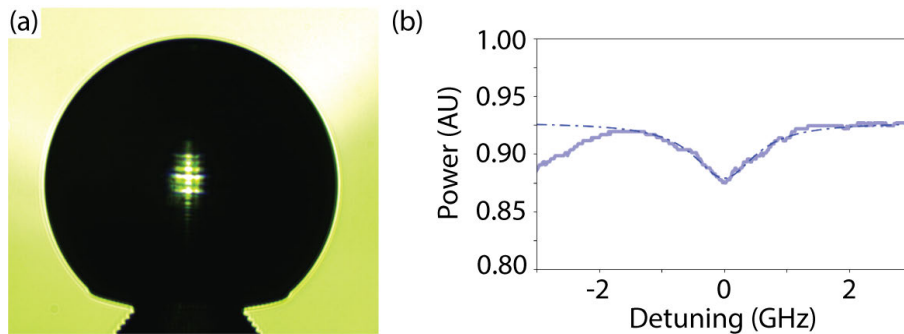


Figure 2.4: (a) Profile view of a water/glycerol microdroplet of radius $257.9 \mu\text{m}$ supported by a 3D printed device. (b) Z polarized resonant peak of water/glycerol droplet, fitted with a Lorentzian.

2.3 Results

Using this stable coupling, we were able to collect many data sets for varied resonator types. As these devices do not have a mechanism to overcome evaporation, non-evaporating liquids were used. Figure 2.4(a) shows a profile view of a droplet formed from a water/glycerol mixture. The droplet has a measured radius of $257.9 \mu\text{m}$. Figure 2.4(b) shows a resonant peak of the droplet, having a central wavelength of 931.2133 nm and a quality factor of $Q = 1.7 \times 10^6$. The magnitude of the quality factor suggests that there was no penetration of the mode into the 3D printed material.

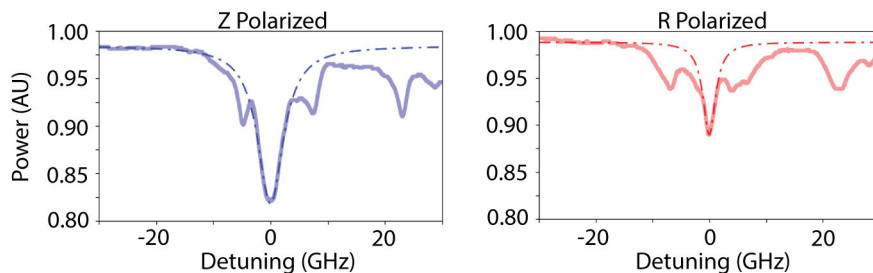


Figure 2.5: Resonance of a paraffin oil droplet fitted to a Lorentzian at both Z and R polarizations.

Figure 2.5 shows resonant peaks of a paraffin oil microdroplet with a radius of $217.8 \mu\text{m}$ at both Z and R polarizations.

Boundary conditions from Maxwell's equations do not allow the R polarized mode to have a continuous electric field across the edge of the droplet. As a result, the R polarized mode will have higher confinement to the resonator than the Z polarized mode. This leads to the R polarized mode having a smaller evanescent field and thus a lower coupling efficiency, as seen when comparing the two plots of figure 2.5.

The peaks in these plots were fitted to a Lorentzian by using a rate equations model:

$$\begin{aligned} \dot{b} &= j(\omega - \omega_0)b - k_0b - k_1b + j\sqrt{2k_1}s_+ \\ s_- &= s_+ + j\sqrt{2k_1}b \end{aligned} \quad (2.1)$$

where $|b|^2$ is the energy inside the resonator, ω is the optical frequency, and ω_0 is the resonant frequency of the microdroplet. k_1 represents the coupling rate between the resonator and the fiber, and k_0 is the intrinsic loss rate of the resonator. Finally, $|s_+|^2$ and $|s_-|^2$ are the optical power at the input and output of the fiber, respectively.

We can find the steady state of the rate equations, which is given in equation 2.2. Using this equation, we fit $|s_-|^2$ to the optical power at the photodetector.

$$\begin{aligned} b_{ss} &= \frac{j\sqrt{2k_1}}{-j(\omega - \omega_0) + k_0 + k_1} s_+ \\ s_- &= s_+ + j\sqrt{2k_1}b_{ss} \end{aligned} \quad (2.2)$$

After fitting the peaks, we found their quality factor (Q) using the relation $Q = \omega_0/2(k_0 + k_1)$, given that the linewidth of the peaks is $2(k_0 + k_1)$. The R polarized peak has a quality factor of $Q = 2.23 \times 10^5$ with the resonant wavelength being 1552.19589 nm. The Z polarized peak has a quality factor $Q = 4.55 \times 10^5$ with wavelength 1554.169066 nm. The Q of the resonances varies across the spectrum for each polarization. Throughout our experiments, both polarizations typically have peaks with Q ranging between 2×10^5 and 5×10^5 .

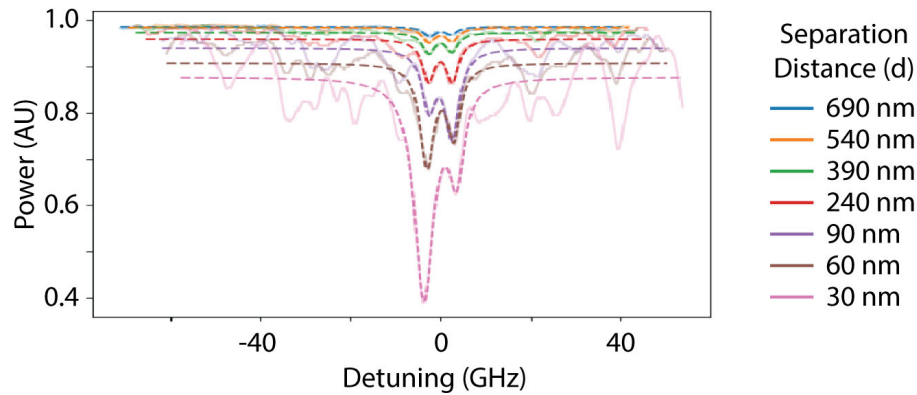


Figure 2.6: Comparison of coupling distance and coupling efficiency using Z polarized light for a paraffin oil microdroplet resonator supported by a 3D printed base.

In another experiment, we were able to observe coupling efficiency as a function of taper-droplet separation distance. Figure 2.6 shows a single resonant peak of a paraffin oil droplet with data collected at many different coupling distances (d) at the Z polarization. The R polarized data (not shown) is very similar. The spectral data was collected by first positioning the droplet at a distance outside the coupling regime ($d \approx \infty$). Then the droplet was carefully moved closer to the fiber until resonant peaks were observed. Spectral data was acquired for each polarization (Z and R), a process which took just under a minute to complete. Then the resonator was moved by increments Δd closer to the fiber, first with $\Delta d = 150$ nm, then with $\Delta d = 30$ nm. The process was repeated until the droplet came into contact with the fiber. Contact between the droplet and the fiber provided a reference for $d = 0$, which we then used to find all the coupling distances. After collection, the data was normalized to the non-coupled transmission spectrum and then fitted with a double-peaked Lorentzian. At a distance of 690 nm from the fiber, the coupling is only about 2% efficient, while at 30 nm the efficiency is near 50%. We note three other features visible in the data. First, there is a slight red shift in the resonant wavelength as the coupling distance decreases, with the peak at the greatest coupling distance being centered at 1554.42233 nm and the peak at the smallest coupling distance being centered at 1554.4402 nm. This effect is likely caused by the thermal dependence in the refractive index of the oil. Second, we see that the resonant peaks are split into doublets, which is due to coupling between modes with significant overlap. In smaller droplets, fewer doublet peaks were observed, since fewer modes are supported by the smaller droplet size. Finally, we observe off-resonance features in the data, which are strongly correlated with the coupling distance. We believe these features indicate coupling to higher-order modes in the droplet.

One of the benefits of using our 3D printed mounts to support the droplets is the mounts' versatility. In conjunction with our precision coupling method, this versatility allows for various microdroplet resonators to be tested with no changes to the tapered fiber or any of the other optical components, ensuring that all changes are caused by the droplet. The mounts can be used with various liquids, and the size and shape of the mounts can easily be changed, resulting in corresponding changes to the microdroplet resonators. In our experiments, our mounts allowed us to create microdroplets of paraffin oil, silicone oil, and glycerol with diameters between 300 μm and 600 μm . Furthermore, we created mounts with racetrack-shaped cross sections, which supported ellipsoidal droplets of eccentricities as extreme as 0.58.

2.4 Conclusion

In conclusion, we present a unique 3D printed mount for optical microdroplet resonators. These mounts provide a robust and easy-to-use method for supporting microdroplet resonators while still allowing control over the droplet position, shape, and size. In our experiments,

we found that the main deterrent to creating smaller droplets was the difficulty of placing the liquid on the mount by hand. We believe that with a more precise delivery method, the droplet size could be decreased dramatically.

In our future work, we hope to further explore the creation and implications of non-spherical microdroplet resonators, in addition to reducing the size of our mounts. We will also integrate 3D printed microfluidic systems that will allow us to deliver liquid to smaller devices and dynamically change the nature of the liquid used in the microdroplets by changing its volume or introducing analytes.

Self-Sustaining Water Microdroplet Resonators Using 3D Printed Microfluidics

This chapter is composed from a paper entitled “Self-Sustaining Water Microdroplet Resonators Using 3D Printed Microfluidics”, published in the journal *Nanomaterials*[62]. I hereby confirm that the use of this article is compliant with all publishing agreements.

3.1 Introduction

Microdroplets have long been used as optical resonators [1]. The surface tension of microdroplets creates a perfectly spherical shape with no surface roughness, making them ideal optical resonators. While many liquids can be used for microdroplet resonators [2], this work focuses specifically on water microdroplet resonators. Water droplet resonators are an ideal tool for biological studies due to the importance of water for life [10, 11].

In one study [11], the researchers created a biolaser by suspending bacteria in a microdroplet. These bacteria expressed a fluorescent protein that acted as a gain medium when the droplet was excited with a pump laser. The researchers were even able to create a stable laser using a droplet containing only one bacterium. Such a result would have been extremely difficult to obtain without the use of a water droplet resonator. A solid material would not allow the cells to have sufficient optical interaction with the laser mode, and a water environment was needed to keep the cells alive.

Water droplet resonators have also been shown to enhance our understanding of physical phenomena present in liquids. In one study [28], the researchers were able to characterize capillary waves present on a droplet’s surface by analyzing the droplet’s optical resonance. These angstrom-scale waves have implications in the coalescence of droplets and the spontaneous rupture of liquid films. By using a water microdroplet resonator, the researchers were able to amplify the effects of these capillary waves on the circulating light, providing greater sensitivity in their characterization over other methods.

Additionally, water microdroplet resonators have been used to construct dye lasers[6, 7] and Raman lasers[8]. Water resonators also present unique opportunities as a subject of study for tuning resonances [6, 18, 19] and producing resonators with high quality factors (Q) [20, 21]. In

our work, we present a new platform that will facilitate future studies involving water microdroplet resonators.

Water microdroplet resonators can be challenging to study because of the rapid evaporation of water, which causes the droplet to change size. This effect is especially pronounced at the small scales used for optical resonators. Typical methods to overcome evaporation involve either adding a stabilizer to the water, controlling the droplet environment, or both [26]. Stabilizing agents can be added to water so that the evaporation rate is decreased. This results in the droplet reaching equilibrium at humidities less than 100%. The most common stabilizers are glycerol [7, 11, 18, 21] and salt [19, 24]. Glycerol is hygroscopic, allowing it to absorb water from the air to establish equilibrium. Salt lowers the vapor pressure of water with similar results. Alternatively (or additionally), the droplet environment can be controlled by either keeping the droplet in a humidity-controlled chamber [6, 8, 26] or submerging the droplet in another liquid [30].

Though water naturally forms smooth spherical droplets in a free environment, typically a droplet must be attached to a surface to create a usable optical device. However, surface adhesion can degrade the shape of the droplet for use as a microresonator. This difficulty can be overcome by manipulating the droplet using optical tweezers [24], but ideally the droplet is supported for device functionality and optical interrogation. Past work has demonstrated supporting water microdroplets by placing them on a hydrophobic surface [6–8, 11, 18, 19, 21, 26] or suspending droplets from a glass stem [20, 28, 29]. These methods, in addition to using optical tweezers, all maintain the droplet in a sufficiently spherical shape to establish optical resonance. The droplets can be formed on these support systems a number of ways, but the most common is to atomize the liquid over a surface or drop an individual droplet onto the support using a pipette or similar tool. Though these methods effectively create droplets of a sufficiently small size (<1 mm), precise control over the size of the droplet is not reported.

We propose a novel solution for droplet formation, support, size control, and stabilization against evaporation. Our design incorporates a microfluidic system that allows us to precisely control the size of the droplet upon formation, which has been used for non-evaporating oil droplets [5] but to our knowledge has not been demonstrated for water microdroplets. Our microfluidic system further serves to provide a constant flow of water to the microdroplet from an external reservoir, completely mitigating the effects of evaporation on the droplet without requiring the addition of a stabilizer to the droplet or a specialized environment. Other methods have been shown to replenish the droplet against evaporation [20], though these did not seek to control droplet size. The microfluidic system we present feeds into a specially designed 3D-printed mount that supports the droplet in a spherical shape and allows for precise droplet positioning. Using this device, we demonstrate water microdroplet resonators that can be tailored to an arbitrary size and are stable against evaporation without requiring additives to the

water or a controlled environment.

3.2 Materials and Methods

3.2.1 Device Fabrication

To fabricate the devices, a custom digital light processor stereolithographic (DLP-SLA) printer with a 365 nm LED light source and a pixel pitch of 7.6 μm in the plane of the projected image was used [32]. A custom photopolymerizable resin was used that consists of poly(ethylene glycol)diacrylate (PEGDA, MW258) with a 1% (*w/w*) phenylbis(2,4,6-trimethylbenzoyl)phosphine oxide (Irgacure819) photoinitiator and a 2% (*w/w*) 2-nitrophenyl phenyl sulfide (NPS) UV absorber [31]. The 3D-printed devices were fabricated on diced and silanized glass slides. Each slide was prepared by cleaning with acetone and isopropyl alcohol (IPA) followed by immersion in 10% 3-(trimethoxysilyl)propyl methacrylate in toluene for 2 h. After silane deposition, the slides were kept in toluene until use. For a typical device, each build layer of the print is exposed to a measured optical irradiance of 21.2 mW/cm^2 in the image plane for 400 ms, and each layer has a thickness of 10 μm . Adjustments to the irradiance and exposure time were made as necessitated by device geometry. After printing, unpolymerized resin in interior regions was gently flushed with IPA, followed by device optical curing for 30 min in a custom curing station using a 430 nm LED with a measured irradiance of 11.3 mW/cm^2 in the curing plane.

3.2.2 Design Considerations

The devices were designed to create spherical droplets by leveraging corner pinning. In a system wherein a droplet is supported by a solid surface, the cohesive forces within the droplet and the adhesive forces between the liquid and the solid result in the liquid edge meeting the solid at a given angle, known as the innate contact angle θ^* . As seen in figure 3.1(a), materials with an innate contact angle $\theta^* < 90^\circ$ are considered hydrophilic, while those with $\theta^* > 90^\circ$ are hydrophobic. Hydrophobic surfaces are desirable for microdroplet resonators, as their low adhesive forces allow droplets to become nearly spherical due to surface tension; however, by creating structures with corners, we are able to use a hydrophilic material ($\theta^* = 43^\circ$) to create our devices. In our devices, as water is added to the top of the device, the contact angle is initially the innate contact angle θ^* , as in figure 3.1(b). To increase the apparent contact angle, we take advantage of corner pinning, as shown in Figure 3.1(c). Corner pinning is a phenomenon in which an advancing liquid cannot proceed around a corner boundary at the native contact angle. Rather, the localized volume of the liquid will increase without advancing around the corner, with the solid–liquid interface increasing in angle until the critical angle θ_c is reached, where $\theta_c = (180 - \phi + \theta^*)$ and ϕ is the angle of the corner boundary relative to a flat surface. The result is a pinned contact angle θ_p , where $\theta^* < \theta_p < \theta_c$, which allows us

to create spherical droplets on surfaces that are innately hydrophilic by supporting the droplets on posts with corner boundaries. Our design further leverages corner pinning using a re-entrant structure, wherein the undercutting of the head creates an additional corner boundary. If the droplet advances from the top of the device and along its side, the droplet pins on the bottom edge, creating an effective contact angle $\theta_{eff} = \theta_p + 90^\circ$ (see figure 3.1(d)).

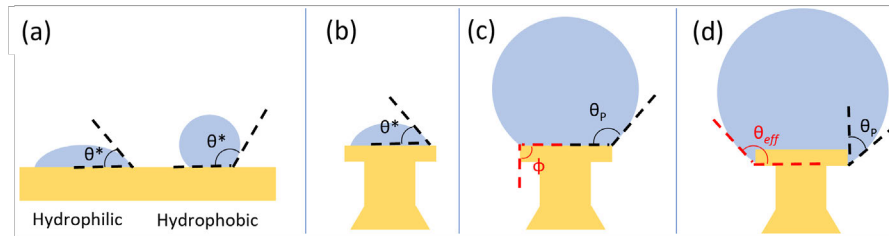


Figure 3.1: (a) Innate contact angle θ^* of a droplet on hydrophilic and hydrophobic surfaces. (b) Initially, no corner pinning is present, so the contact angle is θ^* . As the drop grows, the liquid becomes pinned (c) at the top corner, and the angle formed is θ_p such that $\theta^* < \theta_p < \theta_c$. Further growth causes corner pinning on the bottom edge (d), which allows larger droplets to be formed, and the effective contact angle θ_{eff} becomes $\theta_p + 90^\circ$.

This re-entrant design allows the head to support larger droplets and increase the effective contact angle from the innate $\theta^* = 43^\circ$ to the effective contact angle $\theta_{eff} = 130^\circ$, which helps to create more spherical droplets. Figure 3.2(b) and (c) show a model and microscope image of our device, respectively. Our device's dimensions are based on the fact that the 3D printer has a pixel size of $7.6 \mu\text{m}$ and a layer thickness of $10 \mu\text{m}$. As such, all dimensions are designed to be multiples of this pixel size, and we provide the design parameters here. The device consists of a chamfered square base with side length $176 \mu\text{m}$ and a square pillar $50 \mu\text{m}$ tall and $76 \mu\text{m}$ wide. These are topped with a square head that is $106.4 \mu\text{m}$ wide and $10 \mu\text{m}$ thick. Water is supplied to the top of the head by a square channel $45.6 \mu\text{m}$ wide that cuts through the head, column, and base. The channel connects to larger openings that accommodate external tubing. The device was designed to accommodate as small a structure as possible while ensuring the device could be reliably fabricated.

3.2.3 Microfluidic System

The microfluidic system (shown in figure 3.2(a)) functions by providing a constant flow of water to the droplet such that the rate of evaporation from the droplet is matched by the rate of water flowing into the droplet. The flow rate into the droplet can be precisely determined and set by use of our microfluidic system, which was designed on the principle of hydraulic resistance [63]. We here present a theoretical mathematical description of the process.

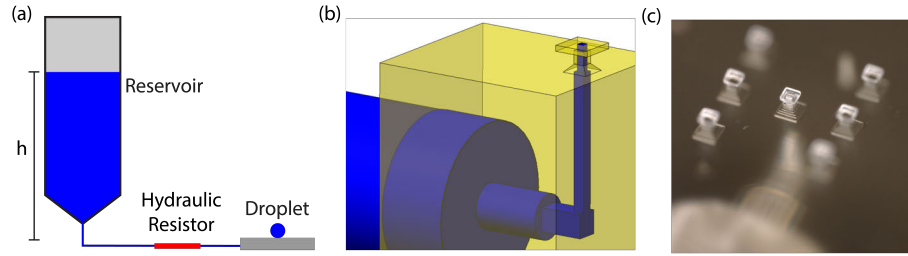


Figure 3.2: Microfluidic system of the devices. (a) The pressure at the hydraulic resistor is determined by the height h of the water reservoir (which is open to the air). This pressure results in constant flow through the resistor, matching the evaporation rate of the droplet. (b) Model of the 3D printed device. The device has a channel to allow water flow and a head with a re-entrant shape to create the corner pinning needed for a spherical droplet. (c) Microscope image of the 3D printed device.

The hydraulic resistance of a microfluidic channel is given by analysis of the Hagen–Poiseuille law, resulting in

$$R_h = \frac{8\mu L}{\pi(r_h)^4} \quad (3.1)$$

where R_h is the hydraulic resistance, μ is the viscosity of the liquid, L is the length of the channel, and r_h is the channel radius for a cylindrical channel. The effective r_h for other channel geometries can be calculated as $r_h = 2A_{cs}/P_{cs}$, with A_{cs} and P_{cs} being the cross-sectional area and perimeter of the channel, respectively. The hydraulic resistance of a channel can be used to determine the flow rate of water (or any liquid) in the channel through the equation

$$F = \frac{\Delta P}{R_h} \quad (3.2)$$

where F is the flow rate, R_h is the hydraulic resistance of the channel, and ΔP is the difference in pressure across the channel. This relation is similar to Ohm’s law for electric circuits and allows us to analyze a microfluidic system by comparing or combining the hydraulic resistances of various microfluidic components as needed. Our system takes advantage of this by incorporating a hydraulic resistor [63].

The hydraulic resistor serves two purposes. The first is to dominate the overall hydraulic resistance of the system. In our system, the hydraulic resistor consists of a 1-cm-long fused silica tube with an inner diameter of 25 μm , giving it a resistance 1000 times greater than the combined resistance of all other microfluidic elements in our system (tubing, 3D-printed channels, etc.). In this way, any variation between devices is negligible, and calculations can safely neglect other microfluidic elements. The second purpose of the hydraulic resistor is to match the desired flow rate to an experimentally convenient reservoir depth (approximately 10 cm).

To match the evaporation rate to the flow rate into the droplet, the height of the water in the reservoir is adjusted. This correct height is

calculated by comparing the rate of evaporation with the flow rate of the microfluidic system. The flow rate F of the hydraulic resistor (which dominates the system) is given by equation 3.2. The pressure P at each end of the resistor is determined by the height of the water above it as given by $P = \rho gh$, where ρ is the density of water, g is the acceleration due to gravity, and h is the water height. Thus, the pressure difference across the resistor is $\Delta P = \rho g \Delta h$, where Δh is the height difference between the height of the reservoir and the droplet.

The droplet evaporation rate E can be found by analysis [55] of Fick's law, resulting in the relation

$$E \approx 4\pi r D (c_0 - c_\infty) \quad (3.3)$$

where r is the radius of the droplet, D is the diffusion coefficient of water vapor in air, and c_0 and c_∞ are the vapor density at the droplet surface and infinity, respectively. This evaporation rate can be combined with the previous equations to determine the height needed to maintain a droplet of a given radius r through

$$h \approx R_h \frac{4\pi D (c_0 - c_\infty)}{\rho g} r \quad (3.4)$$

which, for a droplet of radius $r = 250 \mu\text{m}$ and typical lab conditions (21 °C, 50% humidity), equates to a height of $h = 6.5 \text{ cm}$.

The relationship between height and droplet radius are strongly dependent upon the environmental conditions, particularly the temperature and humidity. Furthermore, the model described above represents a simple explanation of the system, particularly for determining the evaporation rate. In practice, other effects (such as airflow) contribute to evaporation but are not addressed in this explanation. Therefore, while it is very difficult to determine mathematically what the diameter of a stable droplet will be based on the height of the reservoir, through experimentation we determined that the water height needed to maintain a droplet at various temperature and humidity values remains in a range that we can address with our setup. For reasonable lab conditions, a droplet with $r = 250 \mu\text{m}$ can be maintained at water heights ranging from 2 cm to 20 cm.

3.2.4 Experimental Procedure

The experimental procedure is outlined in figure 3.3. The device before a droplet is formed is shown in figure 3.3(a). Figure 3.3(b) shows a droplet on the device head, with corner pinning on the top edge evident. A droplet is initially formed by applying a small amount of external pressure (less than 1 psi) to the water reservoir. After the droplet is formed, the external pressure is turned off, and a valve is opened to ensure the reservoir remains at atmospheric pressure for the remainder of the experiment. At this point, the flow rate of water to the droplet is entirely determined by the reservoir height.

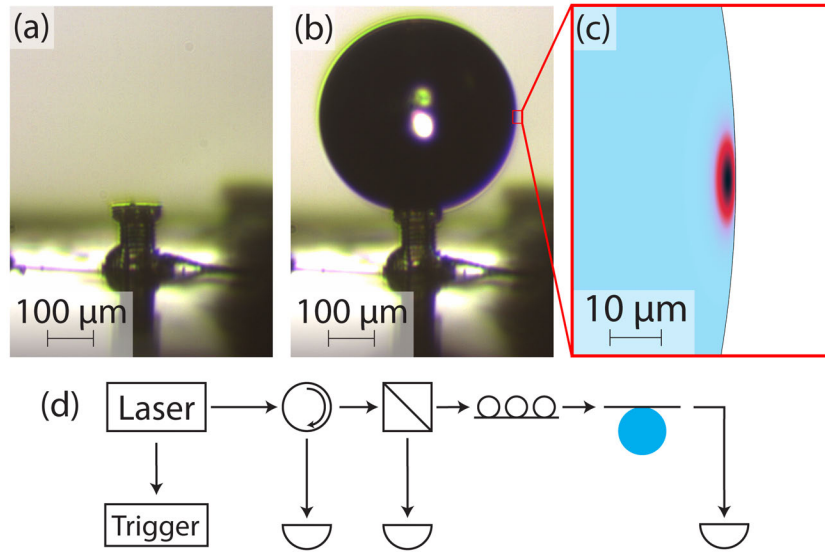


Figure 3.3: (a) The 3D printed device for supporting microdroplet resonators. (b) Water droplet supported by the 3D printed device. (c) Fundamental Z polarized mode of the droplet. Water is shown in light blue, and air is shown in white. (d) Visualization of the optical path. Light from a laser passes through a circulator, then a beamsplitter, then a polarization controller. The light is then coupled to the droplet via a tapered fiber.

In practice, it is often more intuitive to consider matching the flow rate into the droplet with the evaporation rate of the droplet rather than considering that the size of the droplet is determined by the reservoir height. The reservoir height is proportional to the flow rate, and the evaporation rate of a droplet of a given size is constant. If the flow rate is greater than the evaporation rate, the droplet grows, and if the flow rate is lower than the evaporation rate, the droplet shrinks. With this in mind, in our experiments we form a droplet and allow it to expand until it is near the desired size. We then adjust the height of the water reservoir to fine-tune the droplet size and find equilibrium: the point at which the droplet has the desired size and no longer grows or shrinks. In our experience, this fine-tuning is vital for determining the required reservoir height for a droplet of a given size.

This procedure may be aided by the naturally stabilizing action of droplet evaporation, since the droplet evaporation rate is proportional to the droplet size (see equation 3.3). If we assume the flow rate into the droplet is larger than the evaporation rate, the droplet will grow in size. However, as the droplet grows, the evaporation rate also increases. This continues until the evaporation rate matches the input flow rate, and the droplet stabilizes. The same effect occurs for a shrinking droplet. In this way, we can adjust the reservoir height until the droplet is as stable as possible at the desired size, and then small mismatches in the flow rate and evaporation rate of the droplet will naturally stabilize. However, as explained previously, the theoretical model does not account for all possible system dynamics. We have often seen in our experiments that droplets tend to exhibit some form of hysteresis in that growing

droplets tend to keep growing if left alone and shrinking droplets tend to continue shrinking if left alone. The most reliable method for forming a stable droplet is to actively tune the reservoir height until the droplet becomes stable.

This procedure leads to stable droplets. In our context, the droplet being stable means that its size is either constant or that changes to the size are gradual enough that optical coupling is still possible for an extended time. In our experiments, we are able to optically couple the droplet resonator to the tapered fiber for over a minute. As the coupling distance is less than 1 μm , the droplet size therefore changes at a rate less than 1 $\mu\text{m}/\text{min}$. In one experiment, the droplet size was measured and changed in diameter from 524 μm to 518 μm over the course of 15 min, giving $dr/dt = 3.3 \text{ nm/s}$. In comparison, a droplet placed on a similar head but without our microfluidic system changed in diameter from 867 μm to 559 μm over the course of 6 min and had completely evaporated 6 min after that. This results in $dr/dt = 431 \text{ nm/s}$.

Once the droplet is stable, the droplet is brought into close proximity with a tapered optical fiber. The fiber is tapered using a heat-and-pull rig similar to those used in [27, 40–42]. After it is tapered, the fiber is treated with Sigmacote (SL2, Millipore Sigma, Darmstadt, Germany), giving it a hydrophobic coat. This hydrophobic coat makes coupling to the fiber much easier. Without the coating, there is often an attractive force between the fiber and the droplet, causing them to touch when brought close together. Upon touching, the droplet deforms, eliminating resonance, and can leave residue on the fiber. The coated fibers are able to make slight contact with the droplets without destroying the resonance, and they prevent residue from being left on the fiber, allowing for repeated experiments on the same fiber. To the authors' knowledge, this is the first use of a hydrophobic coating on a tapered fiber to counteract attractive van der Waals forces, and it significantly reduces the difficulty of optical coupling.

The optical setup of our experiment is shown in figure 3.3(d). A wavelength-tunable laser (Sachertek PZ500, Sacher Lasertechnik, Marburg, Germany) is swept repeatedly near 930 nm, and a trigger signal is sent from the laser to an oscilloscope to correlate the wavelength with the measured optical signals. The light is sent through a circulator, with the return port being monitored for backscattering, then through a beamsplitter. The beamsplitter provides a reference signal that is used in postprocessing to normalize the variations in the power output of the laser due to the wavelength sweep. The signal beam continues to polarization paddles and finally to the tapered optical fiber, which is evanescently coupled to the water droplet. The transmission of the laser through the tapered fiber is monitored as the droplet is brought closer to the fiber until resonant features appear. Many resonant modes can be excited in this way, and figure 3.3(c) shows the simulated fundamental mode.

3.3 Results

Using the methods described above, we are able to create stable water microdroplets. The device geometry limits the size of droplets to diameters between 300 μm and 600 μm , as excessively small droplets do not exhibit a spherical shape and large droplets advance beyond the corner boundaries of the devices and collapse. In one experiment, we created stable droplets with diameters of 400 μm , 500 μm , and 600 μm . We measured the reservoir height for each and compared those to the mathematically expected heights. We found that, in practice, the measured heights were significantly larger than expected but that the change in reservoir height needed to create droplets of a different size was the same. That is, the reservoir height needed experimentally had a constant offset from the calculated value, as shown in Table 3.1. We believe this is due to a higher evaporation rate. This difference could be caused by air currents or other dynamics. It has been shown that the evaporation rate of sufficiently small droplets can be more complex than the treatment we provide here [64, 65].

Table 3.1: Experimental and calculated reservoir heights and the differences between them for given resonator sizes.

Droplet Diameter [μm]	Reservoir Height (Experimental) [mm]	Reservoir Height (Calculated) [mm]	Difference [mm]
400	147	40	107
500	155	50	105
600	165	60	105

We coupled light into the droplets as described previously. The resulting data exhibit resonant peaks with a high quality factor (Q). Two peaks are shown in figure 3.4, wherein the measured optical power is shown with a solid line and the fitted Lorentzian is shown with a dashed line. Prior to fitting, the data were normalized to remove the wavelength dependence of the rest of the optical system by dividing the throughput power by the reference signal and normalizing to the maximum power.

The peaks in these plots were fitted to a Lorentzian by using a rate equation model [59]. After fitting the peaks, we found their quality factor (Q) through linewidth analysis. The peaks shown in figure 3.4 were found to have $Q = 3.01 \times 10^7$ (part (a), shown in blue) and $Q = 6.25 \times 10^8$ (part (b), shown in red). Many other peaks were analyzed and similarly demonstrate Q values on the order of 10^7 – 10^8 .

3.4 Discussion

The quality factors reported in the previous section were exceptionally high and merit additional discussion. The overall Q of a microdroplet resonator can be expressed as a combination of contributing Q factors associated with various loss mechanisms. As such, we can express the

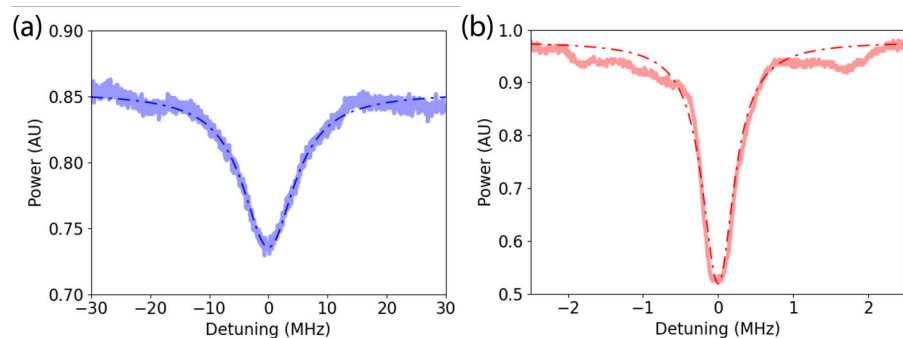


Figure 3.4: Resonant features of water microdroplets. The solid lines show the measured optical power, and the dashed lines show a fit to a Lorentzian. (a) A peak with $Q = 3.01 \times 10^7$. (b) A peak with $Q = 6.25 \times 10^8$.

overall Q as [57]

$$Q^{-1} = Q_{ab}^{-1} + Q_s^{-1} + Q_{rad}^{-1} \quad (3.5)$$

where Q_{ab} is the Q related to material absorption, Q_s is the Q related to surface scattering, and Q_{rad} is the Q related to radiative losses. Based on this relationship, the maximum value of Q is limited to the lowest of the contributions from loss mechanisms. In our devices, the curvature is relatively large and the surface is extremely smooth, so we expect both Q_{rad} and Q_s to be very large. As such, we expect Q_{ab} to limit the total Q . The material absorption Q can be calculated by $Q_{ab} = 2\pi n / \alpha \lambda$, where $n = 1.3278$ [66] is the refractive index of water, $\alpha = 0.20365 \text{ cm}^{-1}$ [66] is the absorption coefficient of water, and $\lambda = 930 \text{ nm}$ is the free-space wavelength of the light. The result is $Q_{ab} = 4.4 \times 10^5$, and we would expect this to be the maximum possible value for the Q of a water resonator. However, in our experiments, we measure Q values much higher than this.

We have explored several explanations for this discrepancy, including thermal bistability, systematic errors in data collection, and dynamic droplet sizes during measurement. Thermal bistability is caused when the intensity of the light in the droplet causes heating to occur, which causes a change in the refractive index of the liquid. This causes a shift in the resonant wavelength of the resonator and can be seen as a widening or narrowing of the resonant peak as the laser sweeps. Depending on the relative directions of the laser wavelength sweep and the resonance shift, the peak may appear narrower or broader than its natural linewidth. Since water has a negative thermo-optic coefficient (increasing temperature leads to decreasing refractive index), we would expect to see linewidth broadening while scanning toward shorter wavelengths and linewidth narrowing when scanning toward longer wavelengths [20]. We conducted experiments wherein the wavelength was swept from 930 nm to 931 nm and back, capturing both sweep directions. No significant change in Q was observed between the sweep directions, and, as such, we do not believe thermal bistability to be the cause of the higher-than-expected Q .

We considered instability in droplet size to be another likely reason for measuring a higher Q than expected. Though the droplets are very stable, subtle growth or shrinkage of the droplet has been observed. In particular, droplets that are growing slightly are commonly seen, as droplet growth aids with reducing the gap between the droplet and the tapered fiber, allowing for coupling. The effect of a growing droplet on the quality factor of the resonator is expected to be similar to that of thermal broadening and narrowing, as a changing droplet size also will result in a moving resonant wavelength. As such, we would expect to see a difference in the Q of resonances measured with a low-to-high wavelength sweep versus a high-to-low wavelength sweep. As stated above, no significant difference was observed for such sweeps.

Another possibility is that the resonant wavelength is changing so fast due to instability that the wavelength of the laser is effectively stationary in comparison. In this case, the direction of the laser sweep would be irrelevant. For this to be the case, the droplet's resonant wavelength (λ_0) would need to be changing at a rate such that the difference in the actual (Q_{act}) and measured (Q_{meas}) quality factors of the resonator and the sweep speed of the laser ($d\lambda_{las}/dt$) and the rate of change of the resonant frequency ($d\lambda_0/dt$) are the same, that is

$$\frac{d\lambda_0/dt}{d\lambda_{las}/dt} = \frac{Q_{meas}}{Q_{act}} \quad (3.6)$$

since a faster relative change in wavelength between λ_0 and λ_{las} results in a higher measured Q . For the blue peak shown in figure 3.4(a), the laser sweep speed was $d\lambda_{las}/dt = 1$ nm/s, and the measured Q was $Q_{meas} = 3.01 \times 10^7$. Using the absorption-limited Q as a maximum value for the actual Q , we get $Q_{act} = Q_{ab} = 4.4 \times 10^5$. Using these values with equation 3.6, we find $d\lambda_0/dt = 68$ nm/s. This represents a conservative estimate of $d\lambda_0/dt$, as either a higher measured Q (such as the red peak in figure 3.4(b)) or a lower Q_{act} (if we considered loss mechanisms other than absorption) would result in a higher $d\lambda_0/dt$.

Using $d\lambda_0/dt$, we can find the expected rate of change of the droplet radius dr/dt by taking the derivative of the equation $\lambda_0 = 2\pi rn/m$, resulting in

$$\frac{dr}{dt} = \frac{d\lambda_0}{dt} \frac{m}{2\pi n} \quad (3.7)$$

where r is the radius of the droplet, n is the refractive index of water, and m is the azimuthal mode number. Using $m = 2230$ (which corresponds to $r = 250.005$ μm at $\lambda_0 = 930$ nm), we calculate $dr/dt = 20.165$ $\mu\text{m/s}$. This is an unrealistically high rate for a droplet that appears to be stable. If the droplet were growing at this rate, the radius would double in 12.5 s, which was not observed in our experiments. As previously discussed, stable droplets have a radius rate of change of under 1 $\mu\text{m/min}$, and a typical droplet was measured to have $dr/dt = 3.3$ nm/s.

Finally, we investigated our data collection and analysis process to ensure we were accurately correlating our measurements to the laser

wavelength, fitting the resonant peaks, and calculating the Q . We found our process to be robust and our analysis to be accurate. In the course of our study, we performed experiments using different components (fiber, 3D printed device, and hydraulic resistor), and we see similarly high values in all cases. As such, though we do not fully understand the cause of these high Q values, we believe them to be accurate. These results merit further study and replication by future researchers, as the Q values we report are significantly higher than any previously reported quality factors for water resonators.

3.5 Conclusions

In conclusion, we have demonstrated a system that uses 3D printed microfluidic mounts to create stable water microdroplet resonators in ambient environments. The system we present overcomes the effect of droplet evaporation by supplying a constant flow into the droplet in stable equilibrium. The resulting resonators exhibit very high optical quality factors. These results may lead to future systems that integrate additional microfluidic technologies such as mixers and valves [32]. Integrating such microfluidic devices to the microresonator mount could allow for real-time manipulation of the droplet's contents for mixing and adding analytes or dyes on demand. The system we present here provides a basis for such future work and demonstrates a unique solution for the challenges inherent in using water microdroplet resonators.

Freezing of Clear Ice Microdroplets

The majority of this chapter is composed from a paper entitled “Freezing Optically Clear Microdroplets in a Laboratory Setting” presented at the 2023 Intermountain Engineering, Technology and Computing (IETC) conference [67]. I hereby confirm that the use of this article is compliant with all publishing agreements.

Additional work beyond the scope of the aforementioned paper will be presented at the end of this chapter.

4.1 Introduction

Freezing microdroplets has many geological, environmental, and biological applications and has received much attention from researchers. Researchers have investigated the properties of freezing microdroplets, such as the process of freezing microdroplets [33] and the effect of humidity on the freezing of droplets [34]. Further research not restricted to microdroplets has investigated the optical properties of ice [35] and its nonlinear optical properties, in particular at the surface of ice [36, 37]. Nonlinear optics have also been used to investigate the freezing process [38].

However, much of this research focuses on structures such as plane-shave ice blocks [68], and curved structures such as ice microdroplets have been mostly neglected in optical research, in part because an uncontrolled freezing process generally makes ice that is not transparent and has a high optical loss. In this paper, we propose a method of freezing optically clear water droplets. These ice droplets provide new opportunities in optical research, such as creating optical resonators, optically examining the freezing process, and examining substances frozen within the droplets.

4.2 Methods

Many techniques exist for freezing microdroplets; however, many of these techniques, such as dropping water droplets to freeze in the air or placing droplets in a freezer, do not allow easy optical access. As such we custom build a setup for that purpose. Figure 4.1 shows our optically clear ice-freezing setup. The droplets are supported by a 3D printed hydrophobic surface, which allows the formation of small, nearly spherical droplets. The droplets are formed by pushing water through a channel that connects the base of the devices to the tops. This results in

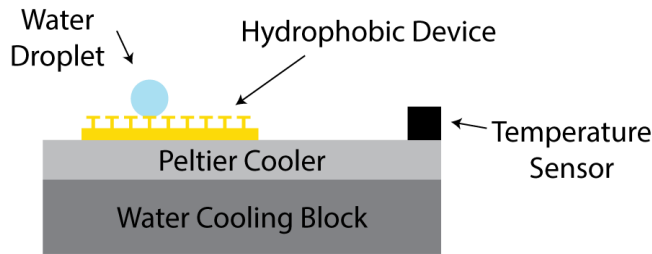


Figure 4.1: Setup for freezing the microdroplets. Droplets are formed on a 3D printed hydrophobic device and cooled using a Peltier cooler. Excess heat from the Peltier cooler is removed using a water cooling block, and the temperature of the Peltier is monitored using a temperature sensor.

droplets that can be less than 500 μm in diameter and have an apparent contact angle of over 120° . To freeze the droplet, the hydrophobic device is placed on a Peltier cooler. A water cooling block removes excess heat from the Peltier cooler. A temperature sensor is placed on the Peltier cooler surface to determine the temperature of the Peltier cooler, and a feedback loop is used to adjust the voltage applied to the Peltier cooler to achieve the desired freezing temperature. The voltage is controlled using an Arduino microcontroller with pulse-width modulation (PWM). The system is capable of maintaining a temperature as low as -20°C with an accuracy of $\pm 0.5^\circ\text{C}$. The microcontroller allows a large degree of control over the freezing rate. This setup allows the droplet to be cooled exclusively from below, which is important for pushing dissolved gases vertically upward during freezing.

4.2.1 Freezing Rate

Cooling the droplet exclusively from below and having control over the freezing rate is necessary because freezing optically clear ice relies on freezing pure water slowly and in one direction.

Disclarity in ice is caused by bubbles and other impurities being trapped in the ice lattice, giving ice a cloudy appearance. Because gasses are less soluble in ice than in water, as water freezes, the dissolved gasses in the water are concentrated into a reduced volume of water. The dissolved gasses become concentrated locally at the interface between the water and ice. When the dissolved gasses reach a high enough concentration, supersaturation occurs, where the water holds more gas than it can sustain in a dissolved state. Reaching supersaturation causes bubbles to nucleate at the phase boundary and on insoluble particles in the water. If the freezing rate of the water is sufficiently slow, the dissolved gasses can diffuse into the unfrozen water, preventing supersaturation at the water-ice interface and eliminating bubble nucleation. However, if water freezes too quickly, the bubbles formed by supersaturation become stuck in the ice lattice, causing disclarity [69]. Freezing at a linear rate less than $3\ \mu\text{m/s}$ [69] eliminates bubble nucleation at the phase boundary, resulting in transparent ice. Using distilled water reduces bubble nucleation sites,

which further reduces bubbles trapped in the ice lattice.

4.2.2 Freezing Direction

Another factor in ice clarity is the direction of freezing. When a microdroplet is cooled from all sides, it starts freezing on the outside, and the ice plane moves inward, forcing dissolved gases to supersaturate in the center of the droplet and form bubbles. When cold temperature is applied to only one side of the droplet, ice freezes directionally. In this way, dissolved gasses are pushed to one side of the droplet (in our case, the top), where they either can escape into the air or create bubbles in a region unimportant to our experiments.

4.2.3 Freezing Process

An additional effect of our freezing process is the reduction of ice nucleation sites, resulting in supercooling. Supercooling occurs when the temperature of a liquid is lower than its freezing point but the liquid is not solidified. In water, supercooling can occur if there are no ice nucleation sites. Typical ice nucleation sites include impurities in the water and the contact boundary of the water droplet and the surface it rests on. When ice nucleation occurs in a supercooled droplet, a near-instantaneous porous structure of ice, known as dendritic ice, freezes throughout the droplet in a process called recalescence. This process releases energy by forming the crystalline structure and brings the temperature back up to the freezing point. After recalescence, the remaining water in the droplet freezes into solid ice at a slower rate.

Figure 4.2 shows the process of a droplet freezing. Figure 4.2(a) shows a liquid droplet before freezing. Before freezing, the droplet is in a supercooled state until ice nucleation occurs. Figure 4.2(b) shows the same droplet after ice nucleation and recalescence. Ice nucleation in our droplets is often facilitated by the growth of ice crystals around the droplet. When a crystal contacts the droplet, it acts as an ice nucleation site and dendritic ice forms. The dendritic ice is recognizable by the textured appearance of the droplet. As the ice fully freezes, the texture disappears. Figure 4.2(c) shows the droplet as the droplet fully freezes in the main phase of freezing. When the droplet freezes at a slow rate, the directional freezing can be seen as a rising ice plane in the droplet. The rising ice plane can be seen in real time and is highlighted by arrows in figure 4.2(c). Controlling the freezing characteristics of this phase is essential for creating a clear ice droplet. The droplet must freeze unidirectionally and at a slow rate to ensure dissolved air is not trapped in the ice. At the end of the freezing process, the dissolved gasses become supersaturated and bubbles rapidly form and leave the droplet, sometimes giving the top of the droplet a rough appearance as in figure 4.2(d), which shows an ice droplet after the freezing process is complete. As the freezing finishes, the droplets form a cusp shape at the top as a result of water expanding as it freezes. Experimentally, we use the

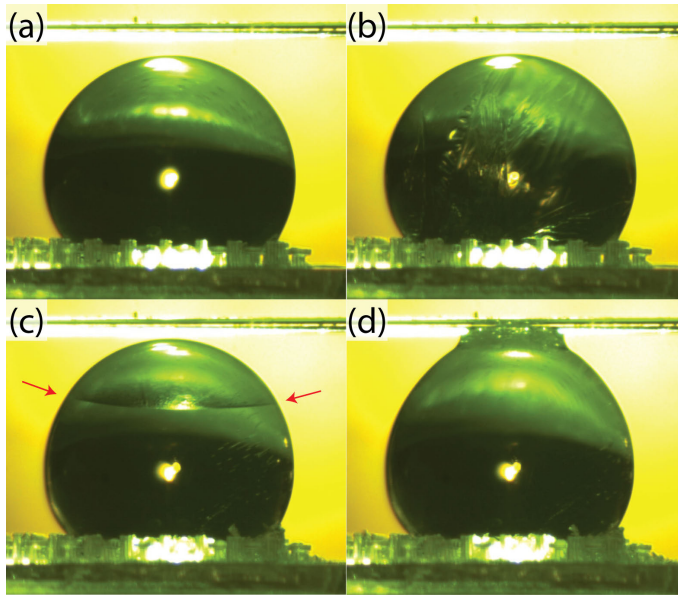


Figure 4.2: In the freezing process, an optical fiber (width 125 μm) is added to readily compare the size of the droplet during the transition from water to ice. (a) Unfrozen droplet. (b) Recalescence phase. Water has a blurred appearance due to porous (dendritic) ice formation. (c) Main freezing phase. The ice plane (the line that distorts the reflection as indicated by the red arrows) ascends vertically, slowly enough for bubbles and dissolved gases to diffuse. (d) Fully frozen clear droplet, forming a cusp shape unmarred by bubbles. The top is rough due to escaping bubbles at the end of the freezing process.

formation of a cusp at the top of the droplet to indicate a completed freezing process.

Figure 4.3 shows a typical droplet before and after freezing. Before freezing, the water droplet is optically clear, as in figure 4.3(a). The optical clarity of the frozen droplets can be determined by comparing them to the unfrozen droplets. The frozen droplet shown in figure 4.3(b) exhibits a high level of clarity, appearing nearly identical to the water droplet in figure 4.3(a) apart from the formation of a cusp due to freezing. However, the droplet in figure 4.3(c) was frozen too quickly, and as a result air bubbles were trapped in the ice lattice and are clearly visible in this figure. In an ideal droplet, after freezing the only transformation is the shape of the droplet, with no change in clarity.

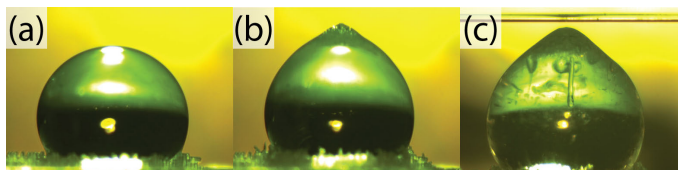


Figure 4.3: Optically clear ice droplet. (a) Water droplet before freezing. (b) Ice droplet frozen using our method to maintain clarity. (c) Droplet frozen too quickly, resulting in the formation of bubbles.

4.2.4 Humidity

After this freezing process, the microdroplet is optically clear; however, the frozen droplet becomes sensitive to the humidity of its environment. High ambient humidity causes the growth of ice crystals on the outside of the droplets, impacting their shape and clarity. Low ambient humidity results in sublimation, which distorts the shape of and shrinks the ice droplets.

To mitigate this problem, we built a humidity-controlled box. The box is airtight and encapsulates all relevant equipment, which ensures the ice droplets are still easily accessible, and all additional equipment is connected by wires and tubes through sealed ports. The humidity is controlled using silica gel beads, allowing the humidity to be set to any value below the ambient humidity of the lab, which is typically 60%. (All relative humidities are at 23 °C unless otherwise specified.)

The effects of humidity on the sublimation rate can be determined mathematically. The rate of sublimation is equal to the rate of evaporation from a small droplet because they are both defined by the diffusion of the water vapor away from the droplet [70]. As such, we can use a derivation of Fick's first law for the evaporation rate of a spherical droplet [71] to approximate the sublimation rate from the frozen droplet. The rate of evaporation from a spherical is [72]

$$\frac{dm}{dt} \approx 4\pi r D (c_0 - c_\infty) \quad (4.1)$$

where $\frac{dm}{dt}$ is the rate of loss of mass of the droplet (due to either evaporation or sublimation), D is the diffusion coefficient of the vapor, r is the radius of the droplet, and c_0 and c_∞ are the concentration of the vapor, or absolute humidity, at the interface and at infinity, respectively.

Analysis of equation 4.1 shows that for a droplet of a given radius, the sublimation rate is entirely determined by the water vapor concentration or absolute humidity. Absolute humidity is defined as the mass of water vapor per unit volume of air. In equation 4.1, c_0 is equal to the saturation concentration of water in the air, which is temperature dependent. To eliminate sublimation, c_∞ , the absolute humidity of the environment, must be equal to c_0 . To ensure this occurs, we regulate the humidity of the environment around the droplet.

Humidity is generally measured in terms of relative humidity (RH), where $RH = v_p/v_s$, with v_p being the partial pressure of the water vapor and v_s being the saturation vapor pressure for water in the air. As the saturation pressure is temperature dependent, the RH will be different in the vicinity of a frozen droplet as compared to the surrounding environment, even though the concentration of the water vapor will be the same. To eliminate sublimation, the RH at the droplet must be 100%, which is an equivalent concentration of water as a lower RH at room temperature. Figure 4.4(a) shows the calculated sublimation rate of a droplet of radius 250 μm for different temperatures. Several traces are shown, which correspond to different RH values of the environment. The

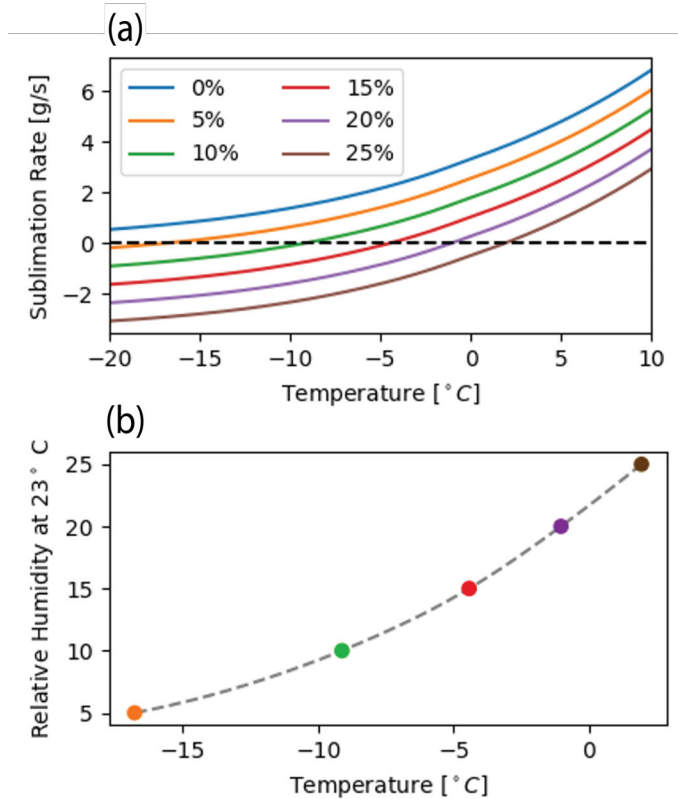


Figure 4.4: (a) Calculation of the sublimation rate at different temperatures. When the sublimation rate is 0, the droplet will be stable. (b) Temperatures and humidities corresponding to a sublimation rate of 0. The marked points are taken from the data in plot (a), with the curve being a quadratic interpolation of those points.

RH of the environment is used since our humidity sensor is set a small distance away from the droplet to avoid interference, so relative humidity is determined at 23 °C. These curves show that for a given ambient humidity, the droplet will experience sublimation at a rate determined by the temperature. Negative sublimation rates indicate an excess of water vapor at the droplet, which will result in crystal growth, though the values on the graph may not exactly reflect crystal growth rates. For stable droplets, a sublimation rate of 0 is desired. The 0 sublimation rate values are plotted in figure 4.4(b), which shows the temperatures and humidities corresponding to a sublimation rate of 0 for a 250 μm radius droplet. The points on this plot are the zero crossings of figure 4.4(a), and the curve is a quadratic interpolation of the points. This plot can be used to determine the proper humidity to prevent sublimation for a given droplet temperature, which in turn can be determined experimentally as the temperature that gives rise to a sufficiently slow freezing rate of the droplet.

Figure 4.5 shows the experimental verification of our calculations. In the experiment, droplets were frozen and observed after 5 minutes in environments with differing levels of humidity. The droplets were

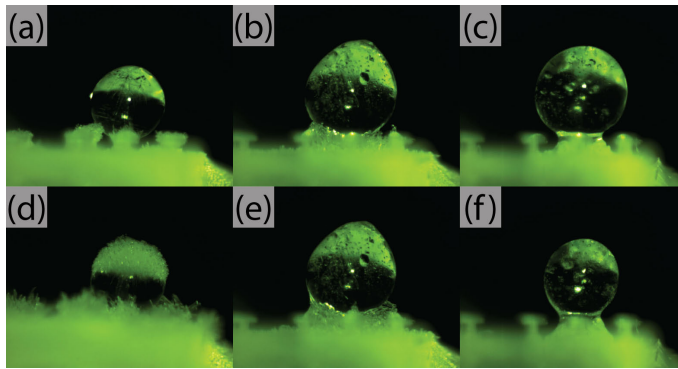


Figure 4.5: Effect of humidity on droplet stability. The top row (a-c) shows newly frozen droplets, and the bottom row (d-f) shows those same droplets after 5 minutes under different humidity conditions. (a) Droplet frozen at a high humidity (30% RH). (b) Droplet frozen at an ideal humidity (12% RH). (c) Droplet frozen at low humidity (0% RH). (d) Growth of ice crystals on the droplet (a) after remaining in 30% RH for 5 minutes. (e) Droplet (b) after remaining in 12% humidity for 5 minutes. This is ideal and shows the droplet is stable. (f) Droplet (c) after remaining in 0% RH. The droplet shape is altered due to sublimation.

frozen at -6°C . Figure 4.5(a–c) shows the droplets immediately after freezing, and figure 4.5(d–f) shows the same droplets 5 minutes later. In figure 4.5(a) and (d), we see a droplet in a high-humidity environment, and crystal growth is evident, resulting in a loss of clarity. In figure 4.5(b) and (e), we see a humidity corresponding to a 0 rate of sublimation, and the droplet remains stable. In figure 4.5(c) and (f), the droplet is exposed to a low-humidity environment, and the droplet sublimates, resulting in a loss of mass and distortion of shape. We note that bubbles are present in the ice droplets due to freezing too quickly in this experiment.

As humidity drops we need to freeze at lower temperatures because the freezing point of water is depressed [34]. This phenomenon makes freezing clear droplets difficult because the freezing temperature also relates to the freezing rate. Future work will address this challenge to demonstrate a droplet that is free of both bubbles and ice crystal growth.

4.3 Conclusion

In conclusion, we present a method of creating optically clear ice droplets in a laboratory setting. When microdroplets consisting of distilled water are frozen unidirectionally at a speed of less than $3\ \mu\text{m/s}$ in an environment with the temperature and humidity defined by the line in figure 4.4(b), they freeze and remain optically clear. This method allows for consistency in making optically clear ice microdroplets in uninsulated spaces allowing for access for experimentation, such as attempting optical coupling. In our future work, we hope to explore the use of these microdroplets as optical resonators.

4.4 Additional Work

There is a challenge in creating clear ice droplets at low humidities. The main difficulty is the reduction of ice nucleation sites. Ice nucleation is necessary to establish the crystal structure of the ice. Because we use deionized water, there are no impurities in the water to facilitate nucleation, and we have experimentally observed that the 3D printed surface of our devices do not easily facilitate nucleation. In most of our experiments, ice nucleation was facilitated by frost growth. An ice crystal growing near the droplet would make contact with the droplet, seeding the droplet and starting recalescence. Figure 4.6 shows this process. In figure 4.6(a), the crystal growth near the droplet can be seen, and in figure 4.6(b), the crystal touches the droplet and the droplet takes on a textured appearance typical of dendritic ice.

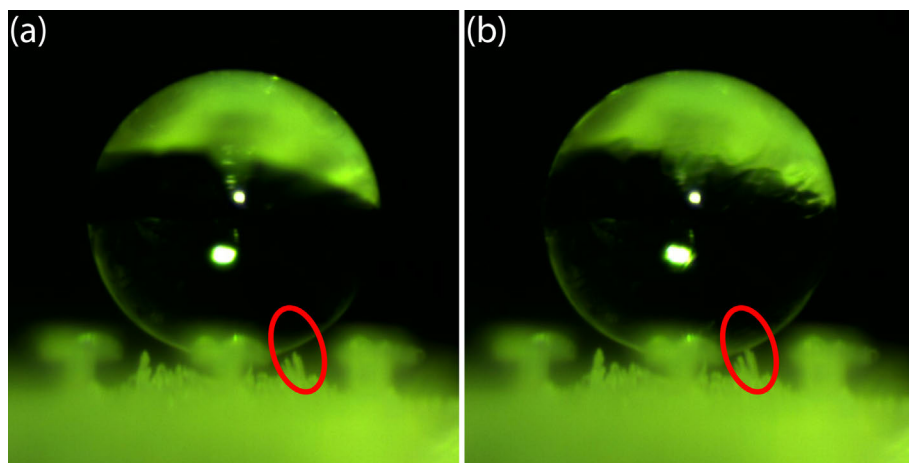


Figure 4.6: Seeding from an ice crystal. a) A supercooled water droplet just before seeding. The crystal about to contact the water surface is circled in red. b) The droplet just after seeding. The circled crystal has now touched the droplet, and the texture typical of dendritic ice can be seen on the top half of the droplet.

This method for seeding ice was very convenient and consistent; however, the same crystal growth that seeded the droplets would quickly mar the surface of the droplet. To prevent this, the droplets are frozen in a lower humidity environment, but this in turn prevents the growth of these seeding crystals. As expected, without a seed it became impossible to start the freezing process at the temperatures needed to ensure a slow freeze (about -2 °C). To overcome this, we developed a method that seeds the ice and allows for freezing at relatively high temperatures in low humidities. We call this process channel seeding.

Channel seeding works by freezing the water channel with a rapid freeze to seed the desired slow freeze. Channel seeding has four steps: freeze a sacrificial droplet, remove the sacrificial droplet, create a new water droplet, and freeze the new droplet. Figure 4.7 shows the steps of the process. The first step is to freeze a sacrificial droplet (shown in figure 4.7(a)). The water droplet to be frozen will be created as normal by pushing water through the channel onto the mount while

at a temperature just above freezing ($3\text{ }^{\circ}\text{C}$). The droplet is then frozen by reducing the temperature as low as necessary to start the freezing, commonly between $-5\text{ }^{\circ}\text{C}$ and $-10\text{ }^{\circ}\text{C}$. Once frozen, the sacrificial droplet is removed (shown in figure 4.7(b)). This is done by setting the device temperature to $3\text{ }^{\circ}\text{C}$ and blowing room temperature nitrogen directly onto the droplet. This will melt the droplet and evaporate all water so a new droplet can be formed on the mount. It is important the the droplet be removed as quickly as possible to ensure the channel remains at least partially frozen. At this point, the water pressure in the reservoir is increased to create a new droplet (shown in figure 4.7(c)). The temperature is left at $3\text{ }^{\circ}\text{C}$ until a new drop forms, at which point it is immediately lowered to the slow freeze temperature of $-2\text{ }^{\circ}\text{C}$. The droplet may take some time to form (up to a few minutes), since the channel should be frozen. Only when the channel begins to thaw will the droplet form. With the droplet formed and the temperature set to $-2\text{ }^{\circ}\text{C}$, the droplet will freeze slowly from the bottom (shown in figure 4.7(d)). Fine-tuning of the temperatures may be needed to ensure success.

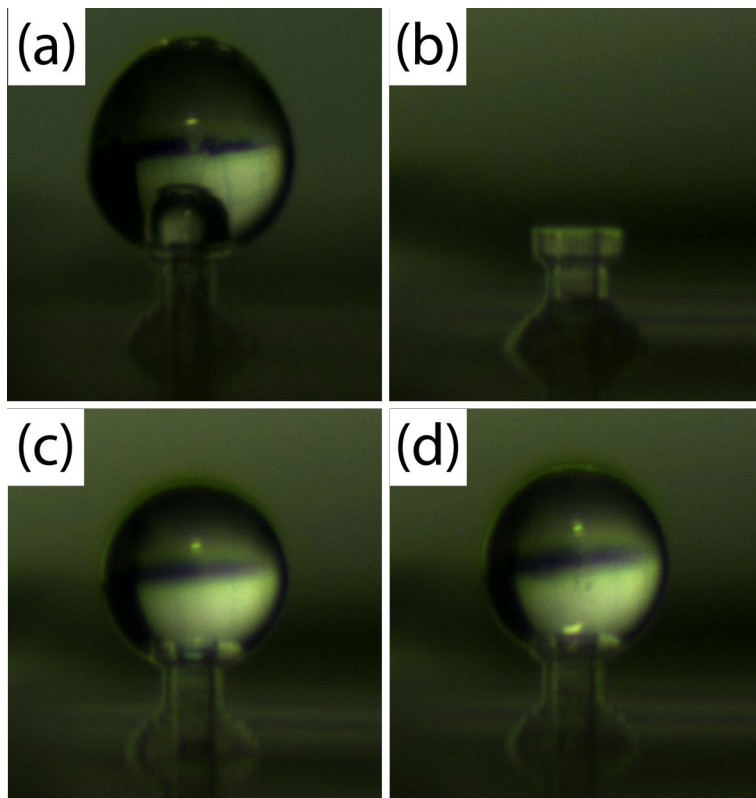


Figure 4.7: Steps of the channel seeding method. (a) The sacrificial droplet frozen at a low temperature. (b) The mount after the sacrificial droplet is removed. (c) A new droplet formed at a temperature just above freezing. (d) The new droplet after being frozen at a temperature just below freezing.

The channel seeding method was tested without the use of the environmental control box at a time when the lab relative humidity was naturally low. Later attempts to use the channel seeding method

within the environmental control box were less successful. The difficulty arose in melting the rapidly frozen droplet using the nitrogen blower because of the limited reach of the box gloves. This should be possible to overcome by modifying the gloves or the experimental setup to ensure everything can be easily reached. An additional difficulty arose in the optical coupling. It is desirable to couple to the droplet as soon after freezing as possible to mitigate any possible effects of crystal growth or sublimation, even when operating in a controlled environment. To do this, the tapered fiber should be fabricated and placed in the experimental setup. This presents a risk since it is possible to break the taper when blowing nitrogen to melt the sacrificial droplet. As with the difficulty of reaching with the gloves, this difficulty should be relatively easy to overcome for a future researcher.

Environmental Control Box

This chapter is composed from a paper entitled “OSCBox: An Open Source Extreme Humidity and Temperature Solution” which has been submitted for publication in the journal *HardwareX*.

Specifications Table

Table 5.1: Specifications table.

Hardware name	OSCBox: An Open Source Extreme Humidity and Temperature Solution
Subject area	<ul style="list-style-type: none"> • Chemistry and biochemistry • Photonics • Electronics
Hardware type	<ul style="list-style-type: none"> • Measuring physical properties and in-lab sensors • Controlling environment for experimentation
Closest commercial analog	Laboratory Glove Box
Open source license	CC BY 4.0
Cost of hardware	USD \$1000
Source file repository	https://data.mendeley.com/datasets/jrt4mkwggp/2

5.1 Hardware in Context

Many research areas require an environmentally controlled chamber for testing specimens. Specifically, a multitude of experiments require low temperatures and humidity, and much research has been done to resist ice and frost formation [73, 74]. In the field of electronics, low-humidity control is required while running tests at below-freezing temperatures and for observing variations in performance due to environmental variables [75, 76]. In the field of photonics and microfluidics, accurate low-humidity control in subzero temperature experiments allows researchers to develop new techniques for measuring environmental variables and methods for manipulating liquids [77–80]. Other fields

that require similar environmental control include food research [81, 82], biomedical research [83–85], environmental and wildlife research [86–88], and material science research [89–91].

To address this challenge, many open-source designs for temperature and humidity controlled environments have arisen [92–95]. However, these designs typically cannot accommodate experiments that require advanced equipment such as precision motion stages, microscopes, and probing tools. Furthermore, current open-source chambers are limited by the size and shape of the container they use as a base and the software they run locally on a microcontroller. They can also be difficult to use at extremely low humidity levels, as they are either unable to reach those levels or take a long time to do so. Thus, it is clear that while current open-source environment control chambers are functional for some users, they are insufficient for many researchers with complex and time-sensitive experiments that require humidity-controlled environments operating at temperatures below 0 °C.

In this paper, we present the Open-Source Control Box (OSCBox), a customizable humidity-controlled chamber with an integrated thermoelectric cooler (TEC) for controlling specimen temperatures. The chamber, unlike other open-source designs, is not built around a commercially purchased container. Instead, it is assembled using acrylic panels, making the shape and size adaptable. The box is designed with an open bottom so that it can be clamped to an optical breadboard. This allows all of the instrumentation required for the experiment to be secured to the table and remain inside the controlled environment, with electrical, optical, liquid, and gaseous connections leaving the box in an airtight fashion. The chamber (470 liters) can reduce its relative humidity from 30% to 0% in 15 minutes, with the TEC reaching its target temperature in under a minute. In addition to these features, the electronic controls for the box are accessible remotely using Pyrolab [96], a Python-based laboratory networking package. We provide software for a graphical user interface (GUI) that enables remote control of the box features.

5.2 Hardware Description

We present designs for a customizable humidity-controlled chamber and TEC, along with methods for incorporating complex equipment into the box. The chamber is constructed using 1/4" thick acrylic panels with 90° aluminum angle stock along the edges. Caulk is used to seal any gaps between the acrylic pieces and angle stock, making the entire chamber airtight. The chamber is not designed to be pressurized (>2 psi) or evacuated (>2 psiv).

The bottom of the chamber is completely open so that it can be mounted to an optics table using specialized clamps. The box has two large doors that are bolted onto the chamber for manual access. One has gloves mounted to it for working inside while maintaining a controlled environment. Foam window seal is lined around the perimeter of the

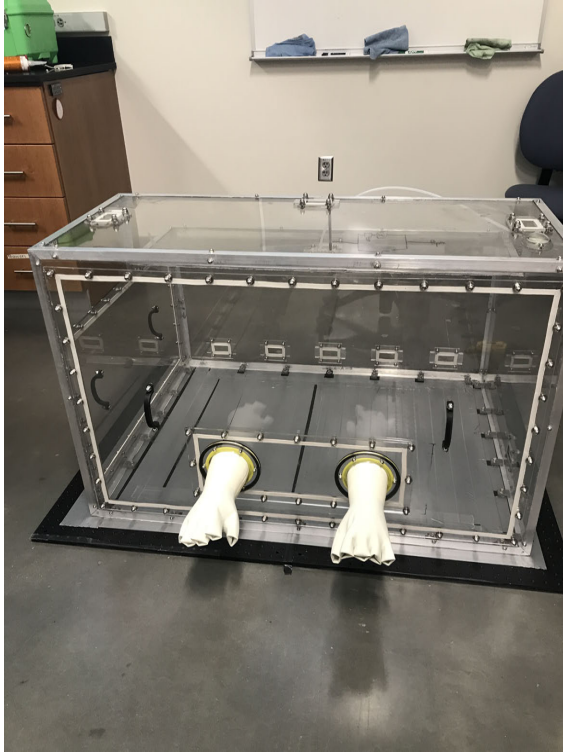


Figure 5.1: Constructed box clamped onto optical breadboard.

doors and the bottom of the box. When compressed, the window seal creates an airtight seal between these surfaces.

Several of the acrylic panels have small rectangular cutouts. These are used as universal ports for “wire doors” that manage the various airtight connections running into the box. The wire doors are designed to be modular and highly customizable, allowing the use of various diameters of cable and various connector types. This method maintains the integrity of the box environment while allowing wired connections to hardware inside the box.

The box humidity is controlled using a desiccator constructed of 1/4" acrylic, which is placed inside the box. The desiccator functions by cycling air through chemical desiccant and can maintain a relative humidity of 0% inside the box for several days.

The TEC consists of a Peltier tablet and a water-cooled aluminum block, capable of controlling the temperature of an experimental specimen to temperatures as low as -18°C .

OSCBox is designed to meet four criteria: it is inexpensive, it is airtight, it controls humidity and temperatures with a high-speed response, and it incorporates various electrical, optical, liquid, and gaseous connection options. Furthermore, OSCBox can easily be tailored to suit a variety of applications, such as differences in box geometry or internal hardware.

5.2.1 Summary

- Inexpensive solution for humidity and temperature control.
- Highly customizable shape and size, allowing for large experimental setups.
- Rapid response to changes in temperature and humidity set points.
- Capable of establishing wired connections to hardware inside the box.
- Compatible with Pyrolab, allowing remote access to hardware.

5.3 Design Files Summary

Table 5.2: Design files summary.

Design File Name	File Type	Open-Source License	Location of the File
bar_1	SolidWorks	CC BY 4.0	data.mendeley.com/datasets/jrt4mkwggp/2
bar_1_floor	SolidWorks	CC BY 4.0	data.mendeley.com/datasets/jrt4mkwggp/2
bar_2	SolidWorks	CC BY 4.0	data.mendeley.com/datasets/jrt4mkwggp/2
bar_3	SolidWorks	CC BY 4.0	data.mendeley.com/datasets/jrt4mkwggp/2
bar_4	SolidWorks	CC BY 4.0	data.mendeley.com/datasets/jrt4mkwggp/2
bar_5	SolidWorks	CC BY 4.0	data.mendeley.com/datasets/jrt4mkwggp/2
bar_6	SolidWorks	CC BY 4.0	data.mendeley.com/datasets/jrt4mkwggp/2
bar_7	SolidWorks	CC BY 4.0	data.mendeley.com/datasets/jrt4mkwggp/2
bar_8	SolidWorks	CC BY 4.0	data.mendeley.com/datasets/jrt4mkwggp/2
bar_9	SolidWorks	CC BY 4.0	data.mendeley.com/datasets/jrt4mkwggp/2
part_aa	SolidWorks	CC BY 4.0	data.mendeley.com/datasets/jrt4mkwggp/2
part_a_left	SolidWorks	CC BY 4.0	data.mendeley.com/datasets/jrt4mkwggp/2
part_a_right	SolidWorks	CC BY 4.0	data.mendeley.com/datasets/jrt4mkwggp/2
part_b	SolidWorks	CC BY 4.0	data.mendeley.com/datasets/jrt4mkwggp/2
part_c	SolidWorks	CC BY 4.0	data.mendeley.com/datasets/jrt4mkwggp/2
part_d	SolidWorks	CC BY 4.0	data.mendeley.com/datasets/jrt4mkwggp/2
part_e	SolidWorks	CC BY 4.0	data.mendeley.com/datasets/jrt4mkwggp/2

Table 5.2: Design files summary.

Design File Name	File Type	Open-Source License	Location of the File
part_f	SolidWorks	CC BY 4.0	data.mendeley.com/datasets/jrt4mkwggp/2
part_fa	SolidWorks	CC BY 4.0	data.mendeley.com/datasets/jrt4mkwggp/2
part_g	SolidWorks	CC BY 4.0	data.mendeley.com/datasets/jrt4mkwggp/2
part_ga	SolidWorks	CC BY 4.0	data.mendeley.com/datasets/jrt4mkwggp/2
door_handle	SolidWorks	CC BY 4.0	data.mendeley.com/datasets/jrt4mkwggp/2
glove_ring_1	SolidWorks	CC BY 4.0	data.mendeley.com/datasets/jrt4mkwggp/2
glove_ring_2	SolidWorks	CC BY 4.0	data.mendeley.com/datasets/jrt4mkwggp/2
valve_insert	SolidWorks	CC BY 4.0	data.mendeley.com/datasets/jrt4mkwggp/2
valve_screw	SolidWorks	CC BY 4.0	data.mendeley.com/datasets/jrt4mkwggp/2
wire_door	SolidWorks	CC BY 4.0	data.mendeley.com/datasets/jrt4mkwggp/2
wire_door_support	SolidWorks	CC BY 4.0	data.mendeley.com/datasets/jrt4mkwggp/2
desiccator_back	SolidWorks	CC BY 4.0	data.mendeley.com/datasets/jrt4mkwggp/2
desiccator_bottom	SolidWorks	CC BY 4.0	data.mendeley.com/datasets/jrt4mkwggp/2
desiccator_corner_piece	SolidWorks	CC BY 4.0	data.mendeley.com/datasets/jrt4mkwggp/2
sliding_door	SolidWorks	CC BY 4.0	data.mendeley.com/datasets/jrt4mkwggp/2
desiccator_ridge	SolidWorks	CC BY 4.0	data.mendeley.com/datasets/jrt4mkwggp/2
desiccator_side	SolidWorks	CC BY 4.0	data.mendeley.com/datasets/jrt4mkwggp/2
desiccator_top	SolidWorks	CC BY 4.0	data.mendeley.com/datasets/jrt4mkwggp/2
sliding_door_handle	SolidWorks	CC BY 4.0	data.mendeley.com/datasets/jrt4mkwggp/2
bar_rack_top	SolidWorks	CC BY 4.0	data.mendeley.com/datasets/jrt4mkwggp/2
bar_rack_bottom	SolidWorks	CC BY 4.0	data.mendeley.com/datasets/jrt4mkwggp/2
peltier_mount	SolidWorks	CC BY 4.0	data.mendeley.com/datasets/jrt4mkwggp/2

5.4 Bill of Materials Summary

Table 5.3: Bill of materials.

Designator	Component	Qty	Unit Cost	Total Cost	Source	Material
Clear Acrylic	1/4"x48"x96"	2	\$239.00	\$478.00	Home Depot	Plastic
Angle Stock	3/4"x48"x1/16"	11	\$7.00	\$77.00	Home Depot	Metal
6/32x7/16" Bolt	6/32x7/16" Bolt	129	\$0.07	\$9.03	McMaster-Carr	Metal
6/32x1 5/8" Bolt	6/32x1 5/8" Bolt	4	\$0.15	\$0.60	McMaster-Carr	Metal
6/32x3/4" Bolt	6/32x3/4" Bolt	24	\$0.07	\$1.66	McMaster-Carr	Metal
6/32 Nut	6/32 Acorn Nut	153	\$0.10	\$15.45	McMaster-Carr	Metal
1/4"-20 Bolt	1/4"-20x3/4" Bolt	164	\$0.21	\$35.23	McMaster-Carr	Metal
1/4"-20 Nut	1/4"-20 Acorn Nut	138	\$0.18	\$24.43	McMaster-Carr	Metal
1/4"-20 Washer	1/4"-20 Washer	164	\$0.03	\$5.69	McMaster-Carr	Metal
Caulk Tube	Gorilla Silicone	2	\$10.00	\$20.00	Amazon	Inorganic
Epoxy	Gorilla Epoxy	4	\$5.75	\$23.00	Amazon	Inorganic
Acrylic Glue	Weld-on 16	1	\$12.90	\$12.90	Amazon	Inorganic
Window Seal	3/8"x17' Seal	2	\$7.00	\$14.00	Amazon	Polymer
Black Acrylic	1/8"x12"x12"	1	\$10.00	\$10.00	Amazon	Plastic
Gloves	Latex Gloves	1	\$20.00	\$20.00	Amazon	Polymer
Raspberry Pi	RP4 1GB RAM	1	\$30.00	\$30.00	Adafruit	Electronic
Arduino Nano	Arduino Nano	1	\$12.00	\$12.00	Amazon	Electronic
Humidity Sensor	Si7021	1	\$10.00	\$10.00	Adafruit	Electronic
Temperature Sensor	TMP36 Sensor	1	\$2.00	\$2.00	Amazon	Electronic
Fan Relay	3.3V Relay	1	\$3.00	\$3.00	Amazon	Electronic
Desiccator Fan	120x120x30 mm	1	\$16.00	\$16.00	Amazon	Plastic
Power Supply 1	12V 1A Supply	1	\$7.00	\$7.00	Amazon	Electronic
Power Supply 2	5V 20A Supply	1	\$13.00	\$13.00	Amazon	Electronic
Power Supply 3	12V 5A Supply	1	\$13.00	\$13.00	Amazon	Electronic
Steel Sheet	1/32"x12"x18"	1	\$23.45	\$23.45	Amazon	Metal
Steel Mesh	0.9 mm Hole Mesh	1	\$16.80	\$16.80	Amazon	Metal

Table 5.3: Bill of materials.

Designator	Component	Qty	Unit Cost	Total Cost	Source	Material
Peltier	Peltier Tablet	1	\$10.00	\$10.00	Amazon	Inorganic
Water Pump	12V Water Pump	1	\$15.00	\$15.00	Amazon	Electronic
Thermal Grease	Thermal Grease	1	\$8.00	\$8.00	Amazon	Electronic
Cooling Block	Cooling Block	1	\$5.00	\$5.00	Amazon	Metal
Tubing	5/16"x1/16" Tubing	1	\$9.00	\$9.00	Amazon	Plastic
Tube Connector	5/16" Barbed	2	\$1.40	\$2.80	Amazon	Plastic
UV Resin	3D Printer Resin	1	\$10.00	\$10.00	Amazon	Resin
PLA Filament	3D Printer Filament	1	\$20.00	\$20.00	Amazon	Plastic
Desiccant	5 lb Silica Gel	1	\$30.00	\$30.00	Amazon	Inorganic

Note that there are a few small components that may not be included in this bill of materials. A complete bill of materials with purchasing links can be found in the associated Mendeley database.

5.5 Build Instructions

The construction of OSCBox is described below, with the build instructions divided into 7 sections: acrylic preparation, aluminum stock preparation, main assembly, 3D printing, wire doors and gloves, environmental control, and electronics. The acrylic and aluminum preparation steps must be performed before the main assembly can begin, but other steps may be performed in any order or concurrently. The box takes approximately 40 hours to construct. Note that this does not include time spent waiting for machining (3D printing, laser cutting, etc.) or time spent waiting on epoxy and caulk to dry. Figure 5.2 shows an exploded view of the box without any of the hardware (nuts, bolts, etc.). The shape of the box is nontraditional due to specific constraints in our laboratory setup but can be easily altered to make a box of any shape. This demonstrates the flexibility that our design permits. Note that the build instructions describe the use of less common tools (industrial laser cutter, press brake, etc.), but the box can be constructed using suitable alternatives.

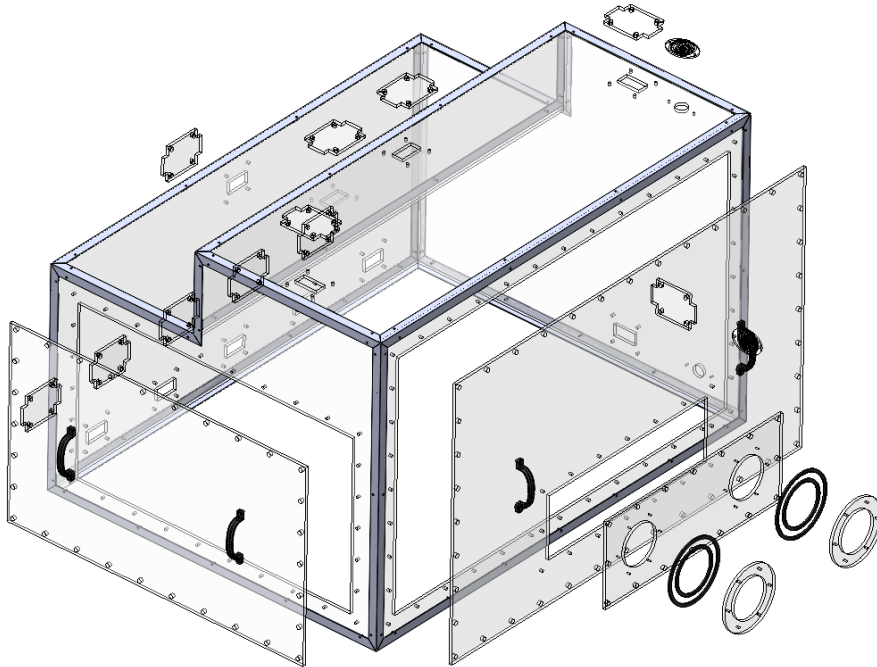


Figure 5.2: Exploded view of OSCBox.

5.5.1 Acrylic Preparation

This section covers the process to manufacture the box panes from the acrylic sheets. First, rough cut the acrylic sheets to ensure the pieces can be put in the laser cutter. To do this, use a permanent marker to draw a blueprint of all the pieces on the acrylic sheets slightly larger than the actual pieces so that after they are rough cut the laser cutter can trim the edges perfectly. We recommend using a jig saw to perform this rough cut, using water to cool the blade as necessary. Once the pieces have been rough cut, they can be laser cut using the DXF files found in the online Mendeley database. These files can easily be reproduced from SolidWorks if changes to the box design are desired.

The acrylic panels contain many holes, that can be classified as either access holes or screw holes. Access holes are typically larger and include holes for wires to enter the box, large holes used by people to work inside the box, and holes for valves and gloves. Access holes do not need any further preparation. On the other hand, screw holes will need to be tapped. Screw holes will be tapped for either 1/4-20 or 6/32 threads. We use 0.195" holes for tapping 1/4-20 threads and 0.11" for tapping 6/32 threads. All holes with these dimensions will be tapped, and holes of other sizes do not need to be tapped. Nearly all of the small, round holes in the design have one of these dimensions, other than holes on the edges of the doors, which are cut larger as through holes for the screws. Once the pieces have been laser cut, these holes can be tapped using an imperial tapping set, as shown in figures 5.3 and 5.4.

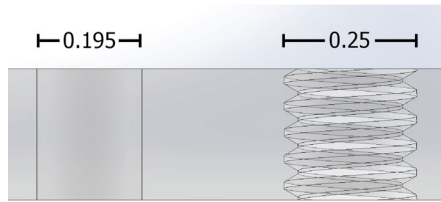


Figure 5.3: Untapped and tapped 1/4-20 holes in the acrylic.

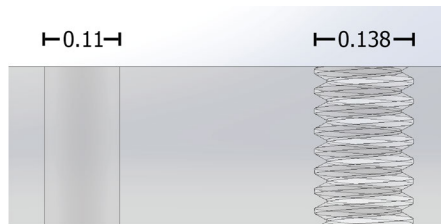


Figure 5.4: Untapped and tapped 6/32 holes in the acrylic.

The completed acrylic pieces are shown in figure 5.5 beside one another. We recommend making a rough assembly of the box using duct tape to hold the edges together to ensure the pieces fit together properly. (Use figure 5.6 as a reference for assembly.)



Figure 5.5: Main acrylic pieces after being laser cut and tapped.

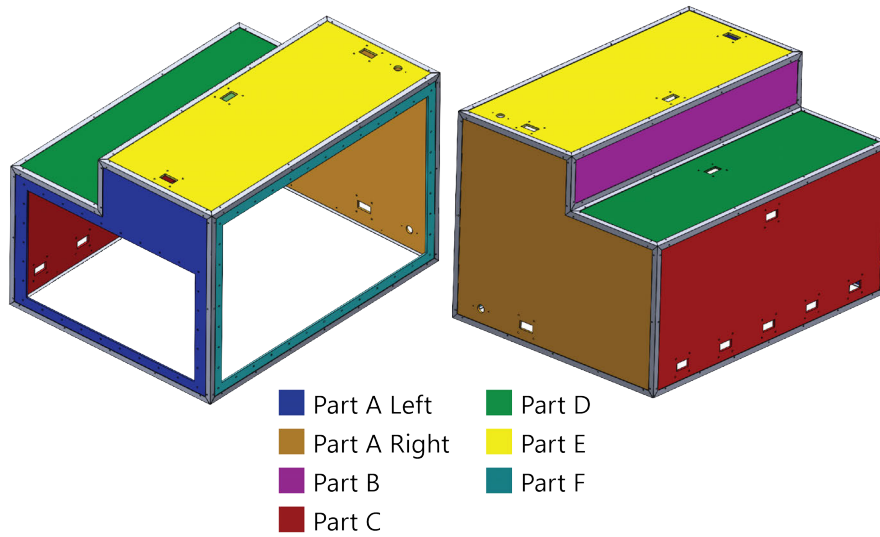


Figure 5.6: Colored image of the acrylic pieces corresponding to their file names.

5.5.2 Aluminum Stock Preparation

The aluminum angle stock is used for structural support and to ensure airtightness and should fit flush with one another and the acrylic pieces. Differing quantities of each bar are made, as shown in table 5.4.

Table 5.4: Aluminum stock list.

Component	Quantity
Bar 1	4
Bar 1 Floor	2
Bar 2	2
Bar 3	2
Bar 4	1
Bar 5	1
Bar 6	2
Bar 7	1
Bar 8	1
Bar 9	2

We recommend using a band saw to cut the aluminum stock. The dimensions of all of the bars can be found in the Mendeley database as drawings. A jig or other method can be used to create the 45° cuts. After this, drill holes using a drill press and a 0.25" drill bit. Proper alignment of holes in the aluminum edging and the acrylic panels can be ensured

by putting the two together and marking the aluminum through the already-cut acrylic holes. Figure 5.7 shows the placement of all the bars.

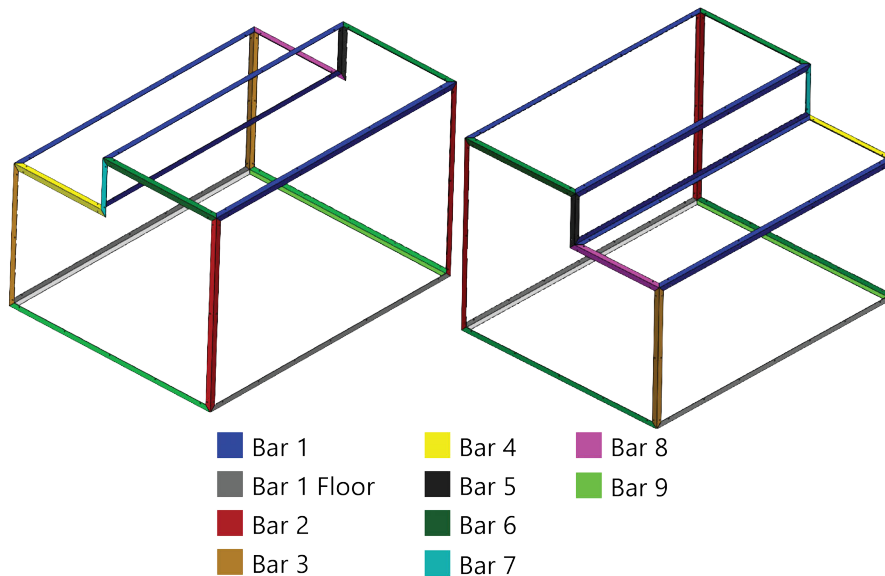


Figure 5.7: Colored image of the aluminum stock pieces corresponding to their file names.

Be aware that the ends of bars 4, 5, 7, and 8 are not like the others; they meet in a concave corner. The types of corner configurations are shown in figure 5.8.

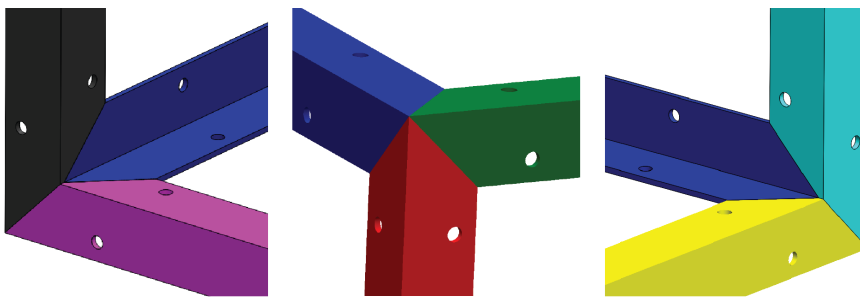


Figure 5.8: Three images of corners (color coded the same as figure 5.7). The left image shows the corner of bars 1, 5, and 8. The right image shows the corner of bars 1, 4, and 7. The center image shows how the rest of the corners look.

At this point, all of the necessary acrylic pieces should be cut and tapped along with the required aluminum angle stock being cut and holes drilled. Assemble the box to ensure that all the pieces fit together. It is possible that some of the edges of the aluminum will not fit together tightly or that some holes will not be aligned. Minor errors can be corrected using a file so that the entire box fits together snugly and is held together by the edge hardware. Because the edges will be sealed with caulk, small imperfections and gaps are acceptable. 6/32x7/16 bolts are threaded into the acrylic from the inside and stick through the holes drilled in the

aluminum edging. 6/32 acorn nuts are attached on the outside. Figures 5.9 and 5.10 show what the box should look like upon a preliminary build. (See figure 5.12 to better understand how the edges will be assembled.)



Figure 5.9: Preliminary construction of the box to ensure the pieces fit together properly.

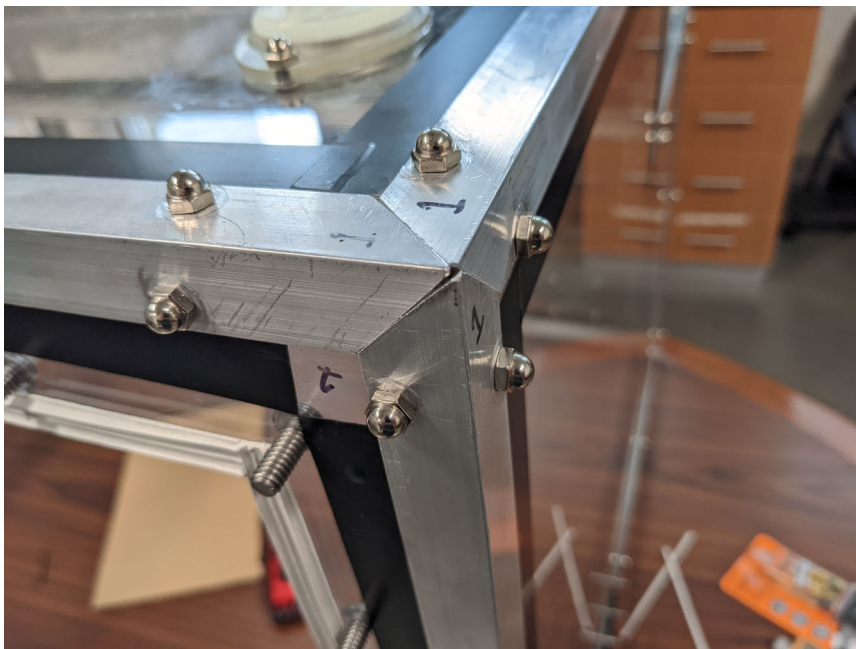


Figure 5.10: Close-up picture of an assembled corner.

5.5.3 Main Assembly

With the acrylic and aluminum pieces prepared, the box is ready for assembly. Throughout this section, refer back to figures 5.6 and 5.7 for how the box should be assembled. In order to assemble the acrylic and aluminum pieces to be airtight, we employ two methods. First, use epoxy on all the bolts so that no air can come through the threads, and second, seal the acrylic and aluminum with caulk. In order to minimize the time required for the main assembly, all of the 1/4-20 bolts and half of the 6/32 should be epoxied into their holes prior to the assembly. This is done by covering the threads in epoxy and then screwing them into the acrylic. The acrylic pieces with bolts epoxied are shown in figure 5.11. Roughly half of the 6/32 bolts can be epoxied before final assembly; however, if all the bolts are epoxied in place before the main assembly, it would be impossible to put the aluminum edging on. To determine which bolts can be epoxied, after performing a rough assembly, remove screws along a single side of an aluminum edge and ensure the bar can be removed and replaced without removing the remaining screws. Repeat for all aluminum edges.

We also use clear silicone caulk between the acrylic and the aluminum to ensure an airtight seal between the acrylic pieces. The assembly should ideally be completed in one sitting so that the caulk on all the corners can combine together fluidly. We also recommend using tape to mask the acrylic along the edges of the aluminum so any extra caulk can be easily removed.



Figure 5.11: Acrylic pieces after epoxying the 1/4-20 screws and half of the 6/32 screws.

When the parts are all ready to be assembled, ensure that you take the proper safety measures for working with the caulk by wearing gloves and safety glasses. Begin with the box assembled. Each bar will be removed and then reattached one at a time. Having the entire box assembled ensures that the pieces maintain their alignment and do not shift during the process. We recommend the following steps be performed by two or more workers. The procedure for attaching an aluminum edge piece to the acrylic is a six-step process, which is shown graphically in figure 5.12. First, remove the acorn nuts from one aluminum piece and remove it from the box. To do this, you will need to unscrew half of the 6/32 screws (the ones that are not epoxied yet) in order to remove the aluminum edging. Second, apply three beads of caulk to the edge with one exactly on the edge and one on either side of it. Put extra caulk on the corners to ensure it fills all of the gaps. Third, replace the bar and apply pressure. Caulk will likely spill from the sides and holes, but this will be cleaned up later. Maintain pressure on the bar while completing step four. Fourth, apply epoxy to the thread of the 6/32 bolts that were removed in step 2 and then screw them back in. Fifth, clean the threads of the 6/32 bolts with a paper towel because there will likely be caulk on the bolts after pushing them through the aluminum. Sixth, reattach the acorn nuts onto the protruding screws.

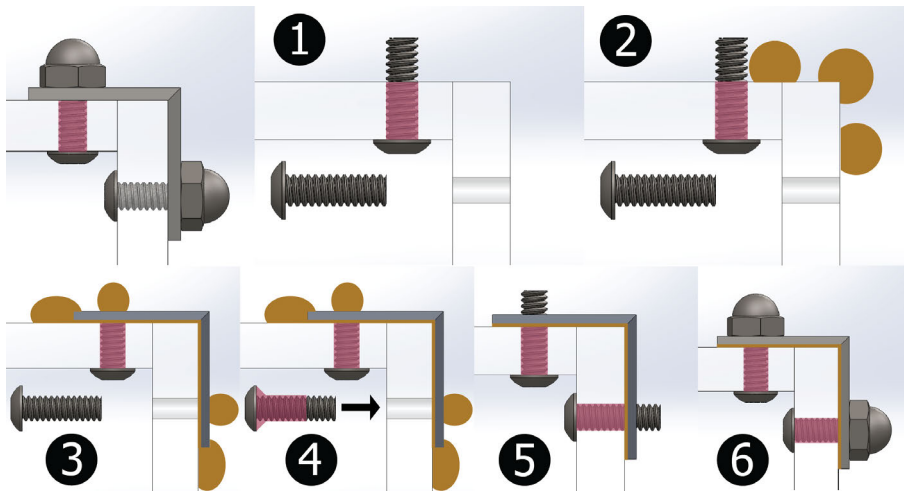


Figure 5.12: Instructions for applying caulk and epoxy to edges. The top left panel shows the screws before the main assembly, and the others show the steps of the main assembly. Caulk is shown in orange and epoxy is shown in translucent red.

Repeat these steps for all the edges of the box. The order in which the edging is attached is not important as long as each piece can be removed without removing another one. If this is not the case, care must be taken to ensure that the free-moving pieces are attached last. The main assembly is a long process, so ensure adequate time is allocated. In our case, it took four workers approximately five hours to complete. Once the main assembly is complete, leave the box at rest to allow the caulk to fully cure, following the manufacturer's instructions. During

this time, clean up any caulk or epoxy streaks on the acrylic or move on to the following sections, which can largely be completed without the box.

The final step of the main assembly is to prepare the seal for the doors and base of the box. For this, we use a common window seal, which is a strip of rubbery foam. We line the perimeters of each door (main and wire doors) with this sealant. The seal will be compressed using the 1/4-20 screws and nuts nearby to create a tight seal (figure 5.13). We also double-line the bottom aluminum with the window seal by placing two strips of sealant together lengthwise. This seal will be compressed using the 3D printed box clamps that screw into an optical breadboard.

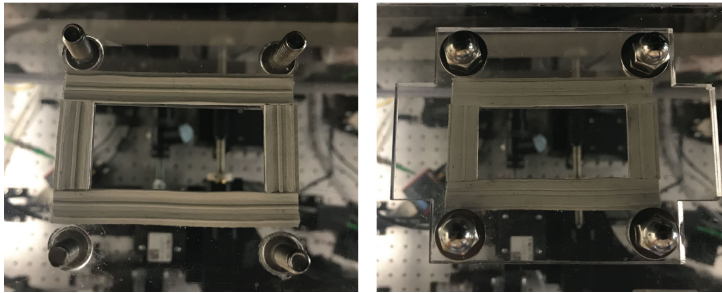


Figure 5.13: The window seal applied to the perimeter of a door and subsequently compressed for a tight seal.

5.5.4 3D Printing

We constructed the 3D printed parts using a resin printer for any pieces that needed to be airtight and a Fused Deposition Modeling (FDM) printer for all the other pieces. While there are different ways to make FDM prints airtight, access to a resin printer is recommended for ease of use. Any type of filament can be used, but we recommend using PLA to make FDM printing simpler. Please note that the required print settings will vary based on the 3D printer and material that is used. Adjust the print settings until you get satisfactory parts.

We printed the handles, clamps, and desiccator fastenings using an FDM printer. These parts are not difficult to print and require little support material. The clamps endure significant force, so we recommend using a high infill when printing them. The desiccator corners are very small and should be solid; thus, we recommend using an infill of 100%. The handles do not endure significant forces, so their infill is discretionary. The base for the TEC is also 3D printed using an FDM printer. Each print can be strengthened by increasing the layer height and the wall thickness with the added cost of a longer print time and higher material usage.

The box also includes two 3D printed valves (shown in figure 5.14), which enable venting the box for various experiments. These valves are printed using a resin printer and must be airtight. The valve consists of two pieces: the valve insert, and the valve screw. The valve insert is attached to the box using two 6/32 screws. These screws should already

have been epoxied in place during the main assembly. The face between the valve and the acrylic is sealed with epoxy or caulk, and then the 6/32 acorn nuts are attached. The valve insert contains a groove to hold a 1 1/2" gasket. The valve screw can then be screwed into the insert to create an airtight seal.



Figure 5.14: The valve assembly for the box. The left image shows the completed assembly on the box. The center image shows the valve insert. The right image shows the valve screw.

5.5.5 Wire Doors and Gloves

The previous sections have detailed all of the steps necessary for making an airtight box, but the true advantage of our design is its ability to accommodate various equipment and allow manual operation from outside the box. In this section, we discuss how to create airtight electrical, optical, liquid, and gaseous connections, thereby enabling the control of complex processes inside the humidity-controlled chamber. We also describe our simple method for adding gloves to the chamber to allow for manual manipulation of equipment inside.

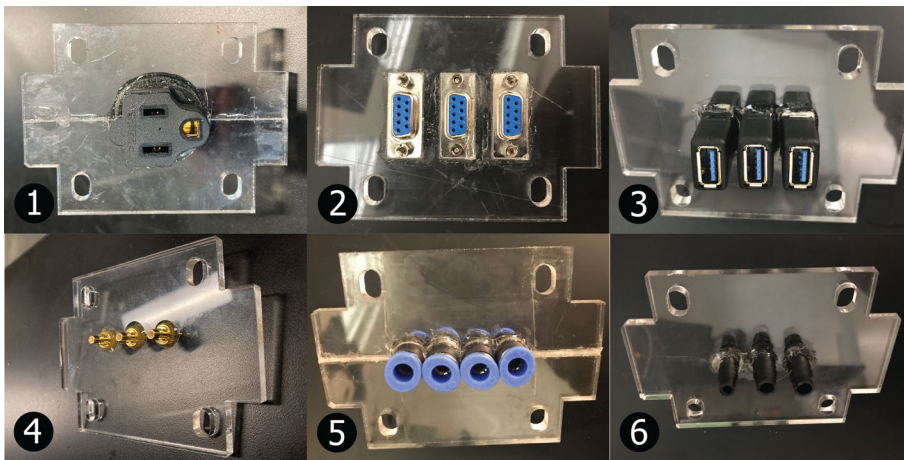


Figure 5.15: Six doors made by epoxying female-to-female connectors into the acrylic piece. (1) AC power. (2) VGA cables. (3) USB cables. (4) SMA cables. (5) Quick connectors for gas tubing. (6) Male PVC tubing connectors.

To create a flexible, airtight method of getting electrical wires, optical fibers, and various fluids into the box we create modular “wire doors” that can be placed over identical holes in the faces of the box. These doors are small 1/4" acrylic pieces with connectors (wires, fibers, tubes, etc.) running through them. The method for creating an airtight seal between

the wire doors and the box surface was detailed in section 5.5.3 Main Assembly. The rubber window seal is compressed using 1/4"-20 bolts between the two pieces of acrylic. The method for creating an airtight seal between the door and the wires, however, is different for each door.

There are two different methods for creating the seal between the wires and the doors. The first is preferred because it is more reliable, but it is not always feasible due to the connections required. A female-to-female connector is simply epoxied into a hole in the door. Some connectors available online may not be fully airtight, so (depending on the experimental needs) it may be necessary to disassemble and fill them with hot glue. (USB and VGA connectors required this extra step in our case.) The hole for the connector can be drilled or cut using a laser cutter. Male connecting wires are then connected to either side of the door to create a connection. This method is shown in figure 5.15 for (1) AC power, (2) VGA cables, (3) USB cables, (4) SMA cables, (5) quick connectors for gas tubing, and (6) male PVC tubing connectors. Doors for a variety of other connectors can easily be constructed using the same methodology.

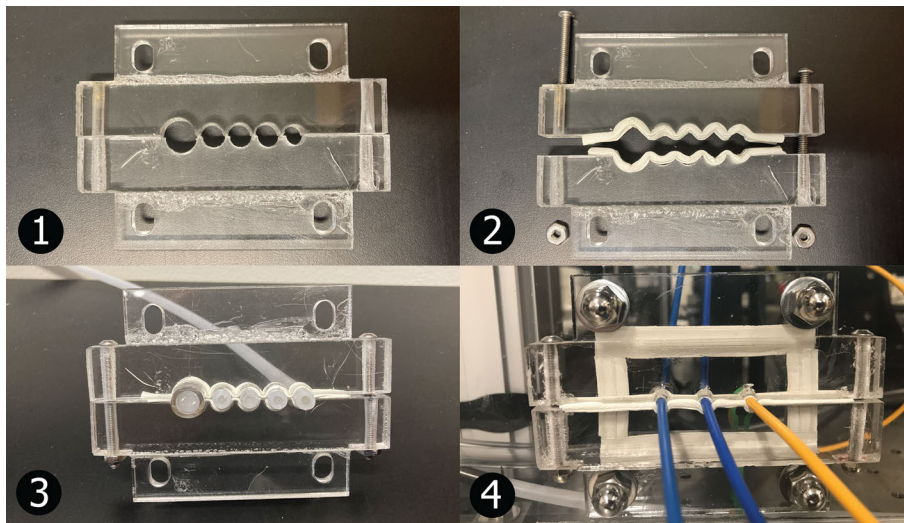


Figure 5.16: Process for making wire doors using the secondary foam sealant method. (1) Holes are drilled along the center line and vertically through the sides. (2) foam is placed along the center line holes and screws are threaded through the holes in the sides. (3) The tubes or wires are clamped by the foam using the screws. (4) Completed wire door for optical fibers.

For some applications, a female-to-female connector may be difficult to obtain, expensive, or inconvenient. This is when the second method for making airtight doors is used, which is shown in figure 5.16. These doors are comprised of two 1/4" pieces of acrylic glued together using weld-on-16 acrylic cement in order to make them 1/2" thick. Once the two pieces are glued, holes slightly larger than the diameter of the cables are drilled along the center line (figure 5.16(1)). Following this, the doors are cut along the center line and drilled along the edges to make shafts for bolts to run between the two halves, as shown in figure 5.16(2). Next,

foam window seal is placed on each half of the wire door along the plane where the cut was made, traveling down into the drilled holes for the wires (see figure 5.16(2)). Finally, the two halves are placed around the wires and bolted together using two 6/32x1 5/8" bolts. This compresses the foam against the cables creating an airtight seal. This design works well for small-diameter cables but is less reliable for larger-diameter cables. We specifically use this for optical fibers, as shown in figure 5.16(4).

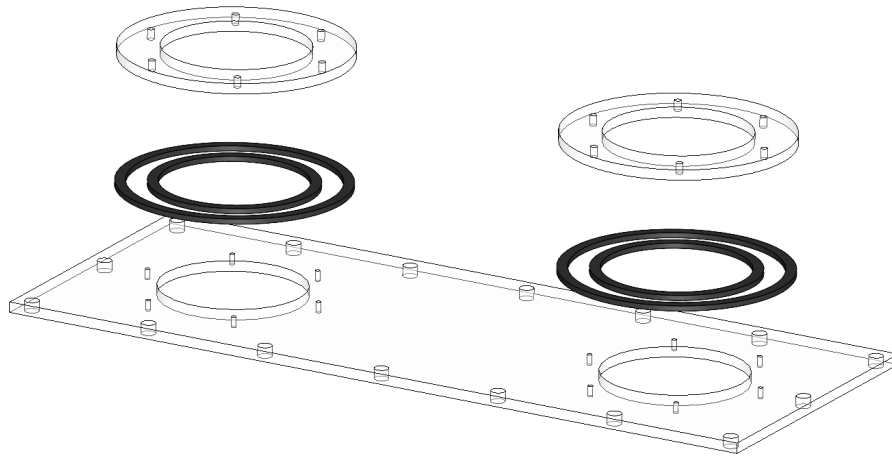


Figure 5.17: Acrylic pieces used to construct the glove door assembly.

To enable manual access inside the box, we designed a method for attaching gloves to the main door of the box. The gloves are bolted to a small panel that is then attached to the door. The acrylic parts needed for this assembly are shown in figure 5.17. The acrylic pieces can be laser cut using the files supplied in the Mendeley database. Parts G and Ga are cut from clear 1/4" acrylic. The glove ring parts are cut from 1/8" black acrylic. The small holes in part G should be tapped for 6/32 threads. Then 6/32x3/4" bolts can be epoxied into the threaded holes.

Once the acrylic pieces are cut, they are assembled into the door. Figure 5.18 shows the 4 steps for assembling the glove door. First, wrap the rubber glove around the smaller glove ring. Second, slip the glove through the large circular hole in part G, which should have 6/32x3/4 bolts epoxied already. Place the larger glove ring on the outside of the bolts. This ring provides support for the acrylic of part G. Third, place part Ga atop the other disks. Fourth, after aligning the smaller glove ring with the inside of part Ga and the larger ring with the outside of the same part, bolt the assembly together using 6/32 acorn nuts. Our design has the advantage of flexibility. The gloves we used are thin rubber latex gloves, but these can be exchanged for any similar rubber gloves. The gloves act as their own gasket, so they must be compressible and airtight. Using this design, it is also easy to replace gloves if they become worn.



Figure 5.18: Process for assembling the glove door. (1) Wrap the glove around the small ring. (2) Place the small and large rings on the door. (3) Place the top ring over the bottom rings. (4) Bolt the ring using acorn nuts.

5.5.6 Environmental Control

In this section, we detail the construction of a fan-aided chemical desiccator along with a TEC to control the humidity and temperature of a sample, respectively.

The first major objective of the box is to be able to lower the interior humidity quickly for use in research environments. We achieve this rapid absorption of water vapor by pushing air through a large surface area of desiccant inside the desiccator. Our design is a tower with a 12V computer fan on the top, modular packets of silica gel beads inserted into the column, and a tray of silica gel beads placed on the bottom. The silica gel components are shown in figure 5.19. The pouches are rectangular, $4 \times 8 \frac{1}{2}$ " in size, and $\frac{1}{2}$ " thick. They are constructed using fine steel mesh and steel caps that are bolted to the ends using $\frac{6}{32}$ bolts and acorn nuts. The base tray is similarly constructed using fine steel mesh with the top open. The use of metal components for the desiccant packets allows the beads to be reactivated in an oven without the need to remove the beads from the packets.

The end caps for the pouches were designed using the SolidWorks sheet metal tool to increase repeatability and accuracy. To create the end caps, we recommend printing out and taping an unfolded version of the part to a piece of steel $\frac{1}{32}$ " sheet metal. Using the paper outline as a guide, cut the sheet metal and drill out the holes using a $\frac{7}{64}$ " bit. Then bend the metal into shape using a press brake. The longer sides should be bent first, then the smaller sides. The smaller sides can be hammered into place if needed. Eight of these caps should be made, with each of the four pouches having two end caps.

The wire mesh part of the pouches is made of a 255 mm \times 21.8 cm rectangle of fine steel mesh (about 1 mm square holes) and bent into a hollow box. As precise dimensions are not needed for this component, the bend locations in the mesh can be estimated by sliding the mesh into the end cap. Ultimately, the mesh will be bent into a rectangular prism



Figure 5.19: Silica gel packet and bottom silica gel tray inside the desiccator.

that is placed between two of the steel end caps. The original piece of steel mesh is designed with extra material so that the mesh can be folded over itself, which helps hold the shape of the pouch and prevents beads from falling out. Use pliers to make this crimp.

Once the wire mesh for the pouch is bent into shape, insert a cap onto either end of the mesh, ensuring that the mesh is pushed in all the way. Using a permanent marker, mark the spots on the mesh that meet the drilled holes. Then take the end caps off and use the cutters to make a hole just large enough for the 6/32 screws to pass through. Secure one cap using 3/4" long 6/32 screws and nuts. Fill the pouch with silica beads, then attach the second cap in the same manner. Repeat for the other three pouches.

The bottom tray is also constructed out of fine mesh. The tray is made out of a 166 mm x 166 mm piece of mesh that is bent into a 115 mm x 115 mm x 25 mm tray. Two sides of the tray have securing flaps that allow bolts to go through and hold the shape of the tray together. Use a paper stencil that has a 166 mm square with four 25 mm lines that are parallel to one side of the square. The 25 mm lines are 25 mm from the side of the square. After the bends are made, cut out holes large enough for 6/32 screws in the flap and the mesh beneath the flap. Insert the bolts and attach nuts onto the other side.

The packets and base tray are now filled with silica gel beads and can be heated in an oven or on a hot plate to reactivate them. Alternatively, the beads can be removed from the packets to be reactivated or replaced. The beads we have listed in our bill of materials reactivate when heated to 150 °C for 1.5 hours. Most desiccant beads include color-changing beads to indicate when beads need to be reactivated. These orange beads can be seen in figure 5.19. If necessary, beads can also be replaced or reactivated when their performance declines.

The casing for the desiccator is made from 1/4" acrylic and was laser cut using the files available on our Mendeley database. These pieces are held together using 3D printed corner pieces and 6/32 bolts. The

acrylic is tapped and bolts are screwed into the holes, pointing outward. The 3D printed fastenings are placed on the corners and acorn nuts are used to secure the pieces. Railings are attached instead of regular corner pieces on the two edges where the door will be placed. These allow a sliding door to go on the front of the desiccator. A CAD rendering of the acrylic pieces along with a final assembly of the entire desiccator is shown in figure 5.20. Because the desiccator is placed inside the airtight box, the desiccator will slowly reduce the humidity in the box if the desiccator is not airtight, even if the fan is turned off. In the case of experiments running at extremely low humidities, this is completely acceptable and the desiccator need not be airtight. If precise humidity control is needed over an extended time period, efforts should be made to make the desiccator airtight, such as taping over the acrylic corners or installing flaps over the vents.

The second objective of the box is for the TEC to be able to reach cold temperatures quickly and precisely. The TEC is composed of an electrically powered Peltier tablet and a water-cooled aluminum block that are both inserted into the FDM print. The Peltier tablet moves heat energy from its top surface to the bottom surface, which is in contact with the aluminum cooling block with silver thermal grease between them. The aluminum block is hollow and has cold water running through it to remove the heat energy from the Peltier tablet, cooling the system further and allowing the top Peltier tablet surface to reach temperatures as low as $-18\text{ }^{\circ}\text{C}$. The water is pumped in from a tank outside the box using a 12 V submersible pump. For typical operations near $0\text{ }^{\circ}\text{C}$, the water tank can be filled with room-temperature water. For colder applications, we recommend adding ice to the tank.

The Peltier tablet is powered from a 12 V 6 A power supply that is

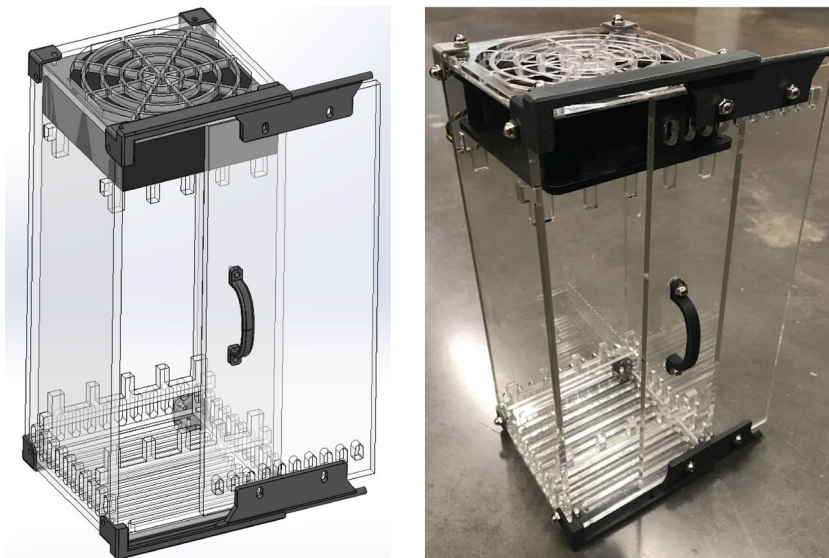


Figure 5.20: CAD rendering and actual assembly of fan-assisted chemical desiccator.

switched on via a high-power MOSFET. To measure the temperature of the surface of the Peltier tablet, we use a TMP36 temperature sensor [97] that is coated in thermal grease and inserted into a small crevice in the FDM print where it contacts the Peltier tablet. Once a good thermal connection is confirmed, the sensor is hot-glued in place. The assembled TEC is shown in figure 5.21.

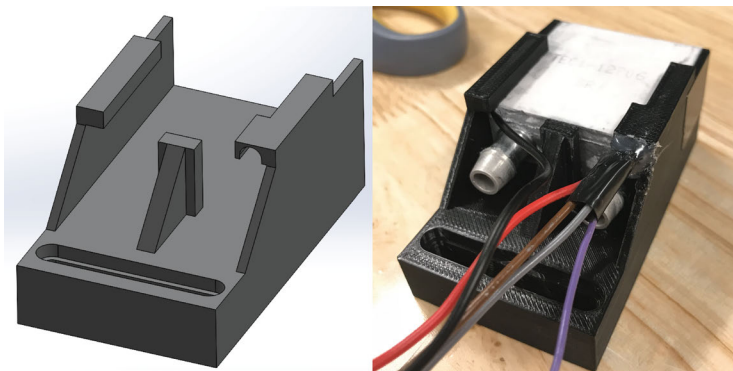


Figure 5.21: CAD rendering and actual assembly of the TEC.

5.5.7 Electronics

To maximize the utility of OSCBox, it is necessary for its functionality to be remotely accessible. This includes reading the humidity and temperature values, as well as activating the desiccator and TEC. This is accomplished using a Python package developed in our lab called Pyrolab [96], designed for remote-accessing laboratory equipment and streaming data to any computer with Pyrolab installed. We provide a Pyrolab driver for OSCBox with functions to read, record, and control the humidity and temperature within the box. Other functions can be added to increase the usefulness of the box. Pyrolab is perfect for these applications because it can be run on a Raspberry Pi, enabling us to easily wire our various components directly to the computer. The Mendeley database contains code for the box driver as well as code for a graphical user interface (GUI) that can be run on a separate computer to conveniently control the box functions and receive information about the box temperature and humidity. Figure 5.22 shows a block diagram of the Pyrolab connections. The details for establishing this server/client relationship can be found in the Pyrolab documentation.

The Adafruit Si7021 humidity sensor [98] is used in the box to collect humidity data, and a 3.3 V relay is used to control the desiccator fan. The driver software provides convenient functions that control the fan to maintain the humidity at a given value.

The TEC temperature is monitored using a TMP36 temperature sensor that produces an analog output and thus can be read by an analog to digital converter (ADC). Since the Raspberry Pi does not include an ADC, we use an Arduino Nano to read the temperature value. The Arduino Nano also provides the control signal to a power transistor to provide

power to the TEC. As with the humidity control, the provided software enables the user to set a desired temperature value, and the TEC will be controlled to maintain that value. In some cases, excess noise may be induced in the temperature reading due to long wire lengths between the TMP36 and the Arduino Nano. In this case, an I2C ADC may be added closer to the temperature sensor.

To provide additional feedback to the user, we have implemented LEDs and an LCD screen as optional components. These provide a visual representation of the current humidity and temperature inside the box. The LEDs are controlled through the Raspberry Pi, but the data line must be run through a 3.3V to 5V level converter. The LCD screen is controlled via I2C from the Raspberry Pi.

Because of the complexity of the electrical systems, we have included a circuit board design in Eagle and a detailed schematic for easy replication (found in the Mendeley database).

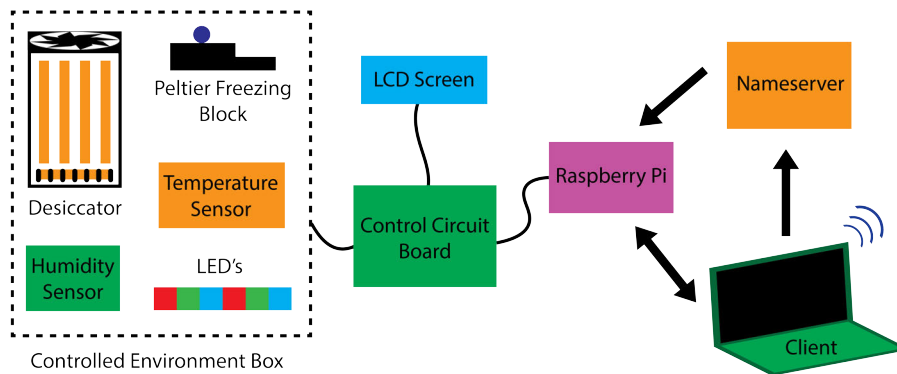


Figure 5.22: Pyrolab is used to access the electrical components of the box remotely.

5.6 Operation Instructions

While the construction of this humidity-controlled environment is complex and involved, the operation is comparatively simple. A few preparatory steps should be taken for operation. Before attempting to change the humidity in the box, ensure that all doors and ports are sealed tightly and that the silica beads in the desiccator are active. If they have become too saturated, reactivate or replace them before use. The beads can be reactivated by heating them to 150 °C for 1.5 hours. Before activating the TEC, ensure that the water cooling pump is turned on and that the tank is sufficiently full. If very low temperatures are needed, add ice to the tank. The pump should always be run while the TEC is in use.

OSCBox is most conveniently controlled using the provided GUI. Using Pyrolab, the humidity in the box and temperature of the TEC can be observed and controlled by any computer with internet access. The GUI allows easy, graphical access to all of the functions of the box (shown in figure 5.23), including temperature control, humidity control, LCD

screen control, LED strip control, and the plotted data with plot control. These functions are further explained below.

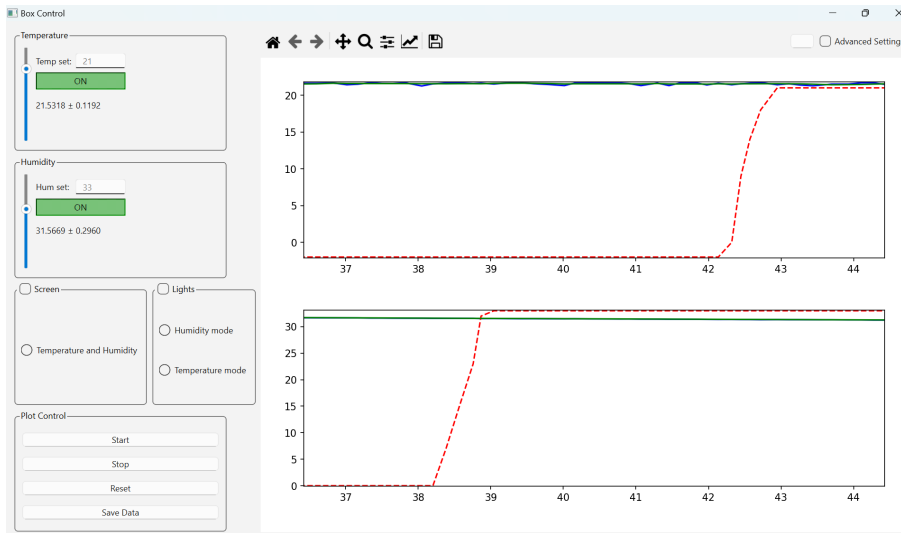


Figure 5.23: Graphical User Interface for OSCBox.

The temperature control box is located in the top left of the GUI and is shown in detail in figure 5.24. The box contains a slider on the left edge and a text input box at the top. These can be used to change the set point for the TEC. The slider will change the set temperature to an integer value in the range of -20°C to 30°C . If a different range is desired, the code can be edited to allow such. When a value is typed in the text input box and enter is pressed, the box will change the temperature to the provided float value (within the same range).

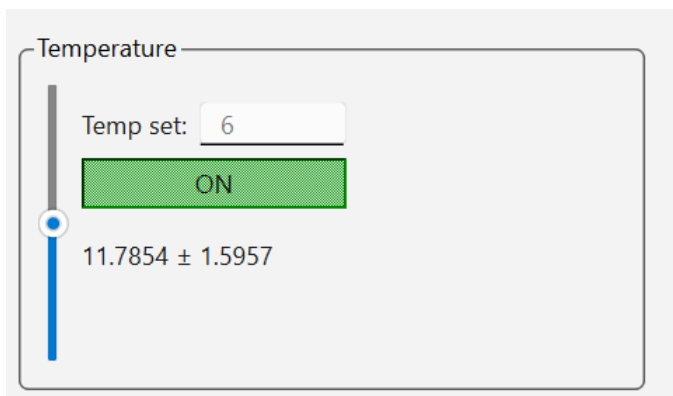


Figure 5.24: Temperature box of the GUI.

The TEC is activated when the temperature control button near the center of the box is clicked. The button will then be labeled "On" or "Off" depending on the state of the control. If the label for the button becomes "ERR," then the Raspberry Pi is not connected and the GUI must be

restarted. The GUI also displays the current temperature directly under the temperature control button. A running average of the last 8 seconds of the temperature appears directly under the activation button, as well as the maximum deviation from the average during the same period. This temperature reading may not be accurate when the temperature experiences large changes over the 8 second period or immediately after the data collection begins.

The humidity control box contains the same functions, and the humidity value can be set within a range from 0% to 50% Relative Humidity (RH). If control above 50% RH is desired, the code can be edited to allow such. The slider, text input, and humidity control button function identically to the temperature control options, as seen in figure 5.25. The running average and deviation for the humidity value operates identically to the running average in the temperature box.

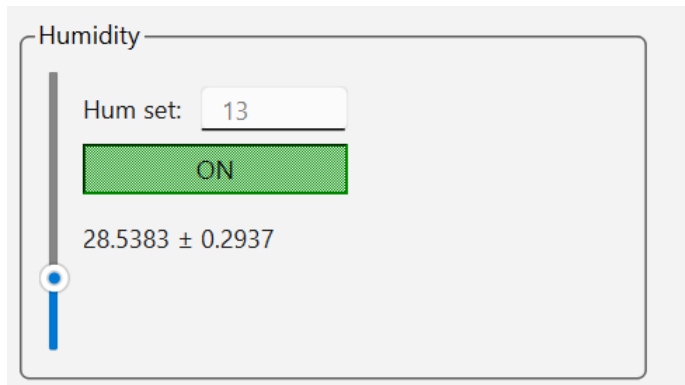


Figure 5.25: Humidity box of the GUI.

As an example, we now describe the steps needed to operate the box at a target temperature of 0.5 °C and a relative humidity of 4%. After ensuring the box is sealed and the water cooling system is active, type the value “0.5” into the temperature text input and press enter. Next, click temperature control button. The target temperature is now set and the TEC control is active. The temperature control button should read “ON”. Next, click and drag the humidity slider until the text box displays “4”, then click the humidity control button. The humidity control is now active and the humidity control button will read “ON”. The running averages and the plot, if running, will display the decreasing temperature and humidity.

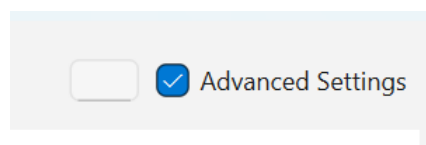
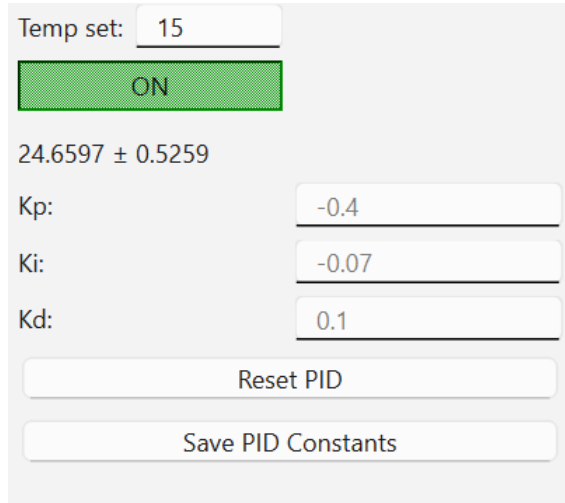


Figure 5.26: Advanced settings button on the GUI.

The control parameters for the temperature and humidity can be

accessed and modified using the “Advanced Settings” checkbox on the top right corner of the GUI, as seen in figure 5.26. Checking the box shows the underlying control system constants for both the temperature and humidity control in their respective boxes, as seen in figure 5.27.



The screenshot displays the advanced PID control settings for the TEC. At the top, the temperature setpoint is 15. A green button labeled 'ON' is visible. Below this, the current temperature is shown as 24.6597 ± 0.5259. Three input fields are provided for the PID constants: Kp is -0.4, Ki is -0.07, and Kd is 0.1. At the bottom, there are two buttons: 'Reset PID' and 'Save PID Constants'.

Figure 5.27: PID control advanced options for the TEC.

The temperature is controlled using a proportional-integral-derivative (PID) controller. Each of the three constants can be modified using a text input box. The proportional constant K_p and the integral constant K_i are bounded within -1 and 0 , while the derivative constant K_d is bounded between 0 and 1 . The “Reset PID” fetches saved constants from the “pid_constants.txt” and inputs those into the functions. The “Save PID Constants” button saves the current constants into the “pid_constants.txt” file.

The humidity controller is only able to turn the fan on or off, without control over its speed. The fan control depends on a derivative time constant to prevent overshoot. The controller calculates the derivative of the humidity, then projects the future humidity using the humidity time constant. If the projected value is above the set point, the fan is turned on. If not, the fan is turned off. This derivative time can be modified using its text box. The input is not bounded, but a time of at least 20 seconds is recommended to prevent overshoot. Longer derivative times result in a slower response but are less likely to overshoot. Advanced settings include the derivative time constant, with similar save and default options, as seen in figure 5.28, where the Humidity Time (s) is the derivative time constant. The “Set Default Humidity Time” and “Save Time Constant” buttons function the same way as the temperature advanced options, using the “time_constant.txt” file to store the constant.

Figure 5.28: Humidity control advanced options.

Below the temperature and humidity control boxes are two boxes for controlling the optional LCD screen and LEDs, as seen in figure 5.29. Both functions use a checkbox in the top left corner to activate the device. Once the device is active, the buttons inside each section are used to set the mode of the respective LCD screen or LED strip.

Figure 5.29: LED and LCD control boxes of the GUI.

In the LCD control box, the “Temperature and Humidity” option displays the current values of the box on the LCD screen. While the LCD control currently has only one option, we provide this framework to facilitate the addition of new display options. The `rasberrypibox.py` driver code has a function, `load_lcd_data`, which allows you to load any desired data from Pyrolab and display it on the LCD screen. The LED control has two options. The first is humidity mode, which will change the color of the LEDs to indicate relative humidity levels. The second is the temperature mode, which changes the color of the LEDs to indicate the TEC temperature.

The right side of the GUI contains plots showing live feeds of the temperature and humidity inside OSCBox. These plots scroll to display only the last 8 seconds of data while active, though up to 30 minutes of data can be stored and viewed in the GUI plots. If longer sets of data are desired, the code can be edited to lengthen the data limit or remove it. This should be done with caution, however, because if the data gets excessively long the program can become unresponsive.

The plot control box is located at the bottom left of the GUI. Four buttons control the data collection: “Start,” “Stop,” “Reset,” and “Save

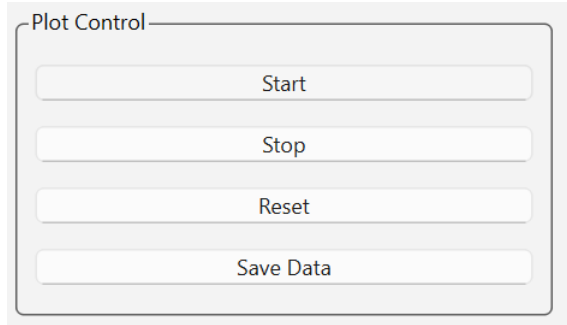


Figure 5.30: Plot control buttons of the GUI.

Data,” as seen in figure 5.30. Clicking the “Start” button starts or unpauses the plot in the GUI. Clicking the “Stop” button will pause the plot and allow more of the data to be shown and manipulated using the plot controls in the taskbar. Clicking the “Reset” button stops the data collection if it is running and sets a flag to clear the data once “Start” is pressed again. The running average of both the temperature and humidity will also be frozen until “Start” is pressed to start the data collection. The data collected will not be reset in the GUI until “Start” is pressed again. The “Save Data” button saves the current data to a .npz file. The GUI code can be modified if other file types are desired.



Figure 5.31: Plot taskbar for manipulating plot views while the collection is paused.

The plot taskbar, as seen in figure 5.31, has multiple standard functions. It has a home button that sets the current view to the last set view, i.e., the last plot update. There are two arrows, left and right pointing, that function as undo and redo buttons. The four-pointed arrow sign functions as a panning feature and can zoom along axes while holding right-click. The magnifying glass functions as a drag-to-zoom feature with left-click zooming in and right-click zooming out, as seen in figure 5.32. The save icon saves a picture of the current plots. If the data needs further manipulation, we recommend saving the data using the “Save Data” button in the plot control area.

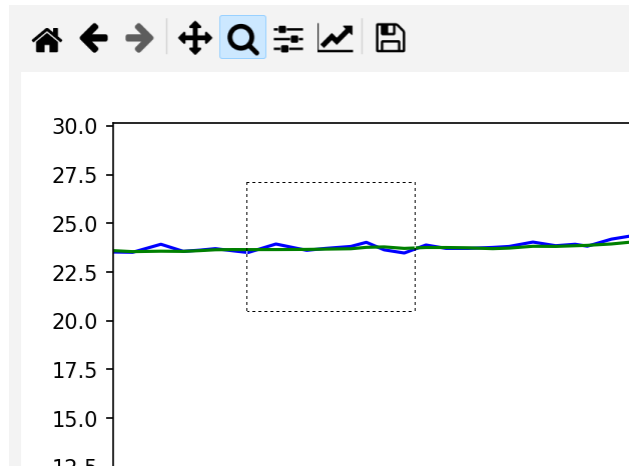


Figure 5.32: Magnifying glass feature of the plot.

5.7 Validation and Characterization

OSCBox operates at extremely low humidity with components at low temperatures. Our chamber is designed to consistently reduce the relative humidity to any desired level, including 0%, quickly and accurately. Our design accomplishes this task, which we verify in this section. We also characterize the control of temperature we achieve with the TEC and comment on the entire system's usefulness in a laboratory setting.

Please note that the humidity sensor we use for tracking the internal relative humidity [98] states that the sensor can have an error of up to $\pm 3\%$ with a nominal error of less than 2%. We observed that a sensor reading of -2.3% corresponded to a true relative humidity of 0%. Consequently, we add a 2.3% linear offset to all data and charts presented here.

We performed analysis of two use cases for humidity control. The first is to reduce the humidity as much as possible in as short a time as possible. The second is to regulate the humidity to specific values.

For the first test, we run a series of 30-minute trials starting with 32% relative humidity inside the box at a temperature of 22 ± 1 °C. The first trial uses recently reactivated silica beads and each successive trial reuses the same desiccant. The results are shown in figure 5.33. The five trials reach a relative humidity of 0.0%, 0.9%, 2.4%, 3.9%, and 5.4% respectively after 30 minutes of running inside the box. The data shows each successive test reaching a slightly higher relative humidity after the desiccator has run for 30 minutes. The first two iterations both reach below 1%, while the later three do not in the allotted time. The degradation of the water absorption rate can be counteracted in part by stirring the base tray, which will bring drier beads to the surface. However, based on these results, we suggest that if it takes greater than 15 minutes to reach 2% relative humidity, the beads should be reactivated if minimal humidity is desired.

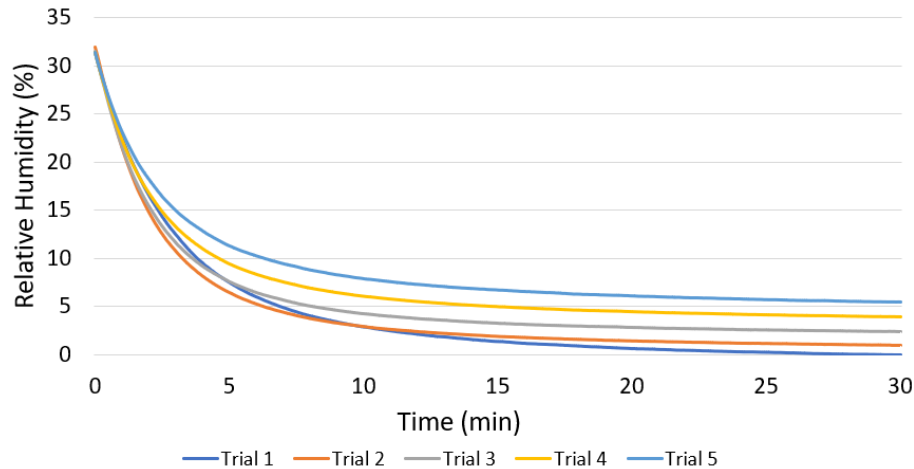


Figure 5.33: Five 30-minute trials testing the fan-aided chemical desiccator with repeated use.

An additional test is performed to determine the longevity of the desiccator. The chamber starts at 37% relative humidity and runs for 90 hours to observe how long the desiccator can maintain an ultra-low humidity. The results are shown in figure 5.34. The relative humidity reaches 2% in 15 minutes and reaches 0% in 1 hour. From there, the humidity remains at 0% for another 9 hours. The humidity rises above 2% after an additional 65 hours.

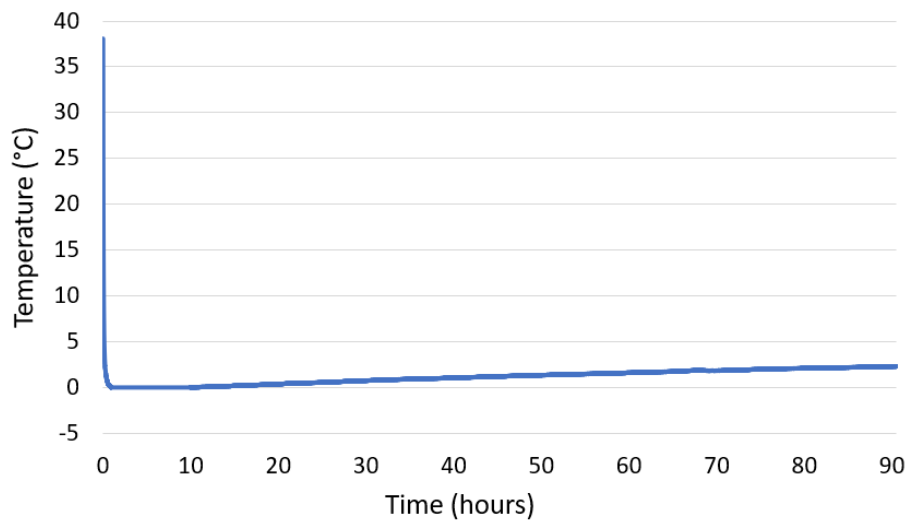


Figure 5.34: Humidity over the course of 90 hours with the desiccator running.

Precise target humidity control was then tested to measure the box’s capability of maintaining specific humidity levels. For this experiment, the chamber starts at 37% relative humidity. Next, a target value is set, held for a time, then lowered to the next test point. The results are shown in figure 5.35. At higher humidity values, the response time is approximately 3 minutes, while at lower humidity values the response

time is nearly 5 minutes. We would expect larger steps to result in longer response times. Typically, the humidity will settle within 0.5% of the set value. In some cases, more overshoot can occur, but it is typically limited to be within 1% of the set value. Also, as mentioned above, over time the humidity can slowly decrease as the desiccant absorbs more water. This effect can be mitigated by sealing the desiccator as much as possible. Note that when the box is fully sealed, there is no mechanism for raising the humidity level. If the humidity becomes lower than desired and the humidity needs to be raised, the box must be opened to allow external air to enter. OSCBox includes small valves that can be used for this purpose.

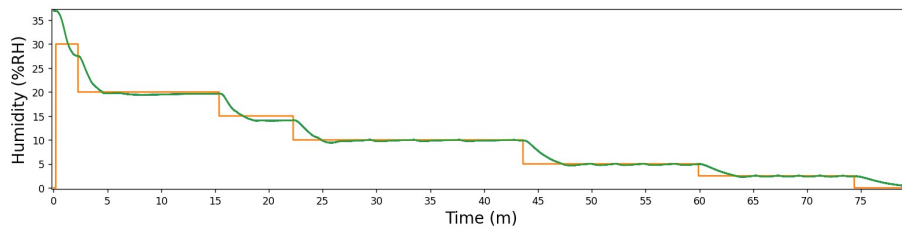


Figure 5.35: Precise humidity control over 80 minutes.

Next, we test the TEC and accompanying PID controller to verify its performance at temperatures near freezing. The TEC is capable of reaching temperatures as low as -18°C when run at full power. Here we show only data near freezing, as the PID parameters have been optimized for this range. If a different range is desired, the PID parameters may need to be adjusted. In this test, we supply temperature commands ranging from -5°C to 10°C and observe the controller's response (shown in figure 5.36). The controller reliably reaches a new target temperature with a variation of $\pm 0.5^{\circ}\text{C}$ within 30 seconds and settles to a variation of $\pm 0.25^{\circ}\text{C}$ within a minute.

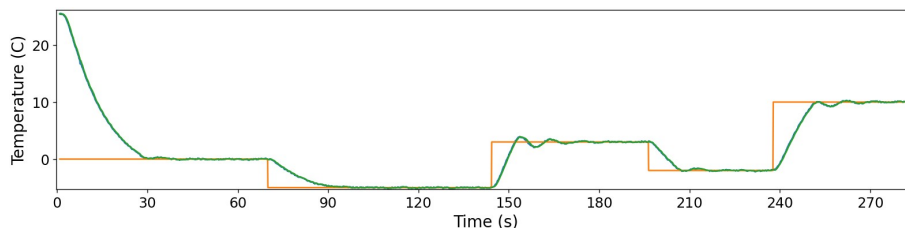


Figure 5.36: Target temperature and controller response plotted for 5 minutes.

An additional test to measure the consistency of the temperature was taken over the duration of half an hour within a temperature range of -6°C to 2°C . The test result is shown in figure 5.37. As seen with the previous dataset, the temperature reaches a new target temperature with a variation of $\pm 0.5^{\circ}\text{C}$ within 30 seconds and of $\pm 0.25^{\circ}\text{C}$ within 1 minute.

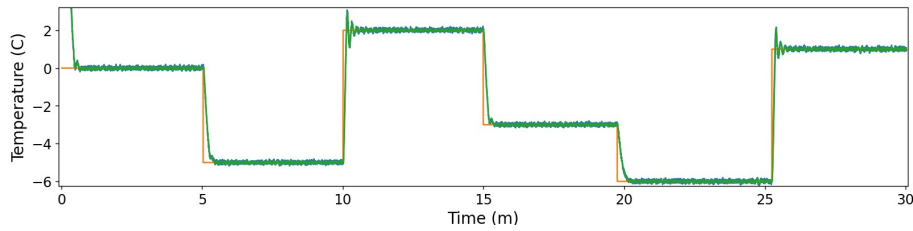


Figure 5.37: Target temperature and controller response plotted for 30 minutes.

The final test is a proof-of-functionality via observation. One of the applications of OSCBox is the control of humidity and temperature for regulating ice crystal growth. To test our control of this growth, we froze three water micro-droplets at $-5\text{ }^{\circ}\text{C}$ and observed the effects of different humidity levels on the growth of ice crystals on the droplets over a period of five minutes. It is important here to note the effect of temperature on relative humidity. Relative humidity is a measure of the vapor pressure of the air compared to the saturation vapor pressure, which depends on the temperature. Thus, if warm air has the same water vapor pressure as cold air, the cold air will have a higher relative humidity than the warm air. We will report the relative humidities of the environment (at $22\text{ }^{\circ}\text{C}$) for this experiment; however, near the cold ice droplet and TEC, the relative humidity will be higher.

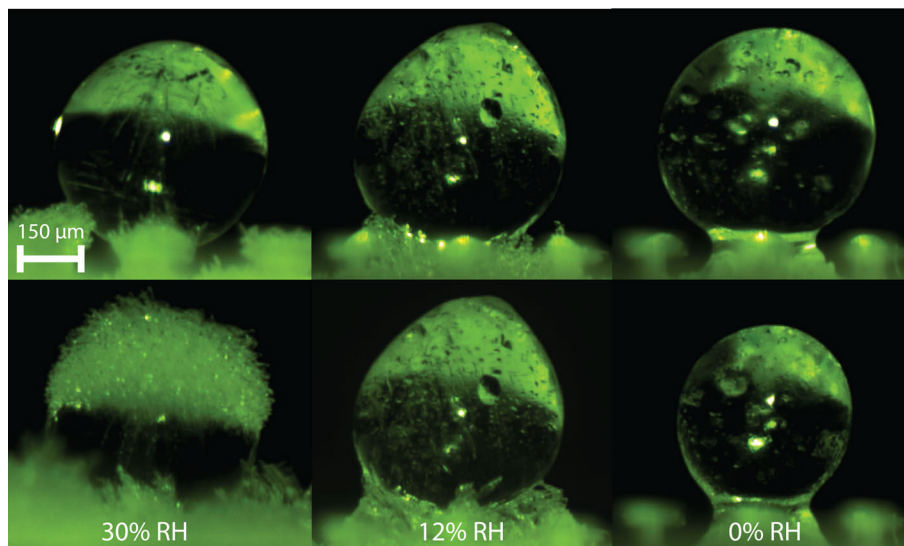


Figure 5.38: Three droplets frozen at different humidity levels (top) and observed after 5 minutes (bottom).

The experiment was performed at 30%, 12%, and 0% humidity levels. The results of each test are shown in figure 5.38, with the top frames showing the droplets at the beginning of the 5-minute period and the lower frames showing the droplet after the 5-minute period. The first test (shown in the leftmost frames of figure 5.38) was performed at 30% humidity. This produced oversaturated air at $-5\text{ }^{\circ}\text{C}$, resulting in

heavy deposition of water vapor onto the droplet, seen as crystal growth. For the second test (shown in the center frames of figure 5.38), we experimentally found the relative humidity level at which the deposition and sublimation of water are equivalent (approximately 12% RH) and observed that the ice droplet did not change size and did not experience crystal growth. The third test (shown in the rightmost frames of figure 5.38), was performed at 0% humidity and caused the sublimation of the ice spheroid.

OSCBox is a useful tool for experiments that require temperature and humidity control. Its customizability along with its optimal performance allows researchers in a variety of fields to execute experiments in a controlled environment.

5.7.1 Summary

- Able to reduce the humidity to less than 1% in under 30 minutes.
- Able to maintain humidity below 2% for over 70 hours.
- Able to maintain set humidity within 0.5%
- Able to reach target humidity within 5 minutes (for small steps).
- Able to reach temperatures as low as $-18\text{ }^{\circ}\text{C}$.
- Able to maintain set temperature within $0.25\text{ }^{\circ}\text{C}$.
- Able to reach target temperature within 30 seconds.

Automated Fabrication of Tapered and Dimpled Optical Fibers

This chapter is composed from a paper entitled “Automated Fabrication of Tapered and Dimpled Optical Fibers” prepared for publication in the journal *EPJ Techniques and Instrumentation*.

6.1 Introduction

The growing role of integrated photonic circuits in research has led to an increased development and interest in unique materials platforms and device geometries. Many of these devices include undercut structures, which are very difficult to couple to using waveguides due to the lack of supporting material, such as microdisk resonators [42, 44–51] and nanobeams [52–54]. These structures often facilitate the investigation of optomechanical interactions [42, 44, 48–54] or quantum optical effects [47, 52–54] and allow fabrication in different materials, such as diamond [47, 52, 54]. As a result, tapered and dimpled optical fibers [42, 51] have been used to allow optical coupling to these isolated devices.

We build on the excellent work done previously in describing the methods for fabricating tapered and dimpled optical fibers [42, 51]. Though these works were essential to researchers seeking to use dimpled optical fibers, the manual nature of the dimpled fiber fabrication process requires extensive training for new researchers and significant time in the fabrication process. Additionally, the uniformity of manually fabricated dimpled fibers is likely to suffer from human variations in the process, making their creation less repeatable.

In this work we present a fully functional system for the automated fabrication of tapered and dimpled optical fibers. By integrating motorized stages, a laser source, an oscilloscope, a camera, and a torch into a single unified system, the user is able to fabricate a tapered or dimpled fiber at the touch of a button. The system analyzes output from the oscilloscope and uses computer vision techniques to analyze the camera feed in order to fully automate the tapering and dimpling process. The system is capable of producing tapered and dimpled optical fibers with optical efficiencies of over 90% with high repeatability. The system requires minimal training for new users and can create a tapered and dimpled fiber in under 10 minutes.

6.2 System Overview

We here provide a description of the hardware and software used in our automated fiber tapering and dimpling system.

6.2.1 Hardware

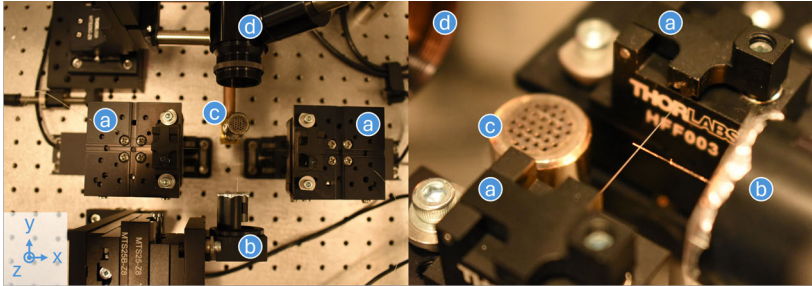


Figure 6.1: Fiber tapering and dimpling system. (a) Pulling stages, one-axis motors with fiber clamps. (b) Guide fiber with two-axis motorized control. (c) Hydrogen torch with two-axis motorized control. (d) Camera with vertical motorized control.

Figure 6.1 shows the fiber tapering and dimpling system, with coordinate axes in the lower left corner. In the following description, directions will be referenced by their axes (x , y , z), and in later sections, the directions will be referenced as lateral (x), horizontal (y), and vertical (z). The pulling stages are labeled (a) and each consists of a linear motorized stage (Thorlabs MTS25-Z8) oriented in the x direction with alignment stages and fiber clamps raised above them. The alignment stages are five-axis manual stages (Thorlabs PY005), allowing all needed degrees of freedom to precisely align the fiber clamps (Thorlabs HFF003), and therefore the two sides of the fiber. These pulling stages are responsible for pulling the fiber during the tapering process and providing the lateral motion of the fiber during dimpling. The guide fiber is labeled (b) in figure 6.1 and consists of a stripped and cleaned optical fiber held in a fiber clamp (Thorlabs SM1F1-250) with motorized control (Thorlabs MTS25-Z8) in the y and z directions and manual control in the x direction (Thorlabs DTS25). This guide fiber will be used to ensure the dimple forms in the proper shape. The guide fiber assembly can also be removed entirely and replaced with a custom fiber holder, which allows the dimpled fiber to be removed from the setup. In figure 6.1, (c) shows the hydrogen torch, which has motorized control in the y and z directions (Thorlabs MTS25-Z8) and manual control in the x direction (Thorlabs LT1). The torch is used for heating the fiber to its softening point for tapering and for annealing the dimple. The torch is custom built from 1/8" NPT pipe and fittings with a National Torch HT-3 tip. Hydrogen flow to the torch is established using a flowmeter (Masterflex 32003-06) set to 130 sccm. In figure 6.1, (d) shows the camera, which has motorized control in the z direction (Thorlabs PT1-Z9) and manual control in the x and y directions (Thorlabs LT1). The camera consists of a Zelux camera (Thorlabs CS165CU) attached to a zoom lens

system (Navitar 1-60191). The motorized stages are controlled by the user software via motor controllers (Thorlabs KDC101). The system also relies on an optical system to provide the optical throughput power of the fiber as it is tapered. The system uses a laser (Pure Photonics PPCL551), a photodetector (Thorlabs DET10C2), and an oscilloscope (Digilent 410-415).

6.2.2 Software

The software used for our system relies on Pyrolab [96], an open-source Python package developed in our lab. Pyrolab enables remote communication between a client computer and individual devices connected to local servers. Pyrolab is beneficial because it allows for remote control of laboratory equipment, allows devices connected to different computers to be controlled from a single client computer, and enables distribution of processing power among multiple computers. Figure 6.2 shows a graphical representation of the communications made in Pyrolab. First, individual devices (stages, oscilloscope, camera) are connected to local servers. In our system, for example, motorized stages are controlled by motor controllers, which are connected via USB to a computer. These local servers then register these devices with the nameserver, which associates computer addresses with human-readable names. To control the devices, a client first communicates with the nameserver, retrieving the device addresses, which are then used to connect to the individual devices via the local servers. The client can then send commands to multiple devices across multiple local servers as though they were all directly connected to the client.

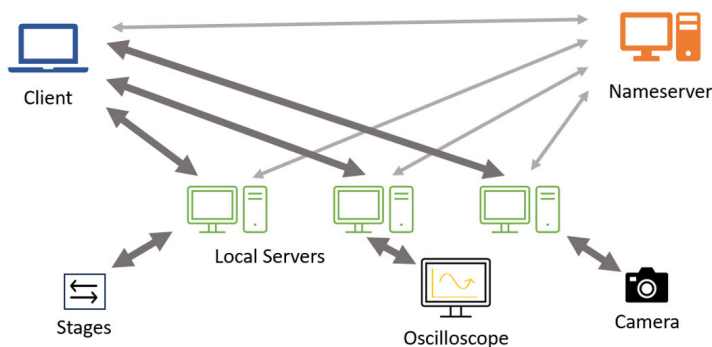


Figure 6.2: Graphical representation of Pyrolab. The client communicates with the nameserver to establish a connection to each of the local servers. Then individual devices can be controlled from the client.

In our system, the client software is run on a laptop, while the local servers are desktop computers in the lab. The client software is responsible for determining the motor movements needed based on the output of the oscilloscope and camera, while the local servers directly perform the motor movement and data collection. The client software produces a graphical user interface (GUI) to allow the user easy access

to the commands needed for fiber tapering and dimpling. The GUI also provides output to the user.

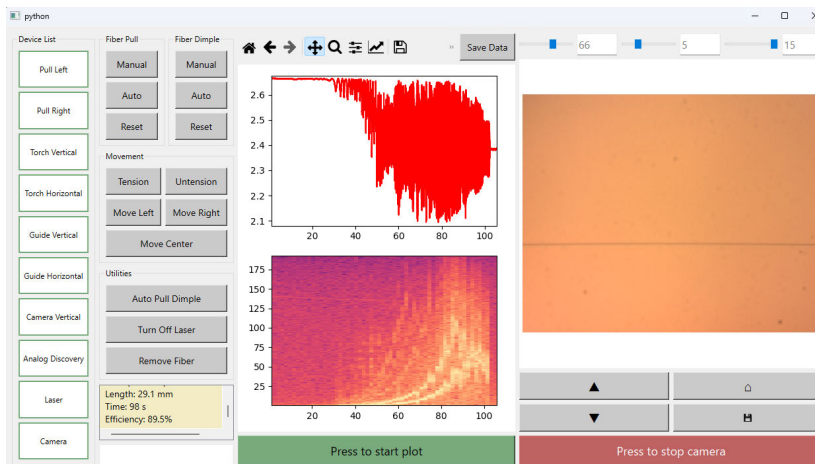


Figure 6.3: A screenshot of the GUI used to control the dimpling system. The program integrates a live camera feed, motor control, and an oscilloscope feed into a single window. It also shows the status of the individual devices as well as a terminal-like interface for input and output. Several buttons allow for convenient access to commonly used commands, and some commands activate keyboard-controlled motion.

Figure 6.3 shows the GUI used to control the fiber dimpling fabrication system. The device list box on the left edge of the window shows the connection status of individual system components and the homing status of motors. To the right of this box, buttons and a text input are provided to allow the user to control the system. The fiber pull and fiber dimple boxes each contain buttons for manual or automated control of the process, as well as a button to cancel and reset the process. The movement box allows the user to perform common motor movements. The utilities box contains buttons for other actions, such as turning the laser on or off. Below this box there is a terminal-like interface to allow the user to enter more customized commands and read textual output. In the center of the GUI, live plots are shown of the power signal (top) and spectrogram (bottom) of the optical throughput of the fiber. The GUI also contains plot manipulation tools above the plot feed and a plot on/off button below it. While running, the feed shows only the last ten seconds of collected data. In figure 6.3, the plot shows the data from a fiber pull. The right side of the GUI shows a live camera feed of the fiber, with camera setting sliders above the feed and control buttons just below the feed. The live camera feed is occasionally overridden to show computer vision algorithm results. In figure 6.3, the camera feed shows a tapered fiber.

6.3 Fiber Fabrication Procedure

We now provide a description of the fiber tapering and dimpling procedure. We will first give a brief overview of the steps involved, then

provide a detailed description of each step.

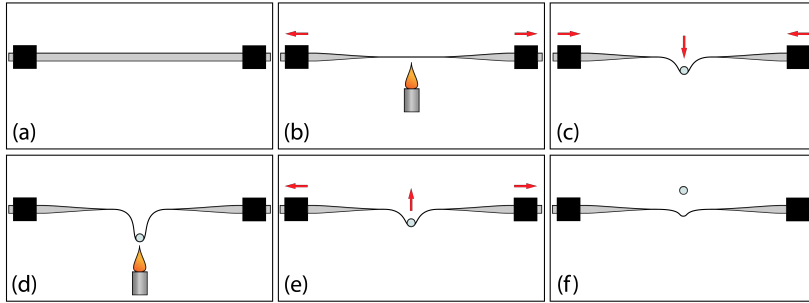


Figure 6.4: Steps for the fabrication of a tapered and dimpled optical fiber. (a) A fiber is clamped onto the pulling stages. (b) The fiber is tapered by moving the pulling stages apart while applying heat to the fiber. (c) The dimple shape is formed by guiding the tapered fiber downward with a guide fiber while moving the pulling stages together. (d) Once the shape is correct, the dimple is annealed. (e) The dimple is released by moving the guide fiber upward while the pulling stages move apart. (f) The guide fiber is carefully detached from the dimple.

Figure 6.4 shows the complete fabrication process for creating a tapered and dimpled optical fiber. The fiber is first stripped of its acrylic coating, cleaned, then clamped to motorized stages, as shown in figure 6.4(a). A hydrogen torch then heats the fiber as the stages move apart, pulling the fiber into a taper, as shown in figure 6.4(b). After the fiber is tapered, the torch is removed from under the fiber and the stages are stopped.

To dimple a fiber, begin with a tapered fiber. Figure 6.4(c) shows the first step of the dimpling process, where the fiber is formed into a dimple shape by moving the pulling stages together while guiding the taper downward using a bare optical fiber. Once the taper has been guided into a U shape, the dimple is annealed with the torch, with the guide fiber acting as a mold, as depicted in figure 6.4(d). Then the dimple shape is released by moving the pulling stages apart while raising the guide, as shown in figure 6.4(e). Finally, the guide fiber is carefully released from the dimple, and due to the annealing, the dimple shape remains, as shown in figure 6.4(f). If desired, the dimpled fiber can then be moved to another location, using a 3D printed fiber holder to support the fiber.

6.3.1 Tapering

Tapered fibers are desirable because they allow light to be coupled from the fiber into another optical device. In a standard fiber, the light is completely contained inside the glass of the fiber. By tapering the fiber, the evanescent field of the fiber extends into the air, and thus, by bringing the tapered fiber in close proximity to another optical device, evanescent coupling can occur. In this section, we describe the method for creating a tapered fiber.

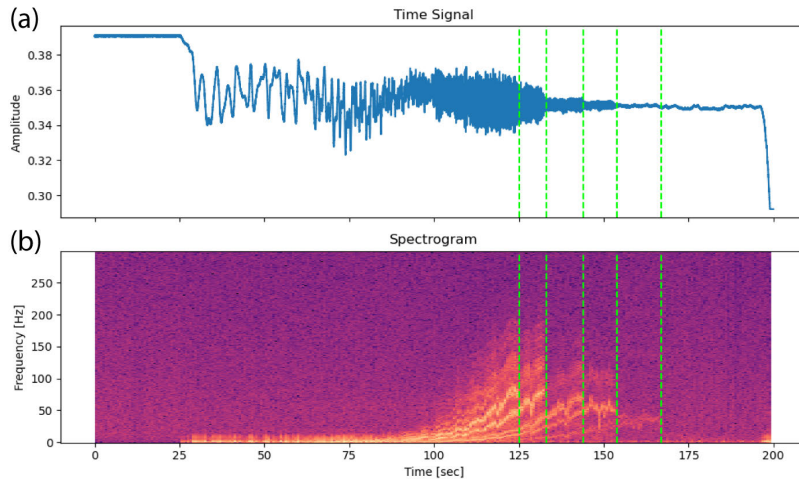


Figure 6.5: Optical transmission through a fiber as it is tapered, with green lines showing the cutoff of higher order fiber modes. (a) The optical power transmitted through the fiber. The cutoff of a higher order mode is visible as a decrease in the oscillation intensity. (b) The spectrogram of the power transmitted through the fiber. The beat patterns between modes can be seen as yellow curves increasing in frequency, which cut off.

Single Mode Tapers

When pulling a fiber, the final fiber diameter is most easily determined by seeking to create a single mode taper. The determination of how long to pull a fiber to ensure that it is single can be made by observing the optical throughput of the fiber, as shown in figure 6.5. As the fiber tapers, the core of the fiber becomes too small to support the optical mode, and the light begins to travel in the cladding of the fiber, which continues to guide the light as a glass/air waveguide. When this occurs, the fiber diameter is sufficiently large to support multiple optical modes, and these modes interfere with each other, as can be seen in figure 6.5(a), beginning at 29 s. The interference of these modes in combination with the changing length of the fiber as it continues to be tapered results in a beating pattern in the throughput of the fiber, which is seen as oscillations in the output power. As the fiber is tapered to smaller diameters, the higher order modes will no longer be supported, and those modes will no longer produce beating in the fiber throughput. For example, in figure 6.5(a) at 133 s, some higher order modes have been eliminated, and the beating amplitude is diminished. To determine when to stop the pull, the optical throughput of the taper is monitored, and the pull is stopped when the fiber becomes single mode, which is seen when the power output no longer exhibits oscillations [27, 42], as seen in figure 6.5(a) at 154 s. If the fiber is tapered further, it can break, as seen at 197 s in figure 6.5(a). The tapering process results in fibers whose optical mode has an evanescent tail in the air and therefore can be coupled to another optical device.

To further understand the effects of mode beating during fiber pulling and refine the pulling process, we can consider the spectrogram of the optical power through the fiber during the pulling process, shown in

figure 6.5(b). By doing so, we can perform frequency-domain real-time monitoring of the taper [99]. In this plot, the individual beating frequencies can be clearly seen as higher intensity lines. These lines stop when the higher order mode is no longer supported by the tapered fiber. A comparison of the spectrogram and the power makes the changes in the oscillations of the power signal (figure 6.5(a)) more meaningful and obvious. Additionally, some changes in the supported modes are not obvious in the power signal. For instance, at 157 s, no oscillations are visible in the power plot, but the spectrogram shows that a higher order mode is still present until 167 s. Tapering until this mode is eliminated will result in more consistent performance. Furthermore, tapers with very low loss exhibit much smaller oscillations, which can be difficult to observe in the power signal but remain obvious in the spectrogram. By using the spectrogram to determine the length of the fiber pulls, we are able to use an objective measure to determine when the pulling is complete, and the method is resilient to variations between fiber pulls.

Fiber Tapering Process

The fabrication process for a tapered fiber is relatively simple. We employ a heat-and-pull method, similar to previous work [27, 40–42]. We use 1-meter-long SMF-28 Ultra fiber patchcords. A small part of the fiber (about 1 inch long) is stripped of its acrylic coating. The stripped portion is then cleaned using isopropyl alcohol applied to a lint-free wipe and the fiber is clamped to the pulling stages. The hydrogen is set to flow and the torch is lit. The user then clicks the auto button in the fiber pull box, beginning the automated pull procedure.

The automated pull procedure has 4 steps. First, the background power level is determined. This is done by turning on the laser and collecting 5 seconds of optical power data. A fast Fourier transform (FFT) is performed on the data as it is collected, providing a spectrogram. The background noise level is determined from the frequency content, which will be used to determine when to end the pull. Second, the torch is moved horizontally so that it is under the fiber. The torch is positioned a few millimeters below the fiber, with the edge of the flame touching the fiber to create a large hotspot. The hotspot size determines the tapering rate of the fiber, with a large hotspot producing a gradual taper and a small hotspot producing a rapid taper. In order to ensure we can see the majority of the taper in later steps, we target a total taper length near 25 mm. This is sufficiently long to produce low-loss tapers. Third, with the torch under the fiber, the fiber is heated for 5 seconds before beginning the pull. The pulling stages then move apart at a constant speed, with the power through the fiber being monitored. The algorithm waits until the maximum value of the FFT is above the beat threshold (9 dB above the background) to ensure the beating between modes has begun. The algorithm then waits until the maximum value drops below the cutoff threshold (3 dB above the background). Fourth, once the beating has stopped, the torch is removed from under the fiber and the pulling motors are stopped. In some cases, the beating between modes has a

high intensity, and the cutoff threshold is raised to account for increased noise in the system.

6.3.2 Dimpling

While tapered fibers allow for optical coupling from the fiber to other optical devices, dimpled fibers are more useful for integrated devices. Devices located on a chip are difficult to couple to using a tapered fiber as the thick ends of the fiber can prevent the fiber from coming close enough to the optical device. Additionally, light can couple from the fiber anywhere the fiber is sufficiently thin. This makes it difficult to isolate coupling to a single on-chip device, especially when multiple on-chip devices are close together. Adding a dimple to the fiber solves both of these issues. The dimple shape makes it easier to place the narrow region of the taper close to the chip without the fiber touching in any other locations.

We now describe our automated dimpling process. This process combines computer vision (CV) algorithms with coordinated motor movements to ensure the process is robust to variations in the tapered fibers. Tapers of different lengths can all be dimpled with the same algorithm. To perform the dimpling using the GUI, the user clicks the auto button in the fiber dimple box after a fiber has been successfully tapered.

Guide Fiber Positioning

The first step of the dimpling process is to ensure the correct location of the guide fiber. The fiber is moved into approximate position over the taper, then the vertical guide motor is lowered until the guide fiber is visible in the camera frame. The guide fiber is vertically centered in the frame, then the guide fiber's horizontal position is adjusted until it is in focus with the camera. The vertical motor position and the lateral position of the guide fiber within the camera frame are noted for later use. This step is to determine the exact position of the guide fiber, which may not always be the same since the guide fiber is removed from the setup to remove the dimpled fiber using the fiber holder. When the guide fiber is replaced, exact repositioning is not necessary as this step accounts for small differences in the guide fiber position.

Taper Profile Mapping

The next step of the dimpling process is to map the profile of the tapered fiber. This mapping will be used to find the center of the taper and to determine the length of the flexible region of the taper. A typical tapered fiber profile is shown in figure 6.6(a). The central region has a constant thickness and its length is determined by the hotzone length a . The tapered region length is L , and it is based on the pull parameters (speed and hotzone length). The initial fiber thickness is r_0 , which in our case is equal to 125 μm . The equation describing the taper profile is [27, 99, 100]

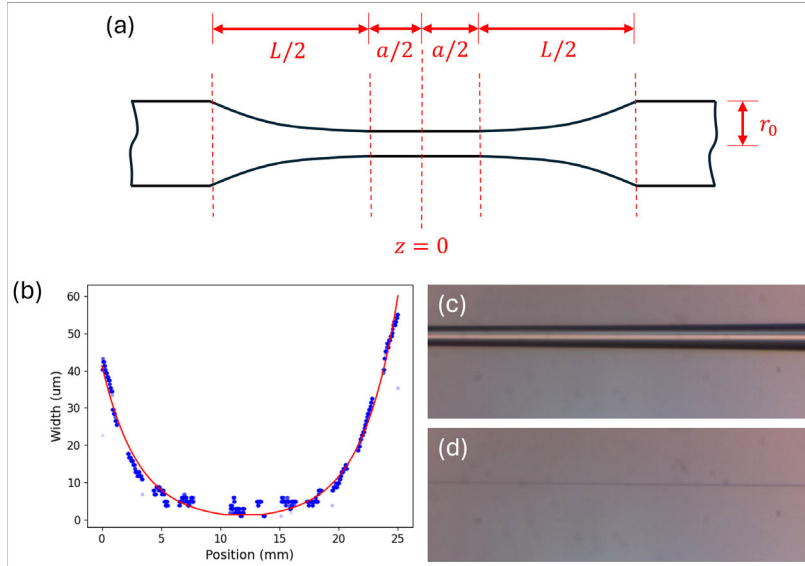


Figure 6.6: Taper profile mapping using computer vision. (a) Regions of a tapered fiber used in the fiber profile calculation. (b) The measured width of the taper along its length (blue) and the fit to the expected taper profile (red). The taper becomes hard to measure at its thinnest points. (c) Image of the taper near its end, where it is thick. (d) Image of the taper near its center, where it is thin.

$$\begin{cases} r(z) = r_0 \exp(-L/2a) & |z| \leq a/2 \\ r(z) = r_0 \exp\left(\frac{|z| - (a+L)/2}{a}\right) & a/2 \leq |z| \leq (L+a)/2 \\ r(z) = r_0 & |z| \geq (L+a)/2 \end{cases} \quad (6.1)$$

where z is the position along the length of the fiber, and r is the fiber radius.

We map the profile of the fiber by measuring its thickness using CV, then fitting our measurements to the expected equation. To measure the thickness, the pull motors are moved laterally to the extent of their travel, and CV is used to measure the width of the fiber at all points within the frame. The motors then scan across their travel, repeating the measurement at several locations. Figure 6.6(b) shows a plot of the fiber thickness with the measured fiber width in microns shown as blue dots. After the thickness is measured, the data is fit according to equation 6.1, with a , L , and the location of $z = 0$ left as fitting parameters. The fit is shown in red in figure 6.6(b).

There are some difficulties in determining the taper width. First, the camera view of thick regions of the taper contains a light stripe in the center of the fiber (see figure 6.6(c)). This occasionally causes the fiber thickness in parts of these regions to be measured as thinner than they are. Additionally, it is more difficult to measure the thickness of the taper near the center, where it is thin. Near the edges of the taper (as in figure 6.6(c)), the fiber is stiffer and easier to distinguish in the camera frame. However, the center (shown in figure 6.6(d)) is more likely to be

bent or move while the frame is being captured, and its edges are harder to distinguish. As such, it is common for this region to be measured as thicker than it is, and we expect there to be more noise and deviation from the fitted curve. These difficulties could possibly be mitigated using more rigorous CV techniques, but we have found that the profile mapping data we collect is sufficient to ensure the creation of a high quality dimple.

Dimpling

After determining the fiber profile, the system proceeds to the dimpling step, where the taper will be formed into a U shape. This is done by touching the center point (as determined by the taper profile mapping) of the taper with the guide fiber, then using the guide fiber to pull the taper center downward while the pull motors move laterally inward. During this step, it is desirable that the fiber remain taut but not overtensioned. If the taper is overtensioned, it may break or be pulled off the guide. If the fiber is too loose, the taper may detach from the guide or form loops on itself.

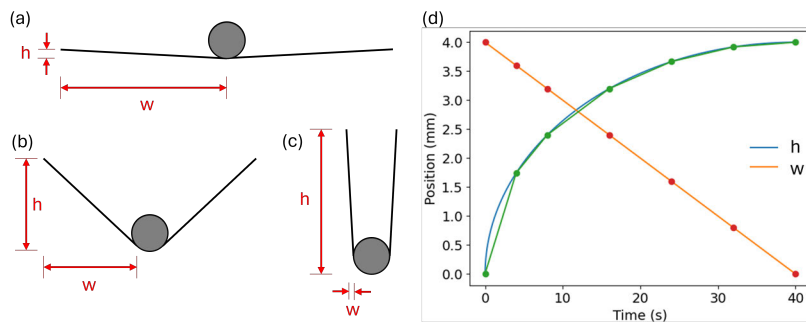


Figure 6.7: Motor movements during dimpling. (a–c) Shape of the taper before, during, and at the end of the dimpling step, respectively. (d) Graph of the width and height of the taper during the dimpling step.

We ensure that the tapered fiber remains taut by moving the guide fiber downward and the pull motors inward at specific rates based on the length of the taper. The relation between the different motor movements is shown in figure 6.7 and is given by the differential equation

$$\frac{dh}{dt} = -\frac{dw}{dt} \frac{w}{h} \quad (6.2)$$

where w is the width of the right triangle formed using the taper as the hypotenuse (see figure 6.7(a–c)) and h is its height. At the beginning of the tapering process (shown in figure 6.7(a)), w is half the length of the “flexible region” of the taper, that is, w is the length of the flexible region on a single side of the guide fiber, and h is nearly 0. During the dimpling process (shown in figure 6.7(b)), the guide pulls the taper down and the pull motors move together, causing h to increase while w decreases. At the end of the dimpling process (shown in figure 6.7(c)), h is half the length of the flexible section, and w is nearly 0.

We choose the motor movements by solving equation 6.2, using an initial value for w , a constant rate for dw/dt , and a chosen total movement time (typically 40 s). The initial value for w is determined using the previously performed taper profile, where w is chosen as half the length of the fiber below a specified thickness (typically about 3 μm). Equation 6.2 is solved numerically using a very fine step size, then 6 points along the curve are chosen as the movement steps. Figure 6.7(d) shows the results of this process for a typical taper with initial values of $w = 4$ mm, $dw/dt = -0.1$ mm/s, and a total time of 40 s. In the figure, the orange line represents w , with the selected movement steps as red dots. The blue line shows the calculated values for h , with the green dots and line showing the selected movement steps. At each step, the motors are commanded to move by the amount needed, and the speeds are set such that all motors finish their movement at the same time.

The mathematical description described above provides a good baseline for the system but makes two significant assumptions. The first is an assumption about taper flexibility. We assume the fiber to essentially be fixed at its ends, with no bending or movement outside the flexible region and perfect flexibility within it. Second, we neglect the effects of the taper wrapping around the guide as the dimpling process progresses. As a result of these assumptions, the movements calculated in the described manner are not perfect. The more significant effect is that of the fiber flexibility. In actuality, the flexibility of the taper will vary continuously since its thickness varies continuously. The result is that the fiber does not bend exactly as expected and the guide needs to move further than calculated near the end of the dimpling to keep the fiber taut. To account for this, we move the guide 1 mm further than calculated during the final step. We have found this to be an adequate adjustment, and the process ensures a taut fiber during the dimpling step.

We also note that the process is robust to different flexible region lengths. For example, if a higher thickness value is used to determine the initial value of w , causing it to be larger, the process will still function well. In this way, the total movement can be adjusted if necessary.

Adjustment, Anneal, and Release

After the dimpling steps are done, the dimple is adjusted to ensure the proper shape. The ideal shape for the dimple is a U shape with the fiber center wrapped tightly around the guide fiber and the fiber ends vertical. The camera is moved upward so that the tapered region of the fiber is visible, but the guide fiber is not. A CV algorithm is then used to determine the angles of the two sides of the tapered fiber. Typically, at this point the fiber is dimpled and appears like the image in figure 6.7(c). The fiber guide and the pull motors are then adjusted until the two sides of the fiber are both vertical. If the two sides of the fiber have different angles, the pull motors are moved to correct the difference. If the sides of the fiber are not vertical, the guide fiber is moved vertically until they are.

This final adjustment phase makes the dimpling process very robust, as any variations in the previous steps are corrected. In typical operation, these final adjustments are very minor.

After the final adjustments are made, the dimple is annealed. To anneal the fiber, the torch is first moved down to create a large gap between the torch and the fiber. In this way, the same flame size used for tapering (which occurs at a relatively high temperature) can be used for annealing, which is done at a lower temperature. The torch is then moved horizontally under the fiber and is removed after a very short dwell time (less than a second).

After annealing, the dimple is released. Similar to how the dimple is formed in 6 movement steps to keep the fiber taut, the release is performed in three movement steps, with the guide fiber being moved up at the same time as the pulling stages are moved apart. In this process, unlike that of forming the dimple, it is not necessary that the fiber remain taut, only that it not be overtensioned. It is also desirable that the fiber not become so loose that it wraps upon itself or the guide. The three-step process we use results in a fiber that is slack during the release but does not wrap on itself. After this process, the guide fiber will be in the same place as before the dimpling, in line with the tapered fiber. The pull motors are not moved all the way to their original positions, leaving the dimpled fiber slightly slack.

After the dimple is released, the guide fiber needs to be detached from the dimple. In most cases, this is easily performed by moving the guide fiber upward and adding tension to the dimple by moving the pulling stages apart until the dimple detaches. In some cases, nitrogen can be used to blow the dimple free. Because this step may require the use of nitrogen and is difficult to quantify, the automated dimpling process leaves this final step to be performed by the user. The GUI provides keyboard commands and buttons to facilitate the motor movement.

After the dimple is detached from the guide fiber, the dimpling process is complete and the guide fiber is moved back away from the dimpled fiber. The dimple can then be used in place or moved to another location.

6.3.3 Fiber Holder

After the tapering or dimpling process is complete, it is desirable to relocate the fiber to the testing location. To facilitate moving the tapered or dimpled fiber, we have developed a 3D printed fiber holder, which is shown in figure 6.8. A model of the fiber holder is shown on the left, and a fiber holder in use is shown on the right. The fiber holder has several important features. The base of the arms of the holder are designed to be flexible. We place a spring between the arms and a small bolt through them, with a nut in a recessed hole. In this way, by turning the screw, the distance between the arms can be adjusted, which allows the user to set the proper spacing for attaching the fiber and tension the fiber after it is epoxied in place. The side and bottom of the base of the fiber

holder have small ridges, which allow it to be placed into the groove of a positioning stage. After the fiber is attached, the fiber holder can be moved and either the bottom or side ridge can be used to ensure proper alignment to a positioning stage. The arms of the fiber holder extend beyond the holder to allow room for the sample to be placed under the holder. The arms have small notches near the front, where the fiber will be placed.

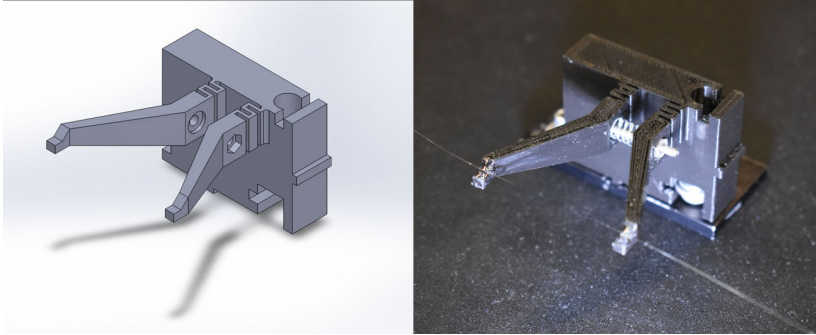


Figure 6.8: Custom fiber holder for removing fibers and positioning them for coupling. At left is a model of the component, and at right is shown the 3D printed component with a dimpled fiber attached.

To attach the fiber, the fiber holder is placed in the dimpling system. The ridge on the side of the fiber holder is used to mount the holder in the place of the guide fiber, enabling motorized control of the fiber holder and convenient positioning. The screw is then adjusted to the width of the fiber, and small beads of epoxy are placed on the ends of the arms. The fiber holder is then lowered below the dimpled fiber and moved upward until the epoxy contacts the fiber at its edges where it has not been tapered. The GUI has a button for removing the fiber, which moves the fiber holder below the taper and activates keyboard control to position the fiber holder. The epoxy is then cured with ultraviolet light. Once the epoxy is cured, the fiber clamps can be released, and the fiber holder can be removed.

6.4 Results

Table 6.1 shows the throughput power of four dimpled fibers. The table columns detail the power before the fiber is altered, after the fiber is tapered, and after the fiber is dimpled, with the power being given as the voltage (V) produced from a photodetector (Thorlabs DET10C2). Additionally, the final column lists the efficiency of the fiber, given as $V_{final}/V_{initial}$. The limiting factor in dimpled fiber efficiency tends to be the pull efficiency. Very little additional loss is incurred during the dimpling process.

Our system currently has a yield of around 50%. That is, half of the fibers break during the tapering and dimpling process. The fiber may break during the pull process if the pulling parameters are not well tuned

Table 6.1: Efficiency results of four dimpled fibers. The values of the first three columns are given as voltage readings from a photodiode and are proportional to the optical power through the fiber.

Initial (V)	After Pull (V)	After Dimpling (V)	Efficiency (%)
2.683	2.638	2.636	98.2
2.679	2.65	2.65	98.9
2.683	2.67	2.668	99.4
2.683	2.655	2.4	89.5

or if the pulling stages are misaligned. The taper may also stick to the guide fiber after the annealing. This effect is mitigated by using a quick anneal at a low temperature, but if the taper sticks to the guide fiber, the taper may break when the two are separated. The bulk of failures in our experiments have happened during the taper pull. Due to an unknown variable, the fiber tapering sometimes fails, with the fiber breaking near the end of the tapering process. This tends to happen in groups, with many fibers breaking in a row. However, at a later time, the fibers will be tapered and dimpled as expected, with a high yield (over 80%), despite there being no changes to the system or process from before. We expect that by determining and correcting this unknown variable, the yield will rise to over 80%.

6.5 Conclusion

In conclusion, we present a system capable of automated fabrication of tapered and dimpled optical fibers. Our system uses optical feedback and computer vision to enable a robust fabrication process. The system is able to create tapered and dimpled fibers with efficiencies of over 90% in under 10 minutes with no feedback needed from the user. We also include details of a 3D printed fiber holder, enabling the removal of tapered and dimpled fibers from the fabrication setup for use in other locations. We anticipate that the work presented here, if implemented, will greatly reduce technician training time and dimpled fiber fabrication time. We also anticipate an increased consistency of dimpled fibers created using this system over manual techniques. We hope this will accelerate the development of unique optical structures by providing a viable coupling scheme.

Conclusion

In conclusion, we have presented unique 3D printed mounts for liquid microdroplet resonators. These mounts provide a robust and easy-to-use method for supporting microdroplet resonators while still allowing control over the droplet position, shape, and size. In our earlier experiments, we found that the main deterrent to precisely controlling droplet size was the difficulty of placing the liquid on the mount by hand. The creation of 3D printed mounts with a central channel allowed for a more robust control over droplet size and allowed us to create stable water microdroplet resonators in ambient environments. The system we present overcomes the effect of droplet evaporation by supplying a constant flow into the droplet in stable equilibrium, and the resulting resonators exhibit very high optical quality factors. The exploration of freezing water droplets to create ice resonators resulted in methods for the creation of optically clear ice microdroplets in both high- and low-humidity environments. This method could lead to the creation of ice microdroplet resonators with a high quality factor. The need for humidity control in creating these ice droplets led to the creation of an environmental control box to control the humidity of the environment and the temperature of the samples. The box encompasses the entire optical setup, including the fiber tapering mechanism. Tapered optical fibers were essential for optical coupling and greatly facilitated our experiments, especially when the fibers were treated to be hydrophobic. Through time, the fiber tapering setup has been optimized, and our process has been refined. We have presented our system for the automated fabrication of both tapered and dimpled optical fibers. This system is capable of producing high-efficiency fibers with no user input through optical feedback and computer vision. The automated fabrication of tapered and dimpled fibers will accelerate future research, including research involving on-chip optical structures.

Future work by other researchers can include further exploration of non-spherical microdroplet resonators supported and shaped by 3D printed mounts. Other work may involve integrating additional microfluidic technologies, such as mixers and valves [32]. Integrating such microfluidic devices to the microresonator mount could allow for real-time manipulation of the droplet's contents, mixing and adding analytes or dyes on demand. The system we present here provides a basis for such future work and demonstrates a unique solution for the challenges inherent in using liquid microdroplet resonators. In

addition, freezing water droplets for use as resonators remains a viable research opportunity, utilizing our freezing methods and environmental control box. Finally, the automated system for fabricating tapered and dimpled optical fibers will greatly reduce the difficulty and time burden of researchers desiring to use tapered and dimpled fibers.

7.1 List of Publications

- Awerkamp, P. A. *et al.*, “Self-sustaining water microdroplet resonators using 3d-printed microfluidics,” *Micromachines*, vol. 15, no. 4, 2024, p. 423 . cited on pp. 21, 91
- Awerkamp, P. A. *et al.*, “3d printed mounts for microdroplet resonators,” *Optics Express*, vol. 30, no. 2, 2022, pp. 1599–1606 . cited on pp. 12, 29, 91
- Awerkamp, P. A. *et al.*, “Self-sustaining water microdroplet resonators using 3d printed microfluidics,” *Frontiers in Optics*, Optica Publishing Group, 2023, FTh1C-2 . cited on p. 91
- Awerkamp, P. *et al.*, “3d printed mounts for microdroplet resonators,” *Frontiers in Optics + Laser Science 2021*, Optica Publishing Group, 2021, JTu1A.35. DOI: 10.1364/fio.2021.jtu1a.35 . cited on p. 91
- Camacho, R. M. *et al.*, “Self-sustaining 3d thin liquid films in ambient environments,” *Advanced materials interfaces*, vol. 7, no. 9, 2020, p. 1901887 . cited on pp. 6, 13, 15, 26, 91
- Wright, K. S. *et al.*, “Freezing optically clear microdroplets in a laboratory setting,” *2023 Intermountain Engineering, Technology and Computing (IETC)*, IEEE, 2023, pp. 98–101 . cited on p. 91
- Henrie, A. *et al.*, “Hardware and software improvements to a low-cost horizontal parallax holographic video monitor,” *Applied optics*, vol. 57, no. 1, 2018, A122–A133 . cited on p. 91

References

- [1] Ashkin, A. and Dziedzic, J. M., "Observation of resonances in the radiation pressure on dielectric spheres," *Phys. Rev. Lett.*, vol. 38, 23 June 1977, pp. 1351–1354. DOI: 10.1103/physrevlett.38.1351 cited on pp. 1, 21
- [2] Wang, Y., Li, H., Zhao, L., Wu, B., Liu, S., Liu, Y., and Yang, J., "A review of droplet resonators: Operation method and application," *Optics & Laser Technology*, vol. 86, 2016, pp. 61–68. DOI: <https://doi.org/10.1016/j.optlastec.2016.07.002> cited on pp. 1, 21
- [3] Qian, S.-X., Snow, J. B., Tzeng, H.-M., and Chang, R. K., "Lasing droplets: Highlighting the liquid-air interface by laser emission," *Science*, vol. 231, no. 4737, 1986, pp. 486–488. cited on pp. 1, 12
- [4] Tang, S. K., Derda, R., Quan, Q., Lončar, M., and Whitesides, G. M., "Continuously tunable microdroplet-laser in a microfluidic channel," *Optics express*, vol. 19, no. 3, 2011, pp. 2204–2215. cited on pp. 1, 2, 12
- [5] Zhang, H., Palit, P., Liu, Y., Vaziri, S., and Sun, Y., "Reconfigurable integrated optofluidic droplet laser arrays," *ACS Applied Materials & Interfaces*, vol. 12, no. 24, 2020, pp. 26 936–26 942. cited on pp. 1, 2, 12, 22
- [6] Kiraz, A., Kurt, A., Dündar, M. A., and Demirel, A. L., "Simple largely tunable optical microcavity," *Applied Physics Letters*, 2006. DOI: 10.1063/1.2335371 cited on pp. 1, 2, 21, 22
- [7] Kiraz, A., Sennaroglu, A., Doğanay, S., Dündar, M. A., Kurt, A., Kalaycioglu, H., and Demirel, A. L., "Lasing from single, stationary, dye-doped glycerol/water microdroplets located on a superhydrophobic surface," *Optics Communications*, 2007. DOI: 10.1016/j.optcom.2007.04.026 cited on pp. 1, 2, 21, 22
- [8] Kiraz, A., Yorulmaz, S. C., Yorulmaz, M., and Sennaroglu, A., "Raman lasing near 650 nm from pure water microdroplets on a superhydrophobic surface," *Photonics and Nanostructures: Fundamentals and Applications*, 2009. DOI: 10.1016/j.photonics.2009.03.002 cited on pp. 1, 2, 21, 22
- [9] Maayani, S. and Carmon, T., "Droplet raman laser coupled to a standard fiber," *Photonics Research*, vol. 7, no. 10, 2019, pp. 1188–1192. cited on pp. 1, 12
- [10] Toropov, N., Cabello, G., Serrano, M. P., Gutha, R. R., Rafti, M., and Vollmer, F., "Review of biosensing with whispering-gallery mode lasers," *Light: Science & Applications*, vol. 10, no. 1, 2021, pp. 1–19. cited on pp. 1, 12, 21

- [11] Jonáš, A., Aas, M., Karadag, Y., Manioğlu, S., Anand, S., McGloin, D., Bayraktar, H., and Kiraz, A., "In vitro and in vivo biolasing of fluorescent proteins suspended in liquid microdroplet cavities," *Lab on a Chip*, vol. 14, no. 16, 2014, pp. 3093–3100. cited on pp. 1, 2, 12, 21, 22
- [12] Zhang, P., Jung, S., Lee, A., and Xu, Y., "Radiation-pressure-induced nonlinearity in microdroplets," *Physical Review E*, vol. 92, no. 6, 2015, p. 063 033. cited on pp. 1, 2, 12
- [13] Lee, A., Zhang, P., Xu, Y., and Jung, S., "Radiation pressure-induced nonlinearity in a micro-droplet," *Optics express*, vol. 28, no. 9, 2020, pp. 12 675–12 687. cited on pp. 1, 12
- [14] Dahan, R., Martin, L. L., and Carmon, T., "Droplet optomechanics," *Optica*, vol. 3, no. 2, 2016, pp. 175–178. cited on pp. 1, 2, 12
- [15] Chen, X., Fu, L., Lu, Q., Yang, H., Wu, X., and Xie, S., "High sensitivity temperature sensor based on packaged microdroplet whispering gallery mode resonator," *Tenth International Conference on Information Optics and Photonics*, vol. 10964, International Society for Optics and Photonics, 2018, p. 1 096 451. cited on pp. 1, 12
- [16] Avino, S., Krause, A., Zullo, R., Giorgini, A., Malara, P., De Natale, P., Looock, H. P., and Gagliardi, G., "Direct sensing in liquids using whispering-gallery-mode droplet resonators," *Advanced Optical Materials*, vol. 2, no. 12, 2014, pp. 1155–1159. cited on pp. 1, 12
- [17] Labrador-Páez, L., Soler-Carracedo, K., Hernández-Rodríguez, M., Martín, I. R., Carmon, T., and Martin, L. L., "Liquid whispering-gallery-mode resonator as a humidity sensor," *Optics express*, vol. 25, no. 2, 2017, pp. 1165–1172. cited on pp. 1, 12
- [18] Kiraz, A., Karadag, Y., and Coskun, A. F., "Spectral tuning of liquid microdroplets standing on a superhydrophobic surface using electrowetting," *Applied Physics Letters*, 2008. DOI: 10.1063/1.2927373 cited on pp. 1, 2, 21, 22
- [19] Kiraz, A., Karadag, Y., Yorulmaz, S. C., and Muradoglu, M., "Reversible photothermal tuning of a salty water microdroplet," *Physical Chemistry Chemical Physics*, 2009. DOI: 10.1039/b816784b cited on pp. 1, 2, 21, 22
- [20] Maayani, S., Martin, L. L., and Carmon, T., "Water-walled microfluidics for high-optical finesse cavities," *Nature communications*, vol. 7, no. 1, 2016, pp. 1–4. cited on pp. 1, 2, 12, 13, 21, 22, 30
- [21] Yilgor, I., Jonáš, A., Karadag, Y., Mestre, M., Mestre, M., and Kiraz, A., "Probing of ultrahigh optical q-factors of individual liquid microdroplets on superhydrophobic surfaces using tapered optical fiber waveguides," *Journal of The Optical Society of America B-optical Physics*, 2012. DOI: 10.1364/josab.29.003240 cited on pp. 1, 2, 21, 22
- [22] Kaminski, S., Martin, L. L., and Carmon, T., "Tweezers controlled resonator," *Optics express*, vol. 23, no. 22, 2015, pp. 28 914–28 919. cited on pp. 2, 12

- [23] Anand, S., Eryürek, M., Karadag, Y., Erten, A., Serpengüzel, A., Jonáš, A., and Kiraz, A., "Observation of whispering gallery modes in elastic light scattering from microdroplets optically trapped in a microfluidic channel," *JOSA B*, vol. 33, no. 7, 2016, pp. 1349–1354. cited on pp. 2, 12
- [24] Guillon, M., Miles, R. E., Reid, J. P., and McGloin, D., "Thermo-optical resonance locking of an optically trapped salt-water microdroplet," *New Journal of Physics*, vol. 11, no. 10, 2009, p. 103 041. cited on pp. 2, 22
- [25] Jonáš, A., Karadag, Y., Mestre, M., and Kiraz, A., "Probing of ultrahigh optical q-factors of individual liquid microdroplets on superhydrophobic surfaces using tapered optical fiber waveguides," *JOSA B*, vol. 29, no. 12, 2012, pp. 3240–3247. cited on pp. 2, 12
- [26] Yang, Y., Yang, Y., Liu, Y., Liu, Y., Liu, Y., Sun, S., Li, W., Li, W., Li, W., Li, W., Li, W., Zhu, N., Li, M., Li, M., Li, M., Li, M., and Li, M., "Optical phase matching of high-order azimuthal wgm in a water droplet resonator," *Optics Express*, 2019. DOI: 10.1364/oe.27.033436 cited on pp. 2, 22
- [27] Gaira, M. and Unnikrishnan, C., "Integrated table-top facility for the study of whispering gallery modes in dynamic liquid micro-cavities coupled to sub-micron tapered fibers," *ArXiv preprint arXiv:1911.01187*, 2019. cited on pp. 2–4, 12, 16, 28, 81–83
- [28] Maayani, S., Martin, L. L., Kaminski, S., and Carmon, T., "Cavity opto-capillaries," *Null*, 2015. DOI: null cited on pp. 2, 21, 22
- [29] Giorgini, A., Giorgini, A., Avino, S., Malara, P., Natale, P. D., Natale, P. D., Gagliardi, G., Gagliardi, G., Gagliardi, G., and Gagliardi, G., "Liquid droplet microresonators," *Sensors*, 2019. DOI: 10.3390/s19030473 cited on pp. 2, 22
- [30] Hossein-Zadeh, M., Vahala, K. J., and Vahala, K. J., "Fiber-taper coupling to whispering-gallery modes of fluidic resonators embedded in a liquid medium," *Optics Express*, 2006. DOI: 10.1364/oe.14.010800 cited on pp. 2, 22
- [31] Gong, H., Bickham, B. P., Woolley, A. T., and Nordin, G. P., "Custom 3d printer and resin for 18 μm \times 20 μm microfluidic flow channels," *Lab on a Chip*, vol. 17, no. 17, 2017, pp. 2899–2909. cited on pp. 2, 12, 13, 23
- [32] Sanchez Noriega, J. L., Chartrand, N. A., Valdoz, J. C., Cribbs, C. G., Jacobs, D. A., Poulson, D., Viglione, M. S., Woolley, A. T., Van Ry, P. M., Christensen, K. A., and Nordin, G. P., "Spatially and optically tailored 3d printing for highly miniaturized and integrated microfluidics," *Nature communications*, vol. 12, no. 1, 2021, pp. 1–13. cited on pp. 2, 12, 13, 23, 32, 90
- [33] Tavakoli, F., Davis, S. H., and Kavehpour, H. P., "Freezing of supercooled water drops on cold solid substrates: Initiation and mechanism," *Journal of Coatings Technology and Research*, vol. 12, 2015, pp. 869–875. cited on pp. 3, 33
- [34] Perez-Diaz, J. L., Alvarez-Valenzuela, M. A., Sanchez-Garcia-Casarrubios, J., and Jimenez-Lopez, S., "Ice surface entropy induction by humidity or how humidity prompts freezing," *ArXiv preprint arXiv:1509.06728*, 2015. cited on pp. 3, 33, 39
- [35] Warren, S. G., "Optical properties of ice and snow," *Philosophical Transactions of the Royal Society A*, vol. 377, no. 2146, 2019, p. 20 180 161. cited on pp. 3, 33

- [36] Shen, Y., "Nonlinear optical vibrational spectroscopy on surface-induced ice structures," *Technical Digest. Summaries of Papers Presented at the Quantum Electronics and Laser Science Conference*, IEEE, 1992, pp. 117–118. cited on pp. 3, 33
- [37] Johansson, P. K., Schmüser, L., and Castner, D. G., "Nonlinear optical methods for characterization of molecular structure and surface chemistry," *Topics in catalysis*, vol. 61, 2018, pp. 1101–1124. cited on pp. 3, 33
- [38] Lovering, K. A. and Chou, K. C., "Insights into ice formation via immersion freezing from nonlinear optical spectroscopy," *Topics in Catalysis*, vol. 61, 2018, pp. 1163–1168. cited on pp. 3, 33
- [39] Li, X., Cui, B., Xu, P., Xie, Y., Wang, P., Tong, L., and Guo, X., "Ice microsphere optical cavities," *Advanced Optical Materials*, vol. 12, no. 18, 2024, p. 2302609. cited on p. 3
- [40] Ward, J., Maimaiti, A., Le, V. H., and Chormaic, S. N., "Contributed review: Optical micro-and nanofiber pulling rig," *Review of Scientific Instruments*, vol. 85, no. 11, 2014, p. 111501. cited on pp. 3, 16, 28, 82
- [41] Knight, J. C., Cheung, G., Jacques, F., and Birks, T., "Phase-matched excitation of whispering-gallery-mode resonances by a fiber taper," *Optics letters*, vol. 22, no. 15, 1997, pp. 1129–1131. cited on pp. 3, 16, 28, 82
- [42] Hauer, B. D., Kim, P. H., Doolin, C., MacDonald, A. J., Ramp, H., and Davis, J. P., "On-chip cavity optomechanical coupling," *EPJ Techniques and Instrumentation*, vol. 1, no. 1, 2014, pp. 1–21. cited on pp. 3, 4, 16, 28, 76, 81, 82
- [43] Michael, C. P., Borselli, M., Johnson, T. J., Johnson, T. J., Chrystal, C., Chrystal, C., and Painter, O., "An optical fiber-taper probe for wafer-scale microphotonic device characterization," *Optics Express*, 2007. DOI: 10.1364/oe.15.004745 cited on p. 4
- [44] Kim, P., Fani Sani, F., Freeman, M., and Davis, J., "Broadband optomechanical transduction of nanomagnetic spin modes," *Applied Physics Letters*, vol. 113, no. 8, 2018. cited on pp. 4, 76
- [45] Doolin, C., Doolin, P., Lewis, B., and Davis, J., "Refractometric sensing of li salt with visible-light si₃n₄ microdisk resonators," *Applied Physics Letters*, vol. 106, no. 8, 2015. cited on pp. 4, 76
- [46] Saleem-Urothodi, R., Le Pouliquen, J., Rohel, T., Bernard, R., Pareige, C., Lorenzo-Ruiz, A., Beck, A., Létoublon, A., De Sagazan, O., Cornet, C., *et al.*, "Loss assessment in random crystal polarity gallium phosphide microdisks grown on silicon," *Optics Letters*, vol. 45, no. 16, 2020, pp. 4646–4649. cited on pp. 4, 76
- [47] Masuda, T., Hadden, J., Lake, D. P., Mitchell, M., Flågan, S., and Barclay, P. E., "Fiber-taper collected emission from nv centers in high-q/v diamond microdisks," *Optics Express*, vol. 32, no. 5, 2024, pp. 8172–8188. cited on pp. 4, 76
- [48] Eichenfield, M., Michael, C. P., Perahia, R., and Painter, O., "Actuation of micro-optomechanical systems via cavity-enhanced optical dipole forces," *Nature Photonics*, vol. 1, no. 7, 2007, pp. 416–422. cited on pp. 4, 76

- [49] Mitchell, M., Hryciw, A. C., and Barclay, P. E., "Cavity optomechanics in gallium phosphide microdisks," *Applied Physics Letters*, vol. 104, no. 14, 2014. cited on pp. 4, 76
- [50] Kim, P. H., Doolin, C., Hauer, B. D., MacDonald, A. J., Freeman, M. R., Barclay, P. E., and Davis, J. P., "Nanoscale torsional optomechanics," *Applied Physics Letters*, vol. 102, no. 5, 2013. cited on pp. 4, 76
- [51] Michael, C. P., Borselli, M., Johnson, T. J., Chrystal, C., and Painter, O., "An optical fiber-taper probe for wafer-scale microphotonic device characterization," *Optics express*, vol. 15, no. 8, 2007, pp. 4745–4752. cited on pp. 4, 76
- [52] Jayakumar, H., Khanaliloo, B., Lake, D. P., and Barclay, P. E., "Tunable amplification and cooling of a diamond resonator with a microscope," *Physical Review Applied*, vol. 16, no. 1, 2021, p. 014 063. cited on pp. 4, 76
- [53] Eichenfield, M., Chan, J., Camacho, R. M., Vahala, K. J., and Painter, O., "Optomechanical crystals," *Nature*, vol. 462, no. 7269, 2009, pp. 78–82. cited on pp. 4, 76
- [54] Burek, M. J., Cohen, J. D., Meenehan, S. M., El-Sawah, N., Chia, C., Ruelle, T., Meesala, S., Rochman, J., Atikian, H. A., Markham, M., *et al.*, "Diamond optomechanical crystals," *Optica*, vol. 3, no. 12, 2016, pp. 1404–1411. cited on pp. 4, 76
- [55] Camacho, R. M., Fish, D., Simmons, M., Awerkamp, P., Anderson, R., Carlson, S., Laney, J., Viglione, M., and Nordin, G. P., "Self-sustaining 3d thin liquid films in ambient environments," *Advanced materials interfaces*, vol. 7, no. 9, 2020, p. 1 901 887. cited on pp. 6, 13, 15, 26, 91
- [56] Saleh, B. E. and Teich, M. C., *Fundamentals of photonics*. John Wiley & sons, 2019. cited on pp. 8, 10
- [57] Gorodetsky, M. L., Savchenkov, A. A., and Ilchenko, V. S., "Ultimate q of optical microsphere resonators," *Opt. Lett.*, vol. 21, no. 7, April 1996, pp. 453–455. DOI: 10.1364/ol.21.000453 cited on pp. 9, 30
- [58] Garcia-Fernandez, R., Alt, W., Bruse, F., Dan, C., Karapetyan, K., Rehband, O., Stiebeiner, A., Wiedemann, U., Meschede, D., and Rauschenbeutel, A., "Optical nanofibers and spectroscopy," *Applied Physics B*, vol. 105, 2011, pp. 3–15. cited on p. 10
- [59] Awerkamp, P. A., Fish, D., King, M., Hill, D., Nordin, G. P., and Camacho, R. M., "3d printed mounts for microdroplet resonators," *Optics Express*, vol. 30, no. 2, 2022, pp. 1599–1606. cited on pp. 12, 29, 91
- [60] Wu, J., Guo, X., Zhang, A. P., and Tam, H.-Y., "Rapid 3d μ -printing of polymer optical whispering-gallery mode resonators," *Optics express*, vol. 23, no. 23, 2015, pp. 29 708–29 714. cited on p. 12
- [61] Saetchnikov, A. V., Tcherniavskaia, E. A., Saetchnikov, V. A., and Ostendorf, A., "A laser written 4d optical microcavity for advanced biochemical sensing in aqueous environment," *Journal of Lightwave Technology*, vol. 38, no. 8, 2020, pp. 2530–2538. cited on p. 12
- [62] Awerkamp, P. A., Hill, D., Fish, D., Wright, K., Bashaw, B., Nordin, G. P., and Camacho, R. M., "Self-sustaining water microdroplet resonators using 3d-printed microfluidics," *Micromachines*, vol. 15, no. 4, 2024, p. 423. cited on pp. 21, 91

- [63] Mavrogiannis, N., Ibo, M., Fu, X., Crivellari, F., and Gagnon, Z., "Microfluidics made easy: A robust low-cost constant pressure flow controller for engineers and cell biologists," *Biomicrofluidics*, vol. 10, no. 3, 2016, p. 034107. cited on pp. 24, 25
- [64] Erbil, H. Y., "Evaporation of pure liquid sessile and spherical suspended drops: A review," *Advances in colloid and interface science*, vol. 170, no. 1-2, 2012, pp. 67–86. cited on p. 29
- [65] Chini, S. F. and Amirfazli, A., "Understanding the evaporation of spherical drops in quiescent environment," *Colloids and Surfaces A: Physicochemical and Engineering Aspects*, vol. 432, 2013, pp. 82–88. cited on p. 29
- [66] Hale, G. M. and Querry, M. R., "Optical constants of water in the 200-nm to 200- μ m wavelength region," *Applied optics*, vol. 12, no. 3, 1973, pp. 555–563. cited on p. 30
- [67] Wright, K. S., Awerkamp, P. A., Hill, D., Bashaw, B., Van Woerkom, D., Fish, D., Nordin, G. P., and Camacho, R. M., "Freezing optically clear microdroplets in a laboratory setting," *2023 Intermountain Engineering, Technology and Computing (IETC)*, 2023, pp. 98–101. DOI: 10.1109/ietc57902.2023.10152156 cited on p. 33
- [68] Warren, S. G., "Optical constants of ice from the ultraviolet to the microwave," *Applied optics*, vol. 23, no. 8, 1984, pp. 1206–1225. cited on p. 33
- [69] Bari, S. and Hallett, J., "Nucleation and growth of bubbles at an ice–water interface," *Journal of Glaciology*, vol. 13, no. 69, 1974, pp. 489–520. cited on p. 34
- [70] Jambon-Puillet, E., Shahidzadeh, N., and Bonn, D., "Singular sublimation of ice and snow crystals," *Nature communications*, vol. 9, no. 1, 2018, p. 4191. cited on p. 37
- [71] Birdi, K., Vu, D., and Winter, A., "A study of the evaporation rates of small water drops placed on a solid surface," *The Journal of physical chemistry*, vol. 93, no. 9, 1989, pp. 3702–3703. cited on p. 37
- [72] Wilson, L., "The physics of microdroplets, by jean berthier and kenneth a. brakke. scope: Review. level: Postgraduates, advanced undergraduates, researchers, scientists, engineers," *Contemporary Physics*, vol. 53, no. 6, 2012, pp. 513–514. cited on p. 37
- [73] Chatterjee, R., Beysens, D., and Anand, S., "Delaying ice and frost formation using phase-switching liquids," *Advanced Materials*, vol. 31, no. 17, 2019, p. 1807812. cited on p. 43
- [74] Lv, J., Song, Y., Jiang, L., and Wang, J., "Bio-inspired strategies for anti-icing," *ACS nano*, vol. 8, no. 4, 2014, pp. 3152–3169. cited on p. 43
- [75] Albuquerque, F. B. and Shea, H., "Effect of humidity, temperature, and elastomer material on the lifetime of silicone-based dielectric elastomer actuators under a constant dc electric field (conference presentation)," *Electroactive Polymer Actuators and Devices (EAPAD) XXII*, vol. 11375, SPIE, 2020, 113751E. cited on p. 43

- [76] Lo, C., Chang, C., Chu, B., Pearton, S., Dabiran, A., Chow, P., and Ren, F., cited on p. 43
“Effect of humidity on hydrogen sensitivity of pt-gated algan/gan high electron mobility transistor based sensors,” *Applied Physics Letters*, vol. 96, no. 23, 2010, p. 232 106.
- [77] He, C., Korposh, S., Correia, R., Liu, L., Hayes-Gill, B. R., and Morgan, S. P., cited on p. 43
“Optical fibre sensor for simultaneous temperature and relative humidity measurement: Towards absolute humidity evaluation,” *Sensors and Actuators B: Chemical*, vol. 344, 2021, p. 130 154.
- [78] Häusler, T., Witek, L., Felgitsch, L., Hitzenberger, R., and Grothe, H., cited on p. 43
“Freezing on a chip—a new approach to determine heterogeneous ice nucleation of micrometer-sized water droplets,” *Atmosphere*, vol. 9, no. 4, 2018, p. 140.
- [79] Mishchenko, L., Khan, M., Aizenberg, J., and Hatton, B. D., cited on p. 43
“Spatial control of condensation and freezing on superhydrophobic surfaces with hydrophilic patches,” *Advanced functional materials*, vol. 23, no. 36, 2013, pp. 4577–4584.
- [80] Roy, P., Mael, L. E., Makhnenko, I., Martz, R., Grassian, V. H., and Dutcher, C. S., cited on p. 43
“Temperature-dependent phase transitions of aqueous aerosol droplet systems in microfluidic traps,” *ACS Earth and Space Chemistry*, vol. 4, no. 9, 2020, pp. 1527–1539.
- [81] Silva Bernardo, A. P. da, Silva, A. C. M. da, Francisco, V. C., Ribeiro, F. A., Nassu, R. T., Calkins, C. R., Nascimento, M. d. S. do, and Pflanzler, S. B., cited on p. 44
“Effects of freezing and thawing on microbiological and physical-chemical properties of dry-aged beef,” *Meat science*, vol. 161, 2020, p. 108 003.
- [82] Nakagawa, K., cited on p. 44
“Food drying at sub-zero temperature: Importance of glassy phase on product quality,” *Science, Engineering and Health Studies*, 2018, pp. 125–137.
- [83] Young, M. A., Furr, D. P., McKeough, R. Q., Elliott, G. D., and Trammell, S. R., cited on p. 44
“Light-assisted drying for anhydrous preservation of biological samples: Optical characterization of the trehalose preservation matrix,” *Biomedical Optics Express*, vol. 11, no. 2, 2020, pp. 801–816.
- [84] Downton, B. and Walker, S., cited on p. 44
“Humidity effects on calibrations of radiation therapy electrometers,” *Medical Physics*, vol. 39, no. 2, 2012, pp. 984–987.
- [85] He, Y., Ung, B. S.-Y., Parrott, E. P., Ahuja, A. T., and Pickwell-MacPherson, E., cited on p. 44
“Freeze-thaw hysteresis effects in terahertz imaging of biomedical tissues,” *Biomedical optics express*, vol. 7, no. 11, 2016, pp. 4711–4717.
- [86] Cameron, R. and Dixon, G., cited on p. 44
“Air temperature, humidity and rooting volume affecting freezing injury to rhododendron and other perennials,” *Journal of Horticultural Science*, vol. 72, no. 4, 1997, pp. 553–562.
- [87] Matsuo, T. and Sasyo, Y., cited on p. 44
“Melting of snowflakes below freezing level in the atmosphere,” *Journal of the Meteorological Society of Japan. Ser. II*, vol. 59, no. 1, 1981, pp. 10–25.

- [88] Niedringhaus, K. D., Brown, J. D., Ternent, M. A., Peltier, S. K., and Yabsley, M. J., "Effects of temperature on the survival of sarcoptes scabiei of black bear (*Ursus americanus*) origin," *Parasitology research*, vol. 118, no. 10, 2019, pp. 2767–2772. cited on p. 44
- [89] Gong, F., Jacobsen, S., Li, P., Wang, Z., Maekawa, K., and Koniorczyk, M., "Modeling of path-dependent phase change in sorption and freezing of pore water for cementitious materials," *Journal of Building Engineering*, 2022, p. 104969. cited on p. 44
- [90] Mohammad Khanlou, H., Hall, W., Woodfield, P., Summerscales, J., and Francucci, G., "The mechanical properties of flax fibre reinforced poly (lactic acid) bio-composites exposed to wet, freezing and humid environments," *Journal of Composite Materials*, vol. 52, no. 6, 2018, pp. 835–850. cited on p. 44
- [91] Kozikowski, B. A., Burt, T. M., Tirey, D. A., Williams, L. E., Kuzmak, B. R., Stanton, D. T., Morand, K. L., and Nelson, S. L., "The effect of freeze/thaw cycles on the stability of compounds in DMSO," *SLAS Discovery*, vol. 8, no. 2, 2003, pp. 210–215. cited on p. 44
- [92] Hillman, T. C., Idnani, R., and Wilson, C. G., "An inexpensive open-source chamber for controlled hypoxia/hyperoxia exposure," *Frontiers in Physiology*, 2022, p. 1301. cited on p. 44
- [93] Lau, S. K., Ribeiro, F. A., Subbiah, J., and Calkins, C. R., "Agenator: An open source computer-controlled dry aging system for beef," *HardwareX*, vol. 6, 2019, e00086. cited on p. 44
- [94] Lau, S. K. and Subbiah, J., "Humidosh: A self-contained environmental chamber with controls for relative humidity and fan speed," *HardwareX*, vol. 8, 2020, e00141. cited on p. 44
- [95] Herrmann, A. J. and Gehringer, M. M., "A low-cost automatized anaerobic chamber for long-term growth experiments and sample handling," *HardwareX*, vol. 10, 2021, e00237. cited on p. 44
- [96] Ploeg, Sequoia and Hill, David and Carver, Christian, *Pyrolab*, version 0.2.1, August 2022. URL: <https://github.com/BYUCamachoLab/pyrolab>. cited on pp. 44, 64, 78
- [97] *Low voltage temperature sensors*, TMP36, Rev. H, Analog Devices, May 2015. cited on p. 64
- [98] *I2c humidity and temperature sensor*, Si7021-A20, Rev. 1.2, Silicon Labs, August 2016. cited on pp. 64, 71
- [99] Ren, Y., Li, M., Ray, S., Bozeat, B. J., and Liu, Y., "Highly accessible low-loss fiber tapering by the ceramic housed electric furnace (chef) and frequency-domain real-time monitoring," *Review of Scientific Instruments*, vol. 92, no. 3, 2021. cited on pp. 82, 83
- [100] Birks, T. A. and Li, Y. W., "The shape of fiber tapers," *Journal of Lightwave Technology*, vol. 10, no. 4, 1992, pp. 432–438. cited on p. 83

- [101] Awerkamp, P. A., Hill, D., Fish, D., Wright, K., Bashaw, B., Nordin, G. P., and Camacho, R. M., "Self-sustaining water microdroplet resonators using 3d printed microfluidics," *Frontiers in Optics*, Optica Publishing Group, 2023, FTh1C-2. cited on p. 91
- [102] Awerkamp, P., Fish, D., King, M., Hill, D., Nordin, G. P., and Camacho, R. M., "3d printed mounts for microdroplet resonators," *Frontiers in Optics + Laser Science 2021*, Optica Publishing Group, 2021, JTU1A.35. DOI: 10.1364/fio.2021.jtu1a.35 cited on p. 91
- [103] Wright, K. S., Awerkamp, P. A., Hill, D., Bashaw, B., Van Woerkom, D., Fish, D., Nordin, G. P., and Camacho, R. M., "Freezing optically clear microdroplets in a laboratory setting," *2023 Intermountain Engineering, Technology and Computing (IETC)*, IEEE, 2023, pp. 98–101. cited on p. 91
- [104] Henrie, A., Codling, J. R., Gneiting, S., Christensen, J. B., Awerkamp, P., Burdette, M. J., and Smalley, D. E., "Hardware and software improvements to a low-cost horizontal parallax holographic video monitor," *Applied optics*, vol. 57, no. 1, 2018, A122–A133. cited on p. 91